PATHWAYS OF BACTERIAL INFILTRATION INTO PLANT LEAVES: MECHANISTIC MODELING, MICROBIOLOGICAL AND MICROFABRICATION EXPERIMENTS

A Dissertation

Presented to the Faculty of the Graduate School

of Cornell University

in Partial Fulfillment of the Requirements for the Degree of

Doctor of Philosophy

by

Mohsen Ranjbaran

August 2019

PATHWAYS OF BACTERIAL INFILTRATION INTO PLANT LEAVES: MECHANISTIC MODELING, MICROBIOLOGICAL AND MICROFABRICATION EXPERIMENTS

Mohsen Ranjbaran, Ph.D.

Cornell University 2019

During pre- and post-harvest processing, leafy greens are exposed to environmental conditions such as large variations in outside temperature and pressure, exposure to light, and evaporation of surface water. These conditions can serve as driving forces for stimulating various modes of bacterial transport into leafy greens. This work aims to show how the applications of physics-based modeling, microfluidics and microbiological experimentation can lead to a deep understanding of various pathways by which bacteria can penetrate into plant leaves. Three physics-based models are presented: 1) A porous media transport model for pressure-driven infiltration of water and bacteria into plant leaves during vacuum cooling, 2) A porous media transport model for light-induced chemotactic infiltration of bacteria into plant leaves, and 3) A model of transport in a two-phase fluid system, with phase interface tracking, for bacterial retention and infiltration at/into plant leaves during sessile droplet evaporation. Microbiological experiments to quantify the amount of bacterial infiltration into plant leaves during exposure to light are conducted to validate the second model. Using photolithography techniques, artificial surfaces patterned with common microstructures at the surface of plant leaves, *i.e.*, stomata, trichomes and grooves, are fabricated and used to support findings of the third model.

BIOGRAPHICAL SKETCH

Mohsen Ranjbaran was born in Fasa, a warm and small city in the Fars province of Iran. He grew up in the beautiful city of Shiraz, the capital of Iranian culture and poetry. After graduation from high school, he attended Shiraz University, one of the leading universities in Iran, and earned his Bachelor's degree in Agricultural Engineering. He finished the undergraduate degree as a first-rank student in 2004, and immediately started his Master's degree in the same field and university. During his Master's research, he worked on developing novel mechanistic models for microwave-assisted fluidized bed drying of moist granular materials. After graduation, he attended Ferdowsi University of Mashhad as a research assistant and worked on developing mechanistic models for aeration and drying process of stored grains. Before attending to Cornell, he had published eight scientific papers out of his past research in high ranked journals. In 2015, he moved to Ithaca, New York, to start his PhD program at Cornell University in the field of Biological and Environmental Engineering. After two years, he earned his second Master's degree, and continued on his PhD. In 2016 and 2017, he earned two Sagi/Spencer awards as partial financial supports to his research in the area of food safety engineering.

To Mina, my wife.

ACKNOWLEDGEMENTS

This work was not possible without all kind supports and guidance of Professor Ashim K. Datta. I sincerely feel that I have been fortunate to work with him, and I will be proud of that. I would like to thank Professors Carmen Moraru and Abraham Duncan Stroock for their roles on my special committee. I acknowledge Professor Ludmilla Aristilde for granting me access to her lab, in order to conduct microbiological experiments. Also, I thank Professor Mingming Wu for all her guidance to me during my microfabrication project at The Cornell NanoScale Science & Technology Facility (CNF). My project at CNF was not possible without the endless helps, guidance, and training of Dr. Beth Rhoades. Also, several other staff members at CNF kindly helped me that include Tom Pennell, John Treichler, Alan R. Bleier, Christopher Alpha, Edward Camacho, Phil Infante, Xinwei Wu. I appreciate Mina Soltalab, my wife and a PhD Candidate at Professor Aristilde lab, for training me on several microbiological experiments. I conducted many microscopy imaging experiments at the Imaging Facility of the Institute of Biotechnology of Cornell University, where I received several helps and training from Carol Bayles, and Johanna Dela Cruz. Also, I used microscopy imaging facility of the Plant Cell Imaging Center (PCIC) at the Boyce Thompson Institute of Cornell University with the help of Dr. Mamta Srivastava.

My attendance to Cornell University and earning a PhD degree was not possible without all generous helps and mental supports of my father, Abdolmajid Ranjbaran, and my mother, Roghayeh Ranjbaran.

TABLE OF CONTENTS

CHAPTER 1

INTRODUCTION

Leafy greens are among the most contaminated food products to human pathogenic bacteria (DeWaal and Bhuiya, 2007). From 2005 to 2011, there were 5415 outbreaks associated to vegetable sprouts and leafy greens, like spinach and lettuce; 73% of which occurred in 2011 due to *E. coli* O104:H4 and *E. coli* O157:H7 (Olaimat and Holley, 2012). Very recently, the Centers for Disease Control and Prevention of the US (CDC, 2018) reported 210 *E. coli* O157:H7 infections linked to romaine lettuce. Infiltration of human pathogens into fresh leafy greens significantly increases the risk of foodborne illnesses, as the internalized microbes cannot be effectively removed or treated utilizing standard sanitation and washing processes (Zhang et al., 2009; Vonasek and Nitin, 2016). Contamination of leafy greens by bacteria is a complex process that involves various influencing factors. Bacteria can get into initial contact with a leaf surface through various routes, such as contaminated irrigation or wash water, and infiltrate the leaf through available opening at the leaf surface, such as stomata, cuts, or wounds. During pre- and post-harvest processing, leafy greens are exposed to environmental conditions such as large variations in outside temperature and pressure, and exposure to light. These conditions can serve as driving forces for stimulating various modes of bacterial transport into leafy greens. Mechanistic understanding of the role these factors can help in better prevention of contamination of leafy greens by pathogenic microorganisms.

This work aims to show how the applications of physics-based modeling, microfluidics and microbiological experimentation can lead to a deep understanding of various pathways by which bacteria can penetrate into plant leaves.

The proposed physics-based models, as complementary to experiments, reveal the fundamental primary and secondary factors affecting the contamination processes that might lead to improvement of microbial safety of leafy greens. In this chapter, the most important environmental conditions that can trigger bacterial infiltration into leafy greens are discussed. This is followed by an introduction to the application of physics-based modeling and experimentation to address underlying pathways of contamination. Finally, the overall objectives and organization of this dissertation are discussed.

1.1 Environmental factors triggering bacterial infiltration into plant leaves

As leafy greens move from field to fork, they experience various temperature, humidity, pressure, and light conditions. These environmental conditions, during pre- and post-harvest processing, can trigger bacterial transport into the plant leaves and alter their growth in the leaf interior. Figure. 1.1 highlights some of these driving forces for bacterial transport into plant leaves that are of interest in this dissertation.

1.1.1 Pressure changes

Any mechanical pressure gradients across the leaf tissue can result in a water flow into the leaf interior and cause passive bacterial transport (i.e., bacteria flowing with the fluid) (Fig. 1.1b). For example, such a contamination pathway can happen during vacuum cooling process (Li et al., 2008; Vonasek and

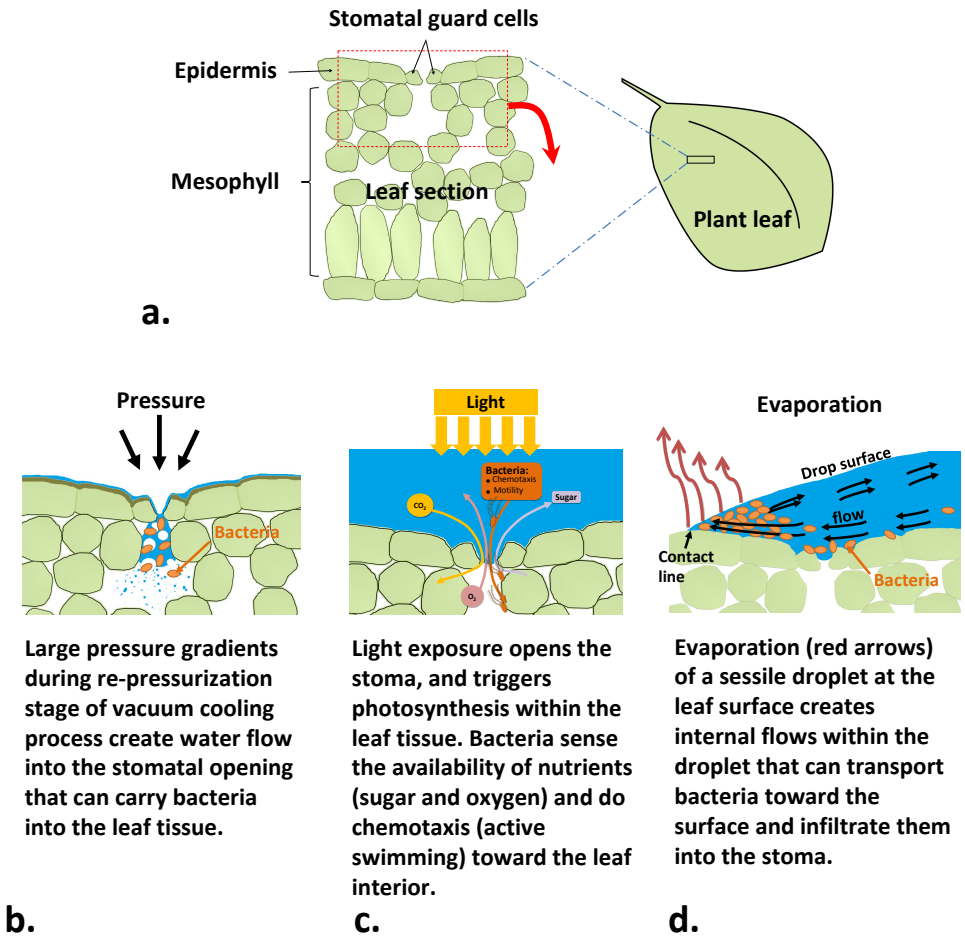

Figure 1.1: a) A schematic of a plant leaf and its cross section, b) Effect of changes in the environmental pressure on the bactrial infiltration into the leaf interior, c) Effect of light in triggering photosynthesis in the plant leaf that can induce bacterial chemotaxis toward the leaf interior, d) Effect of evaporation in creating flows within a surface sessile droplet that can facilitate bacterial retention close to the leaf surface and their infiltration into the stomatal opening.

Nitin, 2016) which is one of the fastest and most efficient pre-cooling practices during post-harvest processing of leafy greens. During re-pressurization stage (when vacuum returns to atmospheric) of this process, large pressure gradients forcibly push water into the leaf porous structure through any available openings at the leaf surface.

1.1.2 Light exposure

Light is one of the driving forces that can promote infiltration of pathogenic bacteria into plant leaves (Kroupitski et al., 2009) (Fig. 1.1c). Photosynthetically active cells in the leaf tissue produce nutrients during light exposure that are attractive food sources for bacteria that may be initially present at the leaf surface. Opening of the stomata in presence of light creates an opportunity for bacteria to do chemotaxis toward the gradients of these nutrients, thus leading into the leaf interior.

1.1.3 Evaporation of surface water

Evaporation of sessile droplets at surface of plant leaves is a process that frequently happens during growth period and post-harvest processing of leafy greens. Evaporation creates internal flows within a sessile droplet that can carry colloidal particles (Deegan et al., 1997) (Fig. 1.1d). On a leaf surface, these flows can transport microorganisms close to the surface and facilitate their adhesion to the surface microstructures such as trichomes, and infiltration into the available openings such as stomata, grooves and wounds.

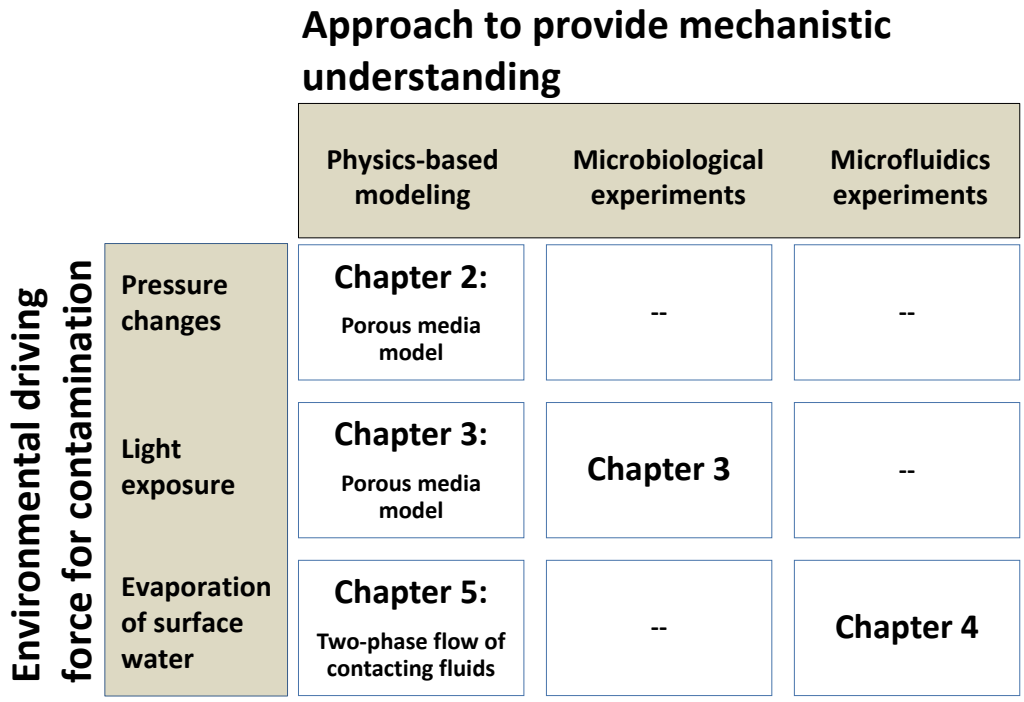

Figure 1.2: The three-pronged approach to provide mechanistic understanding of bacterial infiltration into leafy greens. Each chapter of the dissertation uses one or two of these approaches.

1.2 Mechanistic understanding of bacterial infiltration: a three-pronged approach

An interdisciplinary, three-pronged approach (Fig. 1.2) is taken here to provide a mechanistic understanding of bacterial infiltration into plant leaves as a result of environmental driving forces discussed in Sec. 1.1. Each chapter uses one or two of the approaches. This three-pronged approach includes: 1) Physics-based modeling, which is a mechanistic approach in which physical laws of conservation of mass, momentum and energy are applied to the bacterial contamination process, and predicts the response of the process (e.g., amount of bacterial infiltration) to change in the influencing parameters (e.g., changes in temperature,

pressure, and light exposure). For example, considering a leaf as a porous media, transport of bacteria within the leaf tissue can be modeled. Applying the physical laws to a biologically complex system, like a leaf, requires several simplifications and assumptions. The simplifications still correctly address all essential physics. 2) Microbiological experimentation, by which the infiltration of bacteria into real leaves are determined, and the response of various influencing factors to the amount of infiltration are studied. 3) Microfluidics experimentation, by which an experimental substrate (e.g., artificial surfaces surrogate to plant leaves) with prescribed properties (known roughness and hydrophobicity) can be fabricated, and used to study the response of the biological system to various influencing parameters. Here, patterned surfaces, that mimic microstructures (i.e., stomata, trichomes and grooves) and hydrphobicity at the surface of plant leaves, are fabricated and used to study how they impact the retention of bacteria close to the surface and their infiltration into the leaf tissue during evaporation of surface sessile droplets.

These approaches are used to develop a mechanistic relationship between the extent of contamination and various produce-bacteria-process parameters. The three approaches synergistically complement and validate each other.

1.3 Objectives

The effect of the environmental driving forces discussed in Sec. 1.1 on the bacterial contamination of leafy greens are separately studied here using the approaches described in Sec. 1.2. The specific objectives of this dissertation are:

- Using physics-based modeling to understand physical mechanisms of

contamination (retention/infiltration) of leafy greens as a result of environmental conditions (changes in the pressure, light exposure, and surface water evaporation).

- Conducting microbiological experiments on the light-driven and evaporation-driven infiltration of bacteria into plant leaves.
- Fabrication of patterned surfaces as surrogate of plant leaves, to study how evaporation of surface sessile droplets containing bacteria can lead to retention and infiltration into the leaf openings, and how surface microstructures and hydrophobicity can affect the contamination.

1.4 Organization of the dissertation

This dissertation is divided in five chapters:

Chapter 1: Introduction This chapter introduces the modeling and experimental approaches used in this dissertation to study bacterial contamination of leafy greens.

Chapter 2: Pressure-driven infiltration of water and bacteria into plant leaves during vacuum cooling: A mechanistic model In this chapter a mechanistic model for pressure-driven infiltration of bacteria into plant stomata during re-pressurization stage of vacuum cooling process is introduced. The model focuses on only one stomatal opening and solves the multi-phase transport of gas, water, vapor, and bacteria within the porous structure of a leaf tissue. It studies

the effects of vacuum cooling process parameters (e.g., vacuum level and re-pressurization rate), bacterial and leaf characteristics (e.g., bacterial motile ability, and leaf permeability to water penetration) on the total amount and depth of infiltration of bacteria into the leaf tissue.

Chapter 3: Mechanistic modeling of light-induced chemotactic infiltration of bacteria into leaf stomata In this chapter, by focusing on a single stomatal opening, a mechanistic model is developed for chemotactic transport of bacteria within a leaf tissue in response to the photosynthesis occurring within plant mesophyll and guard cells. This comprehensive model includes transport of carbon dioxide, oxygen, bicarbonate, sucrose/glucose, bacteria, and autoinducer-2 (a signaling molecule) within the leaf tissue. The model includes biological processes of carbon fixation in chloroplasts, and respiration in mitochondria of the plant cells, as well as motility, chemotaxis, nutrient consumption and communication in the bacterial community. The model studies the effects of various influencing process-bacterial-plant parameters on the bacterial infiltration into the leaf tissue. It also explains the effects of the plant stomatal defense on the microbial infiltration.

Chapter 4: Retention and infiltration of bacteria on a plant leaf driven by surface water evaporation This chapter presents experimental approaches to fabricate micro-patterned surfaces that mimic microstructures (stomata, trichomes, and grooves) and hydophobicity of plant leaves. The micro-patterned surfaces are used to study various mechanisms by which evaporation of surface sessile droplets containing bacteria can lead to retention of bacteria at a the various micro-structures on the surface and bacterial infiltration into available open-

ings. The findings from this experimental work is used to validate and support predictions obtained from a mechanistic model presented in Chapter 5.

Chapter 5: A mechanistic model for bacterial retention and infiltration on a leaf during a sessile droplet evaporation This chapter develops a mechanistic model for transport of bacteria within an evaporating sessile droplet located at the surface of a plant leaf. The model predicts the amount of retention of bacteria close to the leaf surface and their infiltration into stomatal openings. It solves for fluid flow within the droplet and surrounding gas, liquid-gas interface movements, heat transfer, transport of vapor in the gas phase, transport of bacteria (by fluid flow, and motility and chemotaxis towards nutrients), and sugar (glucose) within the water phase. The model studies the effects of various influencing process-bacterial-plant parameters on the bacterial retention and infiltration. Experimental data obtained in Chapter 4 are used to validate and support predictions of this model.

BIBLIOGRAPHY

[1] CDC. (2018). Centers for Disease Control and Prevention. E. coli O157:H7 Infections Linked to Romaine Lettuce. Retrieved from: https://www.cdc.gov/ecoli/2018/o157h7-04-18/map.html

[2] Deegan R.D., Bakajin, O., Dupont, T.F., Huber, G., Nagel, S.R., Witten, Th.A. (1997). Capillary flow as the cause of ring stains from dried liquid drops. Nature 389, 827-829.

[3] DeWaal, C.S., Bhuiya, F. (2007). Outbreaks by the Numbers: Fruits and Vegetables. 1990-2005, vol. 2012.

[4] Kroupitski,Y., Golberg, D., Belausov, E.,Pinto, R., Swartzberg, D., Granot, D., Sela, Sh. 2009. Internalization of Salmonella enterica in Leaves Is Induced by Light and Involves Chemotaxis and Penetration through Open Stomata. Applied and Environmental Microbiology, 6076-6086.

[5] Olaimat, A.N., Holley, R.A. (2012). Factors influencing the microbial safety of fresh produce: A review. Food Microbiology 32(1), 1-19.

[6] Vonasek, E., Nitin, N. (2016). Influence of vacuum cooling on Escherichia coli O157:H7 infiltration in fresh leafy greens via a multiphoton-imaging approach. Applied and Environmental Microbiology 82 (1), 106-115.

[7] Zhang GD, Ma L, Beuchat LR, Erickson MC, Phelan VH, Doyle MP. (2009). Lack of internalization of Escherichia coli O157:H7 in lettuce (Lactuca sativa). Journal of Food Protection 72 (10), 2028-2037.

CHAPTER 2

PRESSURE-DRIVEN INFILTRATION OF WATER AND BACTERIA INTO PLANT LEAVES DURING VACUUM COOLING: A MECHANISTIC MODEL

2.1 Abstract

Vacuum cooling of leafy greens can quickly lower their temperature, thus efficiently extending their shelf-life. However, passive bacterial infiltration into the leaf through openings such as stomata or wounds during this process presents a risk. This study develops a mechanistic model of stomatal infiltration and elaborates controlling parameters. Water and vapor phases transport in the leaf tissue as a porous medium, with convective flow driven by pressure changes outside the leaf, capillary diffusion of water and molecular diffusion of vapor. Water exchange between symplast and apoplast in the leaf is driven by pressure changes. Bacteria are convected with intercellular water, along with their motility. Heat transfer includes evaporation that varies with pressure. Increased water and bacterial infiltration are primarily caused by longer re-pressurization time, lower initial moisture content of the leaf and larger stomatal pores, and less so by increased vacuum level. Findings should help making vacuum cooling processes microbiologically safer.

2.2 Introduction

Global consumption of leafy greens has been on the rise over the past decades (Olaimat and Holley, 2012). Meanwhile, outbreaks of foodborne illnesses associated with contaminated leafy greens have increased. Leafy greens are among the most contaminated food products to norovirus, *Salmonella* and *Escherichia coli* (DeWaal and Bhuiya, 2007). From 2005 to 2011, there were 5415 outbreaks associated to vegetable sprouts and leafy greens, like spinach and lettuce, that 73% of which occurred in 2011 due to *E. coli* O104:H4 and *E. coli* O157:H7 (Olaimat and Holley, 2012). Very recently, the Centers for Disease Control and Prevention of the US (CDC, 2018) reported 210 *E. coli* O157:H7 infections linked to romaine lettuce. Infiltration of human pathogens into fresh leafy greens significantly increases the risk of foodborne illnesses, as the internalized microbes cannot be effectively removed or treated utilizing standard sanitation and washing processes (Zhang et al., 2009; Vonasek and Nitin, 2016).

Temperature is the most important factor in preserving the quality of fresh produce after harvest. Leafy greens like spinach and lettuce that have high surface-to-volume ratios can be rapidly cooled by vacuum cooling to reach a safe temperature level for storage (Ozturk and Ozturk, 2009). In vacuum cooling, chamber pressure falls below the equilibrium vapor pressure of water, leading to rapid evaporation of moisture from the surface and within the leaves, thus cooling the product.

While popular as a rapid cooling technique, vacuum cooling can promote infiltration of pathogenic microorganisms into fresh produce (Li et al., 2008; Vonasek and Nitin, 2016; Shynkaryk et al., 2016; Pyatkovskyy et al., 2017).

When pressure of the vacuum chamber transitions from vacuum to the atmospheric level, the generated pressure gradients within the leaf tissue can create a pressure-driven gas and/or water transport into the porous structure of the leaf through any available openings. As water is normally sprayed on the leaf surfaces to avoid moisture loss from evaporation (Thompson et al., 1998), one can expect presence of a water film at the leaf surface when the vacuum is broken. If the gas/water contains pathogenic microorganisms, they would be forcibly infiltrated within the leaf tissue. Indeed, such an infiltration mechanism is similar to that of vacuum impregnation practices in which bacteria are artificially impregnated into leaves to study their mutual interactions (Simmons et al., 2009).

The main routes of infiltration into leafy greens include stomata, cuts, and wounds at the leaf surface (Li et al., 2008). Various factors can affect the amount and depth of bacterial infiltration: 1) Transport properties of water and bacteria within the leaf tissue. For example, capillary diffusivity of water within the porous structure of the leaf, and random motility of bacteria. 2) Leaf characteristics such as permeability of the mesophyll tissue to water, initial moisture content, stomatal opening size, and leaf side. 3) Process parameters including presence of water at the leaf surface, vacuum level, vacuum duration, and repressurization duration. However, the effects of these factors on the amount and depth of infiltration into leafy greens are not well-understood. Mechanistic understanding of the role of each of the involved factors can help in better prevention of contamination of leafy greens by pathogenic microorganisms.

2.2.1 Objectives

The reported evidence (Li et al., 2008; Vonasek and Nitin, 2016) leaves us with a concern about enhancement of pathogen infiltration into leafy greens during the vacuum cooling process. This emphasizes the need for a better understanding of the infiltration mechanisms and identification of the risk factors contributing to foodborne outbreaks. To that end, this work aims to introduce a mechanistic modeling approach that can delineate the involved mechanisms and clearly show the effects of the process parameters, transport properties, and leaf structural features on the microbial infiltration. It was hypothesized that pressure gradients generated during re-pressurization stage of the vacuum cooling process are the driving force for water and bacterial infiltration into the stomatal opening, leading to the following objectives of this study: 1) Development of a porous medium-based model to explain how water and bacteria can infiltrate into the leaf tissue through the stomatal opening during the re-pressurization stage of the vacuum cooling process, 2) Validation of the model predictions against literature data for leaf temperature, pressure, moisture content and the amount of infiltrated bacteria, and 3) Identification of the effects of the most important parameters related to the leaf, process and transport, on the bacterial infiltration.

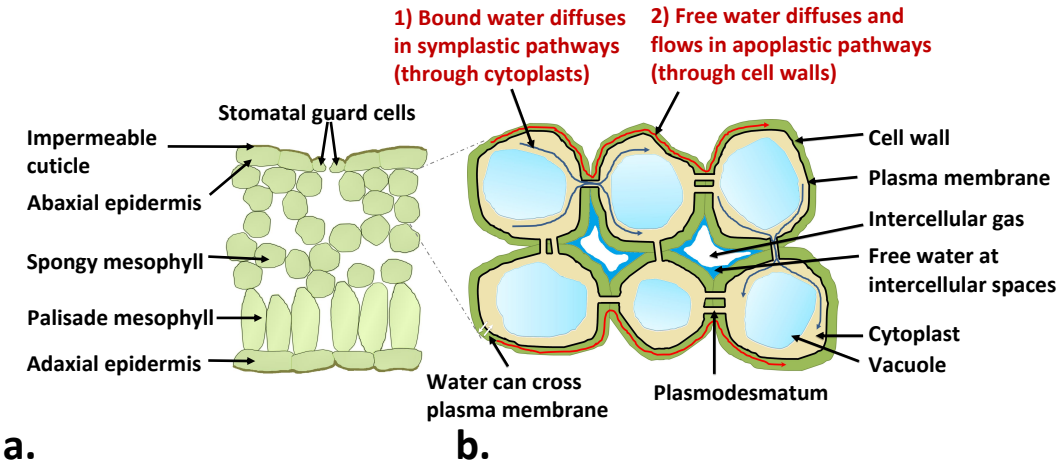

Figure 2.1: a) Various components of a leaf cross section, and b) symplastic and apoplastic water transport in a leaf with water exchange across plasma membrane.

2.3 Model formulation

2.3.1 Leaf section structure

Figure 2.1a shows different components of a leaf section. At the regions where veins are not present, a leaf section contains a mesophyll layer in the middle and two epidermis layers at the top and bottom sides that are covered by a waxy cuticle layer. The mesophyll contains palisade and spongy cells. Most of the surface areas of both spongy and palisade mesophyll cells are exposed to air in the intracellular spaces (Nobel, 2005). The spongy cells are loosely packed but palisade cells are tightly packed. Therefore, one can consider the mesophyll as a porous zone with two different gas porosities. Gas exchange between the interior region of the leaf and outside environment takes place through stomatal openings that are controlled by a pair of guard cells. The movement of water among plant cells takes place by two different routes (Fig. 2.1b): 1) the

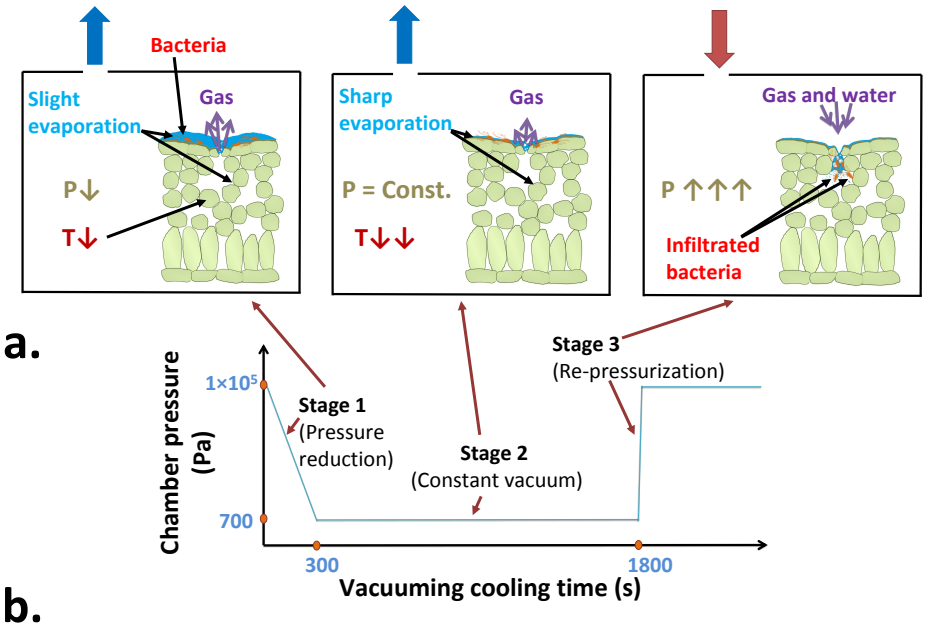

Figure 2.2: a) Vacuum cooling stages, and b) vacuum chamber pressure history during the stages.

symplastic pathways in which water is transported within cytoplasms through plasmodesmata. This water presents within the vacuole of plant cells and here is considered as bound water, and 2) the apoplastic pathways that are spaces outside of plasma membrane in which water is freely transported within connected cell walls of adjacent cells (Dymek, 2015; Nobel, 2005). The apoplast has often implicitly assumed to be dominated by bulk flow rather than a molecular diffusion (Evert et al., 1985; Buckley, 2015). Therefore, free water was assumed to be present at the intercellular spaces and apoplastic pathways whereas bound water fills the intracellular regions (Fig. 2.1b), *i.e.*, within protoplast that contains vacuole and cytoplasm (Maurel, 1997).

2.3.2 Problem description

Pressure history and physical schematic

A common vacuum cooling process includes three successive stages (Fig. 2.2a): at stage 1, the pressure of the chamber is dropped from atmospheric pressure to around 700 Pa (Fig. 2.2b). The produce temperature may reduce due to convective heat transfer and some evaporation effects. At stage 2, there is a constant pressure condition. As the pressure is below the equilibrium vapor pressure of water, a sharp evaporation takes place at the leaf surface and within its porous structure, leading to a rapid cooling of the produce. After about 30 min, when the temperature of the produce reaches to a safe level for storage, the chamber pressure is restored. This is stage 3 within which water and gas might passively infiltrate into the produce through wounds, stomata, or other openings and cuts, due to large pressure gradients generated during re-pressurization. Such a pressure-driven infiltration of gas and water may cause microorganisms present within the water film at the leaf surface to get passively transported into the produce tissue.

Computational schematic and assumptions

A schematic of the computational problem is shown in Fig. 2.3a. A 2D-axisymmetric domain around one stomate was used as the computational domain. The leaf section was modeled as an unsaturated porous medium containing solids, free water, bound water, vapor, and air phases (Fig. 2.3b). As the mesophyll tissue is the dominant part in the leaf section, it was assumed that the entire leaf section has the properties of the mesophyll region. Shrinkage and

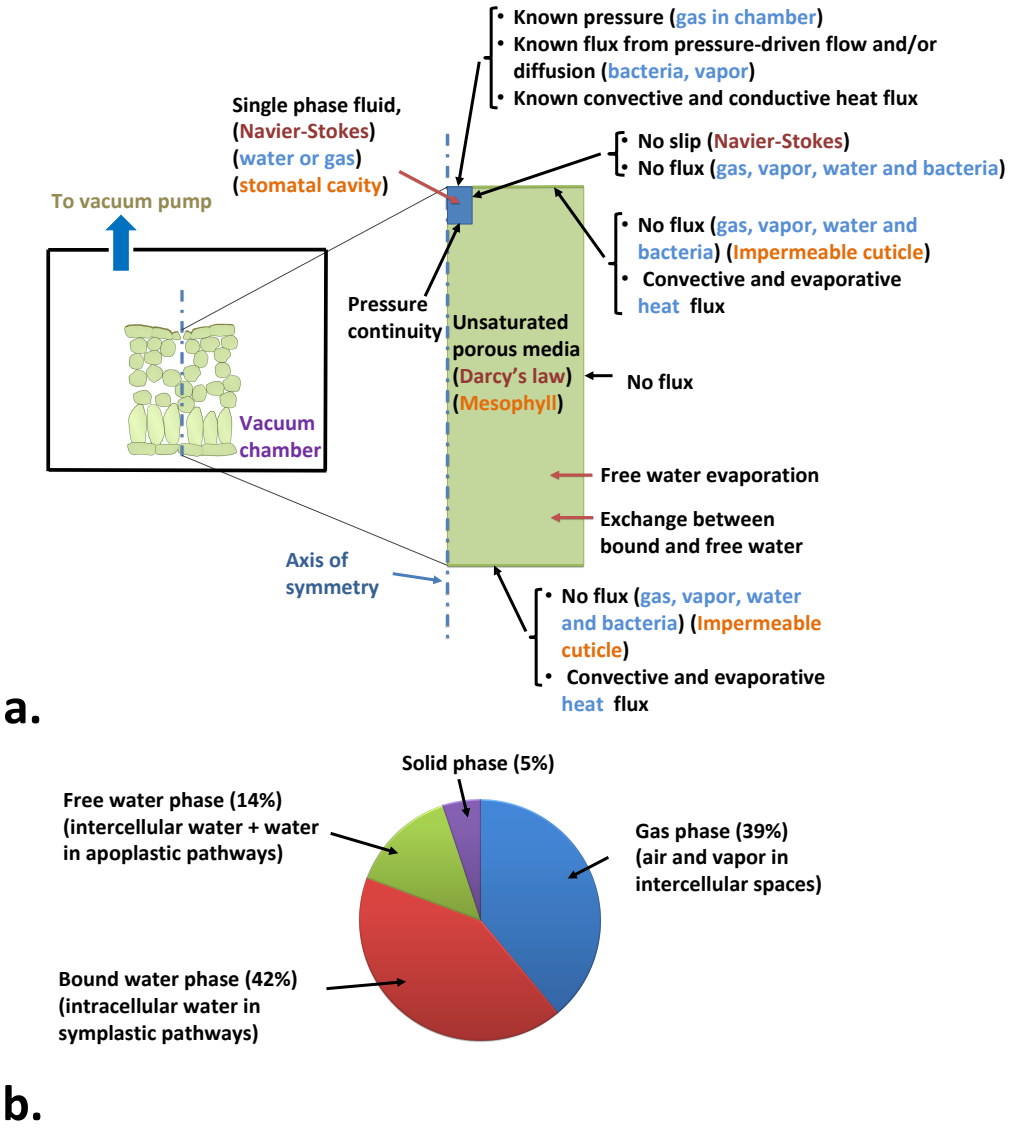

Figure 2.3: a) Model schematic showing the physical (left) and computational (right) solution domain, and b) volume fractions of various phases in a computational representative elementary volume located in the spongy mesophyll region.

changes in porosity of the mesophyll tissue during vacuuming was neglected. The profile of chamber pressure was applied as a boundary condition for the single phase fluid region (stomatal cavity; Fig. 2.2b). Vacuum can forcibly keep the stomata open (Li et al., 2008), which supports the assumption that stomata are open enough at the start of re-pressurization process. It was assumed that when the chamber is under vacuum, the stomatal cavity is filled only by gas, and during re-pressurization, it only contains water. This assumption was made to avoid application of a multiphase fluid flow formulation at the stomatal cavity region. The top and bottom boundaries (leaf surfaces) are assumed to implicitly be covered by a layer of water during the entire process. This is not unlikely as water is normally sprayed on the produce surface during the vacuum cooling process to avoid excessive weight loss and quality deterioration (Vonasek and Nitin, 2016). The effect of leaf wettability on the amount of water infiltration was ignored as the pressure exerted on the leaf during re-pressurization stage is much larger than the minimum pressure required for penetration of water into stomata (Schonherr and Bukovac, 1972). Active plant-microbe interactions such as bacterial chemotaxis toward plant nutrients are not considered here, as the timescale of these active interactions (several minutes to hours) are much longer than that of the re-pressurization stage (few seconds to few minutes) in which bacterial transport is studied here.

Qualitative description of the transport processes

During stages 1 and 2, the generated pressure gradients within the leaf section cause the gas containing air and vapor to be sucked out from the stomatal cavity and mesophyll regions (Fig. 2.3a). These pressure gradients, as well as capillary

diffusion, are the driving forces for transport of free water within the porous structure. Free water can evaporate and generate vapor within the porous media region (mesophyll). The vapor is transported by the gas flow and binary diffusion in air. Relative humidity and temperature histories within a vacuum chamber measured by Ozturk and Ozturk (2009) were used to calculate the vapor mass fraction at the stomatal opening boundary. The bound water which exists within the intracellular region can be transported via molecular diffusion. As a result of vacuum at intercellular spaces, the bound water can cross the plasma membrane and join the free water (Fig. 2.1b). During stage 3, water carrying bacteria enters the stomatal cavity from the stomatal opening boundary followed by penetration into the mesophyll tissue. Bacteria can also transport via diffusion (motile/Brownian motions) within the domain. The top and bottom boundaries (leaf surfaces) are impermeable to the gas, water and bacteria due to the presence of the waxy cuticle layer. Leaf temperature is described by an energy balance over the entire domain. The evaporation of free water within the mesophyll tissue causes a rapid cooling effect within the leaf during stages 1 and 2. At the stomatal opening boundary, heat is transfered out of the domain by gas outflow. In addition, heat can be exchanged via convective and evaporative heat fluxes between leaf surfaces and the chamber environment.

2.3.3 Governing equations

A big picture of the model

An overview of the model is depicted in Fig. 2.4. To simulate the mass (water, vapor, air, and bacteria), momentum and heat transfer in the mesophyll region, a

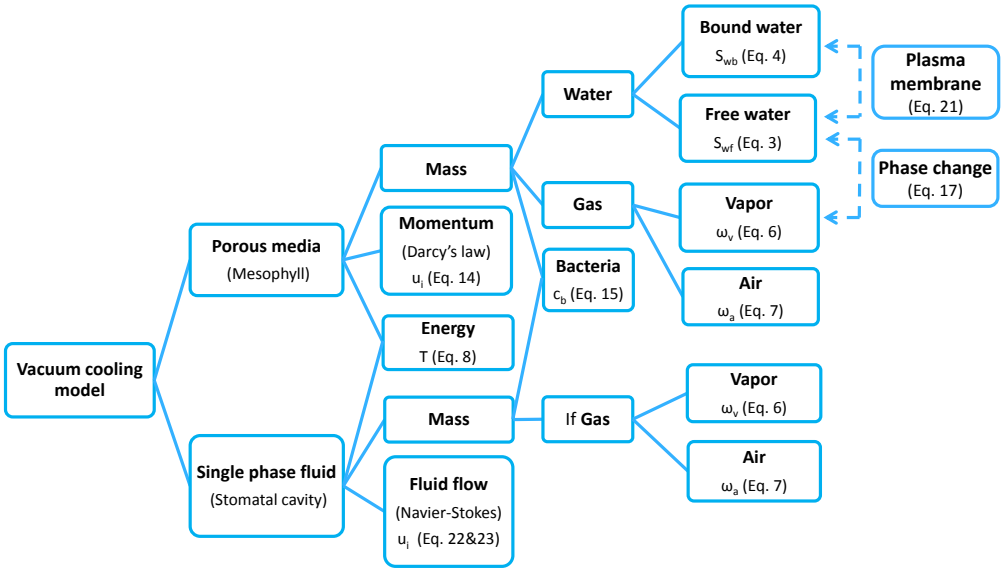

Figure 2.4: An overview of the model.

multiphase porous media-based model was applied. The pressure-driven flow of the fluids (except for bound water that can only diffuse) was modeled by Darcy's law within the porous zone and by Navier-Stokes equations within the single phase fluid region. The interspecies couplings (*i.e.*, bound to free water exchange, free water evaporation, evaporative cooling) were implemented by using a number of source terms.

Basic definitions

The porosity, ϕ, at any point inside the mesophyll is defined as the volume fraction occupied by fluid phases:

$$\phi(r,z) = \frac{1}{\delta V}\sum_{i} \delta V_i \tag{2.1}$$

with $i = wf, wb, g$ representing free water, bound water and gas phases, respectively. δV_i is the volume occupied by ith phase in the elemental volume, δV.

Saturation of each fluid phase, S_i, is defined as the fraction of the total fluid volume occupied by each fluid:

$$S_i(r,z) = \frac{\delta V_i}{\phi(r,z)\delta V} \tag{2.2}$$

Free water in mesophyll tissues

Free water within the pores can be transported either through capillary diffusion, due to concentration gradients, or pressure-driven Darcy flow. The mass balance for free water is given by:

$$\frac{\partial}{\partial t}(\phi\rho_w S_{wf}) + \nabla\cdot(\mathbf{u}_w\rho_w) = \nabla\cdot(D_{w,cap}\nabla(\phi\rho_w S_{wf})) - \dot{I}_v + \dot{J}_{w,bf} \tag{2.3}$$

where t is time (s), ρ_w is water density (kg/m^3), $\mathbf{u}_w$ is velocity of free water (m/s), $D_{w,cap}$ is capillary diffusivity of free water in pores (m^2/s), $\dot{I}_v$ is the rate of evaporation of free water (kg/m$^3\cdot$s), and $\dot{J}_{w,bf}$ is the rate of water exchange across the cell plasma membrane (*i.e.*, bound water to free water) within the mesophyll region (kg/m$^3\cdot$s).

Bound water in mesophyll tissues

Bound water transports through symplastic pathways by molecular diffusion. If there is a water potential difference across the plasma membrane, it passes the membrane to join the apoplastic free water. The transport of bound water within the porous zone is described as:

$$\frac{\partial}{\partial t}(\phi\rho_w S_{wb}) = \nabla\cdot(D_{w,p}\nabla(\phi\rho_w S_{wb})) - \dot{J}_{w,bf} \tag{2.4}$$

where $D_{w,p}$ is the diffusion coefficient of water in the protoplast (m^2/s), which was assumed to be equal to the self-diffusion coefficient of water (Wang, 1965),

$D_{w,w}$; as the protoplast is mainly occupied by vacuole (Nobel, 2005).

Vapor and air in the leaf section

The saturation of the gas phase, S_g, is obtained from:

$$S_g = 1 - (S_{wf} + S_{wb}) \tag{2.5}$$

In the gas phase, by considering a binary diffusion for water vapor and air, one can solve for their respective mass fractions (ω_v and ω_a) using

$$\frac{\partial}{\partial t}(\phi \rho_g S_g \omega_v) + \nabla \cdot (\mathbf{u}_g \rho_g \omega_v) = \nabla \cdot (\phi S_g \frac{C_g^2}{\rho_g} M_a M_v D_{g,eff} \nabla x_v) + \dot{I}_v \tag{2.6}$$

and

$$\omega_a + \omega_v = 1 \tag{2.7}$$

Here, ρ_g is gas density (kg/m^3), $\mathbf{u}_g$ is the velocity of gas (m/s), $D_{g,eff}$ is the diffusion coefficient of vapor in air (m^2/s), C_g is the molar density of gas (mol/m^3), M_a and M_v are molar masses of air and vapor (kg/mol), respectively, and $x_v = p_v/P$ is the mole fraction of vapor defined as the ratio of vapor pressure to the gas pressure.

Heat balance in the leaf section

A thermal energy balance is used to solve for temperature at any point within the leaf section with assumption that all phases are in thermal equilibrium:

$$\rho_{eff} C_{p_{eff}} \frac{\partial T}{\partial t} + (\rho C_p \mathbf{u})_{fluid} \cdot \nabla T = \nabla \cdot (k_{eff} \nabla T) - \lambda \dot{I}_v \tag{2.8}$$

with effective properties being defined as:

$$\rho_{eff} = (1 - \phi)\rho_s + \phi \left((S_{wf} + S_{wb})\rho_w + S_g \rho_g \right) \tag{2.9}$$

$$k_{eff} = (1-\phi)k_s + \phi\left((S_{wf}+S_{wb})k_w + S_g k_g\right) \tag{2.10}$$

$$C_{p_{eff}} = m_s C_{p_s} + m_g(\omega_a C_{p_a} + \omega_v C_{p_v}) + m_w C_{p_w} \tag{2.11}$$

$$(\rho C_p \mathbf{u})_{fluid} = \left(\rho_w \mathbf{u}_{wf} - D_{w,cap}\nabla(\phi\rho_w S_{wf}) - D_{w,p}\nabla(\phi\rho_w S_{wb})\right) C_{p_w} + \rho_g \mathbf{u}_g(\omega_v C_{p_v} + \omega_a C_{p_a}) \tag{2.12}$$

where T is temperature (K), λ is latent heat of vaporization of water (J/kg), k is thermal conductivity (J/m $\cdot$ K $\cdot$ s), C_p is the specific heat capacity (J/kg $\cdot$ K), and m is overall mass fraction of each phase. Subscripts a, v, w, and s, indicate air, vapor, water and solid phases. Note that Eq. (2.8) is valid in the porous media (mesophyll). In the stomatal opening region, a similar equation to Eq. (2.8) was used, but for heat transfer in a single-phase fluid (gas in stages 1 and 2).

Pressure in the mesophyll tissue

Distribution of the gas pressure, P, within the mesophyll region is obtained from the following conservation equation:

$$\frac{\partial}{\partial t}(\phi\rho_g S_g) + \nabla\cdot\left(-\rho_g\frac{\kappa_g}{\eta_g}\nabla P\right) = \dot{I}_v \tag{2.13}$$

with Darcy's law providing superficial velocity of each species i:

$$\mathbf{u}_i = -\frac{\kappa_i}{\eta_i}\nabla P \tag{2.14}$$

where i is either gas or free water, η_i is the dynamic viscosity (Pa $\cdot$ s) of species i, and κ_i is the permeability of mesophyll tissue to species i (m^2).

Bacterial transport

The gas pressure gradients within the vacuum chamber push the water at the leaf surface into the stomatal opening during the re-pressurization stage. In the

absence of any stimulus, motile bacteria undergo a random walk motion known as tumbles that is modeled as a diffusion-like transport mechanism (Tindall et al., 2008). If the bacteria are non-motile, they still have the Brownian random motion due to collisions with fast-moving molecules within the liquid phase. Both of the above random mechanisms are modeled by a diffusive transport term in Eq. (2.15). So, the mechanisms of infiltration includes the transport with the flow of water as well as diffusion (motility/Brownian) of bacteria within water. The conservation equation for bacterial transport in the leaf section can be written as:

$$\frac{\partial(c_b \phi S_{wf})}{\partial t} + \nabla \cdot (\mathbf{u}_b c_b) = \nabla \cdot (D_{b,eff} \nabla (c_b \phi S_{wf})) \tag{2.15}$$

where c_b is the bacterial concentration (CFU/m^3), and $D_{b,eff}$ is bacterial effective diffusivity (m^2/s) which depends on the porosity and free water saturation. It represents the coefficient of random motility (if the bacteria are motile; Tindall et al., 2008) in free water phase. Bacterial velocity, $\mathbf{u}_b$, was adapted by an inhibition function (Shirai et al., 2017) in order to account for the effect of bacterial concentration on their transport in the fluid:

$$\mathbf{u}_b = \left(1 - \frac{c_b}{c_{b,max}}\right) \mathbf{u}_w \tag{2.16}$$

where $c_{b,max}$ is the maximum allowable concentration of bacteria beyond which they cannot be transported by the fluid due to clogging effects. By considering the ratio of the volumes of the stomatal cavity to a single bacterial cell (*E. coli* has a typical dimension of 0.5 μm in radius and 3 μm in length (Zaritsky and Woldringh, 1987)), the $c_{b,max}$ was estimated as 1×10^{18} CFU/m^3.

Free water evaporation in the mesophyll tissue

Rate of change of free water to water vapor is calculated by the following non-equilibrium equation (Halder et al., 2007):

$$\dot{I_v} = K(p_{v,eq} - x_v P)\frac{M_v S_g \phi}{RT} \tag{2.17}$$

where K is evaporation constant (1/s), R is the universal gas constant (J/mol$\cdot$K), and $p_{v,eq}$ is equilibrium vapor pressure (Pa),

$$p_{v,eq} = a_w p_{v,sat} \tag{2.18}$$

which depends on the moisture-dependent local water activity, a_w, of the leaf tissue, and saturation vapor pressure of water (Murray, 1967),

$$p_{v,sat} = \frac{101325}{760} \times 10^{\left(8.07131 - \frac{1730.63}{T - 39.574}\right)} \tag{2.19}$$

Water exchange across plasma membrane

Based on a conservation of mass across plasma membrane, the time evolution of the cell volume, V_c, equals the rate of water exchange across plasma membrane surface area, A_c (Buckley, 2015). Considering a cell as an elastic shell having a constant osmotic potential, π_0, the rate of change in cell pressure, p_{wb}, is related to the rate of change in its volume (Nobel, 2005):

$$\frac{\partial p_{wb}}{\partial t} = \frac{\epsilon}{V_c}\frac{\partial V_c}{\partial t} = \frac{\gamma\, V_w \epsilon}{RT}\alpha_p(\psi_{wf} - \psi_{wb}) \tag{2.20}$$

where ϵ is the volumetric elastic modulus of the cell wall (Pa), γ is the osmotic water permeability of plasma membrane (m^3/m$^2\cdot$s), V_w is the molar volume of water (m^3/mol), ψ_{wb} and ψ_{wf} are water potentials (Pa) in symplast and apoplast, respectively, and $\alpha_p = A_c/V_c$ is the specific surface area of the porous tissue of

the leaf (m^2/m^3). Water potential in the symplast includes the internal cell pressure (turgor pressure) and its osmotic potential, $\psi_{wb} = p_{wb} + \pi_0$. Assuming a negligible concentration of solutes within the apoplast, one can write $\psi_{wf} \approx p_{wf}$. Given the internal cell pressure, the volumetric rate of water exchange, $\dot{J}_{w,bf}$ ($kg/m^3 \cdot s$), across plasma membrane is calculated as:

$$\dot{J}_{w,bf} = \frac{\gamma \rho_w V_w}{RT} \alpha_p \left(\psi_{wb} - \psi_{wf} \right) \tag{2.21}$$

Gas/water flow in stomatal cavity

At the stomatal cavity, velocity and pressure of a single-phase incompressible fluid (i: gas or water) are solved by the Navier-Stokes equation, assuming a laminar flow regime:

$$\rho_i \frac{\partial \mathbf{u}_i}{\partial t} + \rho_i \mathbf{u}_i \cdot \nabla \mathbf{u}_i = -\nabla P + \eta_i \nabla^2 \mathbf{u}_i \tag{2.22}$$

with

$$\nabla \cdot \mathbf{u}_i = 0 \tag{2.23}$$

During stages 1 and 2, the fluid is gas, while at stage 3, it is water.

2.3.4 Initial and boundary conditions

The initial pressure within the leaf structure was set to 1 atm. The initial leaf temperature was set to a constant value, *e.g.* 25 °C. Gas velocity at the stomatal cavity was initially zero. The initial saturations of all phases were calculated in Section 2.3.5. The initial mass fraction of the vapor was calculated to be 0.026 based on the assumption of having initial moisture equilibrium between free

water and gas:

$$\omega_{v,eq} = \frac{x_{v,eq} M_v}{x_{v,eq} M_v + (1 - x_{v,eq}) M_a} \tag{2.24}$$

where $x_{v,eq} = p_{v,eq}/P$ was calculated from Eq. (2.18) and Eq. (2.19). The subscript *eq* indicates the equilibrium condition. The concentration of bacteria within the leaf was initially zero. The initial water potential difference across cells plasma membrane was set to zero. As the boundary conditions for various stages of vacuum cooling process were different (Fig. 2.3a), they are elaborated below.

Stages 1 and 2

During stages 1 and 2, the fluid flowing within the stomatal cavity has the properties of gas. For the Navier-Stokes equation (Eq. 2.22), at the top boundary of the stomatal cavity, gas pressure, $P_{stoma,top}$, is set to that of vacuum chamber, P_{chmb}, (see Fig. 2.2b)

$$P_{stoma,top} = P_{chmb} \tag{2.25}$$

and at the bottom boundary of the stomatal cavity, the pressure continuity between stomatal cavity, $P_{stoma,btm}$, and the mesophyll region, P_{mes}, is assumed:

$$P_{stoma,btm} = P_{mes} \tag{2.26}$$

All other boundaries in the mesophyll region are impermeable to the fluids, and therefore zero flux conditions are set for them.

Vapor balance equation (Eq. 2.6) is solved within the entire domain including stomatal cavity and mesophyll region. At the stomatal opening, flux of the vapor ($\mathrm{kg/m^2 \cdot s}$) is:

$$\mathbf{n}_{v,stoma,top} = \rho_g \mathbf{u}_g \omega_v - \frac{C_g^2}{\rho_g} M_a M_v D_{g,eff} \nabla x_v \tag{2.27}$$

For all other boundaries, the vapor flux is zero.

Free water and bound water balance equations (Eqs. 2.3 and 2.4, respectively) are solved only in the mesophyll region. At all boundaries, zero flux conditions are used for both.

Heat transfer equation (Eq. 2.8) is solved for the entire domain. At the stomatal opening, heat flux ($J/m^2 \cdot s$) includes heat transfer by bulk flow and thermal conduction in the gas:

$$q_{stoma,top} = \rho_g \mathbf{u}_g (\omega_v C_{p_v} + \omega_a C_{p_a}) T - k_g \nabla T \tag{2.28}$$

and, at the top and bottom surfaces of the leaf, there is convective heat transfer from air within the vacuum chamber to the leaf, and a heat loss due to the evaporation of water film at the leaf surface. So, heat flux ($J/m^2 \cdot s$) at the leaf surfaces is defined as:

$$q_{surf} = h_t (T_{chmb} - T) - h_m \lambda (\rho_{v,sat} - \rho_{v,chmb}) \tag{2.29}$$

where h_t and h_m are the heat transfer coefficient ($J/m^2 \cdot K \cdot S$) and mass transfer coefficient (m/s) at the leaf surface, respectively. T_{chmb} and $\rho_{v,chmb}$ are temperature (K) and vapor density (kg/m^3) of gas in the vacuum chamber. $\rho_{v,chmb}$ is dynamically updated based on the experimental profile of temperature and relative humidity of gas within a vacuum chamber (Ozturk and Ozturk, 2009). $\rho_{v,sat}$ is saturation vapor density of water (kg/m^3).

During stages 1 and 2, the bacterial flux through the stomatal opening is zero.

Stage 3

At this stage the fluid within the stomatal cavity region is water. The boundary conditions for the Navier-Stokes equation (Eq. 2.22) at the top boundary of the stomatal cavity are described by Eq.(2.25). However, in stage 3, the chamber pressure is increasing from the target vacuum level to the atmospheric pressure (Fig. 2.2b). At the bottom boundary of the stomatal cavity, there is a pressure continuity condition (Eq. 2.26).

Flux of water (kg/m^2.s) entering the mesophyll tissue is equal to the flux of water leaving the bottom boundary of the stomatal cavity, obtained from the Navier-Stokes equation:

$$\mathbf{n}_{w,mes} = \rho_w \mathbf{u}_{w,stoma,btm} \tag{2.30}$$

Flux of bacteria (CFU/m$^2 \cdot$ s) entering the top boundary of the stomatal cavity with water is defined as:

$$\mathbf{n}_{b,stoma,top} = c_b \mathbf{u}_{b,stoma,top} \tag{2.31}$$

2.3.5 Input parameters

The input parameters used for simulating the vacuum cooling process with microbial infiltration are summarized in Table 2.1. Details of some of the input parameters are described here.

Table 2.1: Input Parameters

Parameter	Symbol	Value	Units	Source
Dimensions				
Stomatal opening diameter	D_{stoma}	$10 - 20 \times 10^{-6}$	m	Iwabuchi and Kurata, 2003, Li et al. (2008)
Stomatal opening depth	H_{stoma}	30×10^{-6}	m	Dymek et al. (2015)
Leaf depth	H_{domain}	300×10^{-6}	m	Dymek et al. (2015)
Distance from axis of symmetry	R_{domain}	80×10^{-6}	m	Assumed
Mass fractions of solid components (ζ)				
Carbohydrate	ω_{carb}	0.0363(spinach), 0.0329(lettuce)	kg/kg	USDA (2016)
Fat	ω_{fat}	0.0039(spinach), 0.0030(lettuce)	kg/kg	USDA (2016)
Protein	ω_{prot}	0.0286(spinach), 0.0123(lettuce)	kg/kg	USDA (2016)
Fiber	ω_{fib}	0.0220(spinach), 0.0210(lettuce)	kg/kg	USDA (2016)
Ash	ω_{ash}	0.0090(spinach), 0.0034(lettuce)	kg/kg	USDA (2016)
Density				

Water	ρ_w	998	kg/m^3	Rahman (2005)
Vapor	ρ_v	Ideal gas	kg/m^3	Gulati and Datta (2013)
Air	ρ_a	Ideal gas	kg/m^3	Gulati and Datta (2013)
Solids	ρ_s	$\frac{\sum_{i\in\zeta}\omega_i}{\sum_{i\in\zeta}\frac{\omega_i}{\rho_i}}$	kg/m^3	Gulati and Datta (2013)
Porosity				
Spongy mesophyll	ϕ_{spg}	0.95(spinach), 0.975(lettuce)	m^3/m^3	Calculated
Palisade mesophyll	ϕ_{pls}	0.95(spinach), 0.975(lettuce)	m^3/m^3	Calculated
Initial saturations				
Spongy mesophyll, gas	$S_{g,spg}$	0.41(spinach), 0.40(lettuce)	m^3/m^3	Calculated
Spongy mesophyll, free water	$S_{wf,spg}$	0.15(spinach), 0.15(lettuce)	m^3/m^3	Calculated
Spongy mesophyll, bound water	$S_{wb,spg}$	0.44(spinach), 0.45(lettuce)	m^3/m^3	Calculated
Palisade mesophyll, gas	$S_{g,pls}$	0.20(spinach), 0.19(lettuce)	m^3/m^3	Calculated
Palisade mesophyll, free water	$S_{wf,pls}$	0.15(spinach), 0.15(lettuce)	m^3/m^3	Calculated

Palisade mesophyll, bound water	$S_{wb,pls}$	0.65(spinach), 0.66(lettuce)	m^3/m^3	Calculated
Intrinsic permeability				
Spongy mesophyll to free water	$\kappa_{wf,in,spg}$	1×10^{-12}	m^2	Calculated
Palisade mesophyll to free water	$\kappa_{wf,in,pls}$	1×10^{-16}	m^2	Calculated
Mesophyll to gas	$\kappa_{g,in}$	Eq. (2.34)	m^2	Tanikawa and Shimamoto (2009)
Relative permeability				
Water	$\kappa_{w,r}$	Eq. (2.35)		Bear (1972)
Gas	$\kappa_{g,r}$	Eq. (2.36)		Bear (1972)
Specific heat capacity				
Water	C_{p_w}	4176	J/kg.K	Rahman (2010)
Vapor	C_{p_v}	1793	J/kg.K	Rahman (2010)
Air	C_{p_a}	1005	J/kg.K	Rahman (2010)
Solids	C_{p_s}	$\sum_{i \in \zeta} \omega_i C_{p_i}$	J/kg.K	Gulati and Datta (2013)

Thermal conductivity				
Water	k_w	0.60	W/m.K	Rahman (2010)
Vapor	k_v	0.026	W/m.K	Rahman (2010)
Air	k_a	0.026	W/m.K	Rahman (2010)
Solids	k_s	$0.5\left(\frac{\sum_{i\in\zeta}\omega_i}{\sum_{i\in\zeta}\frac{\omega_i}{k_i}}+\sum_{i\in\zeta}\omega_i k_i\right)$	W/m.K	Gulati and Datta (2013)
Viscosity				
Water	μ_w	9.27×10^{-4}	Pa.s	McCabe etal.(1956)
Gas	μ_g	1.80×10^{-5}	Pa.s	McCabe etal.(1956)
Water activity	a_w	$1-exp\,(-c(T-273.15)M^n)$ $c=-9\times10^{-6}(T-273.15)^2$ $+0.0007(T-273.15)+0.0143$ $n=0.0004(T-273.15)^2$ $-0.0354(T-273.15)+2.068$		Foke, 2013
Water capillary diffusivity	$D_{w,cap}$	1×10^{-9}	m^2/s	Calculated
Water self diffusivity	$D_{w,w}$	1×10^{-9}	m^2/s	Wang (1965)

Vapor diffusivity in air	$D_{g,eff}$	Eq. (2.41)	m^2/s	Millington and Quirk (1961)
Bacterial diffusivity	$D_{b,eff}$	1×10^{-11}	m^2/s	Warning et al. (2016)
Latent heat of vaporization of water	λ	2.26×10^6	J/kg	Warning et al. (2016)
Evaporation constant	K	100	1/s	Assumed
Osmotic water permeability of plasma membrane	γ	40×10^{-6}	$m^3/m^2.s$	Buckley (2015)
Osmotic potential of cell at reference state	π_0	-0.95×10^6	Pa	Santakumari and Berkowitz (1989)
Volumetric elastic modulus of cell wall	ϵ	0.25×10^6	Pa	Nobel (2005)
Specific surface area of porous zone	α_p	$\left(\frac{\left((S_g+S_{wf})\phi\right)^3}{5\kappa_{wf}\left(1-(S_g+S_{wf})\phi\right)^2}\right)^{0.5}$	m^2/m^3	Rahman (2005)

Solid fraction properties

The USDA composition database (USDA, 2016) was used to calculate the effective properties (Gulati and Datta, 2013) for solid fraction of spinach and lettuce based on their respective solid components (*i.e.*, carbohydrates, proteins, lipids, fiber, and ash).

Porosities and initial saturations

According to the USDA database, about 10% solid content is available within the spinach leaves, which is equivalent to about 5% solids volume fraction. Therefore, within the spinach leaves, the total porosity (including free water, bound water and gas volume fractions) can be estimated as about 0.95, which is comparable with a value of 0.90 for a leafy vegetable (Song et al., 2016). The gas porosity values within the spongy and palisade mesophyll were assumed to be 0.39 and 0.19 (Buckley, 2015), respectively. Therefore, the respective initial saturations of the gas were calculated as 0.41 and 0.20. A saturation of 0.15 for free water was adopted in both mesophyll regions based on the available microscopic images and volume fractions of subcellular components in plant leaves (Pearce and Beckett, 1985; Warmbrodt and VanDer Woude, 1990; Winter et al., 1994). Therefore, the saturations of bound water for spongy and palisade tissues were found to be 0.44 and 0.65, respectively. The respective values for lettuce leaf with solid content of about 5% were estimated by the same approach and are shown in Table 2.1.

Permeabilities

The permeability of the porous media to species i is defined as the product of an intrinsic permeability, $\kappa_{i,in}$ (m^2), and relative permeability, $\kappa_{i,r}$:

$$\kappa_i = \kappa_{i,in}\kappa_{i,r} \tag{2.32}$$

To estimate the intrinsic permeability of the mesophyll tissue to water, the bundle of tubes model, $\kappa_{wf,in} = n_t \pi R_t^4/(24\tau)$ (Bear, 1972), was used. Here, R_t is the tube radius (m), τ is the tortuosity of pores in the porous media, and n_t is the number of vascular tubes per unit area (tubes/m^2). Assuming the fractional free cross section of the vascular tubes to be equal to the summation of the gas and free water porosities, one can estimate $n_t = (S_g + S_{wf})\phi/(\pi R_t^2)$. Therefore, the bundle of tubes model was re-written as (Warning et al., 2014):

$$\kappa_{wf,in} = \frac{(S_g + S_{wf})\phi R_t^2}{24\tau} \tag{2.33}$$

From available structural data for a typical spacing between cells and porosity of the mesophyll tissue (Rockwell et al., 2014; Dymek et al., 2015; Buckley, 2015), the intrinsic permeabilities of the spongy and palisade mesophyll were estimated as 1×10^{-12} m^2 and 1×10^{-16} m^2, respectively. These values are comparable with 1×10^{-13} m^2 which was used by Song et al. (2016) as an average permeability of a leaf matrix to water and gas. The vacuum condition increases the mean free path of the gas molecules, creating a relatively large Knudsen Number ($Kn \approx 1$), which requires the Klinkenberg correction on the gas permeability (Tanikawa and Shimamoto, 2009):

$$\kappa_{g,in} = \kappa_{wf,in}\left(1 + \frac{0.15\kappa_{wf,in}^{-0.37}}{P}\right) \tag{2.34}$$

The relative permeabilities to gas and water were estimated based on the respective saturation of each species in the porous structure of mesophyll tissue (Halder et al., 2007):

$$\kappa_{w,r} = \begin{cases} \left(\frac{S_{wf}-0.08}{1-0.08}\right)^3 & S_{wf} > 0.08 \\ 0 & S_{wf} \leq 0.08 \end{cases} \tag{2.35}$$

$$\kappa_{g,r} = \begin{cases} 1 - 1.1S_{wf} & S_{wf} < 1/1.1 \\ 0 & S_{wf} \geq 1/1.1 \end{cases} \tag{2.36}$$

Capillary diffusivity

From the basic definition of the capillary diffusivity (Halder et al., 2007),

$$D_{w,cap} = -\frac{\kappa_{wf,in}\kappa_{wf,r}}{\phi\eta_w}\frac{\partial P_{cap}}{\partial S_{wf}} \tag{2.37}$$

and the Kelvin's equation, which defines capillary pressure (Pa),

$$P_{cap} = -\frac{RT}{V_w}\ln(a_w) \tag{2.38}$$

one can relate the capillary diffusivity to leaf dry-basis moisture content, M (kg/kg), and water activity:

$$D_{w,cap} = \frac{\kappa_{wf,in}\kappa_{wf,r}}{\phi\eta_w}\frac{RT}{V_w a_w}\frac{\partial a_w}{\partial M}\frac{\partial M}{\partial S_{wf}} \tag{2.39}$$

where

$$M = (S_{wf} + S_{wb})\frac{\rho_w\phi}{\rho_s(1-\phi)} \tag{2.40}$$

Estimating $\partial a_w/\partial M$ from a model for water activity (Foke, 2013; Table 2.1), the capillary diffusivity was estimated to be on the order of 1×10^{-9} m^2/s. The same value was used for both spinach and lettuce leaves.

Vapor diffusivity

The diffusivity of vapor in air within the porous media is a function of porosity, gas saturation, pressure and temperature (Millington and Quirk,1961):

$$D_{g,eff} = \phi^{1.33}S_g^{3.33}\left(\frac{2.13}{P}\right)\left(\frac{T}{273.15}\right)^{1.8} \tag{2.41}$$

Heat and mass transfer coefficients

The heat transfer coefficient at the leaf surface was dynamically updated based on the gas density of the vacuum chamber. The Nusselt number (Nu_L) was estimated for a

laminar flow over a flat surface (Incropera and DeWitt, 1990), having the dimensions (L) of a leaf:

$$Nu_L = 0.664 Re_L^{1/2} Pr^{1/3} \tag{2.42}$$

$$h_t = \frac{Nu_L k_{g,chmb}}{L} \tag{2.43}$$

where Re_L is the Reynolds Number of the flow at the leaf surface and Pr is the Prandtl Number of the gas in the chamber. The resulting heat transfer coefficient, varying from 4 J/m^2·K·s to 0.4 J/m^2·K·s during stage 1, was proportional to the square root of the gas density, *i.e.* $h_t \propto \sqrt{\rho_{g,chmb}}$. The convective mass transfer coefficient at the leaf surface was dynamically calculated by the Chilton-Colburn analogy (Incropera and DeWitt, 1990):

$$h_m = \frac{h_t D_{g,eff} Le^{0.33}}{k_{v,chmb}} \tag{2.44}$$

where Le is the Lewis Number of the gas in the chamber. During stage 1, h_m changed from 0.002 m/s to 0.0008 m/s.

2.3.6 Solution procedure

The governing equations were solved using a commercial finite element package, COMSOL® Multiphysics version 5.2a (COMSOL Multiphysics, Burlington, MA). The time-step size was dynamically varied between 0.001s to 0.25s for stages 1 and 2, and between 10 ns to 0.001s for stage 3. Relative and absolute tolerances of 0.0001 were used for all computations. A mesh of 1620 triangular elements was used for the 2D axisymmetric model for which the maximum element size was 10μm within the mesophyll tissue and far from the stomatal cavity. The solutions were done with the MUMPS direct solver. Run time for the simulations ranged from a few to several hours on a Windows machine with 32 GB of RAM, and 2 GHz dual core Intel® Xeon® CPU E5-2620 processor, depending on the time-step size and pressure jump duration.

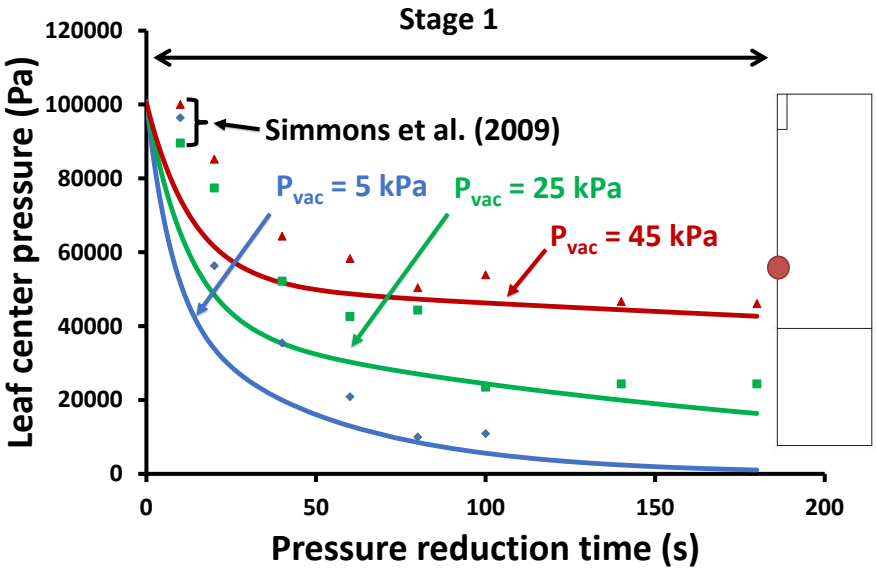

Figure 2.5: a) Computed pressure history at the midpoint of the leaf during pressure reduction stage compared with literature experimental data (Simmons et al., 2009).

2.4 Results and discussion

In this section, the predicted distributions of gas pressure, vapor pressure, evaporation rate, temperature and moisture content of the leaf, and bacterial concentration are reported and discussed. For some of the above variables, the predicted values will be compared with experimental literature data.

2.4.1 Transient pressure in the leaf: validation

During stage 1, pressure of the vacuum chamber is decreased from atmospheric level to the target pressure. Therefore, pressure within the leaf would decrease accordingly with a rate depending on the permeability of the mesophyll as well as the resistance of the stomatal opening to the gas flow. Variations of the leaf pressure during stage 1 is shown

in Fig. 2.5 for three levels of target vacuum. The model predictions were compared with the experimental data of the leaf pressure (Simmons et al., 2009) and reasonable agreement were obtained. During a vacuum cooling process, the cooling effects come from evaporation of water at the leaf surface and water within the porous structure of the leaf. When the vapor pressure within the leaf tissue goes below the equilibrium vapor pressure of water at local temperature, water starts to evaporate. Figure 2.6a shows a typical variation of the pore vapor pressure versus equilibrium vapor pressure of water at the midpoint of the leaf section. As the chamber pressure is decreased during stage 1, the vapor pressure follows closely behind the equilibrium vapor pressure. Such a trend has been reported for vacuum cooling of water (Cheng and Lin, 2007). During stage 1, pressure gradually approaches a constant level (*i.e.*, target vacuum). Therefore, pressure gradients across the leaf tissue weaken and decrease the convective transport of vapor out of the leaf section. This traps vapor within the leaf tissue and causes condensation mainly in the spongy mesophyll region (Fig. 2.6b). Further reduction in the chamber pressure leads to a rapid drop of vapor pressure (Fig. 2.6a) which follows by an increase in the evaporation rate (Fig. 2.6b). During stage 2, vapor pressure is at a constant level while equilibrium vapor pressure decreases as the produce becomes cooler (Fig. 2.6a). Therefore, evaporation rate within the leaf tissue reduces during stage 2 (Fig. 2.6b).

2.4.2 Transient temperature in the leaf: validation

Simulation results for prediction of the leaf temperature were validated against experimental data for iceberg lettuce leaves (Ozturk and Ozturk, 2009). Figure 2.7a and b show reasonable agreement between the predicted and experimental leaf temperatures during stages 1 and 2 at two different vacuum levels of 700 Pa and 1000 Pa. Several factors can contribute to the small discrepancies between simulation results and experimental data. These mainly include simplification of the computational geometry, several assumptions to simplify the model, and differences between input data (*e.g.*,

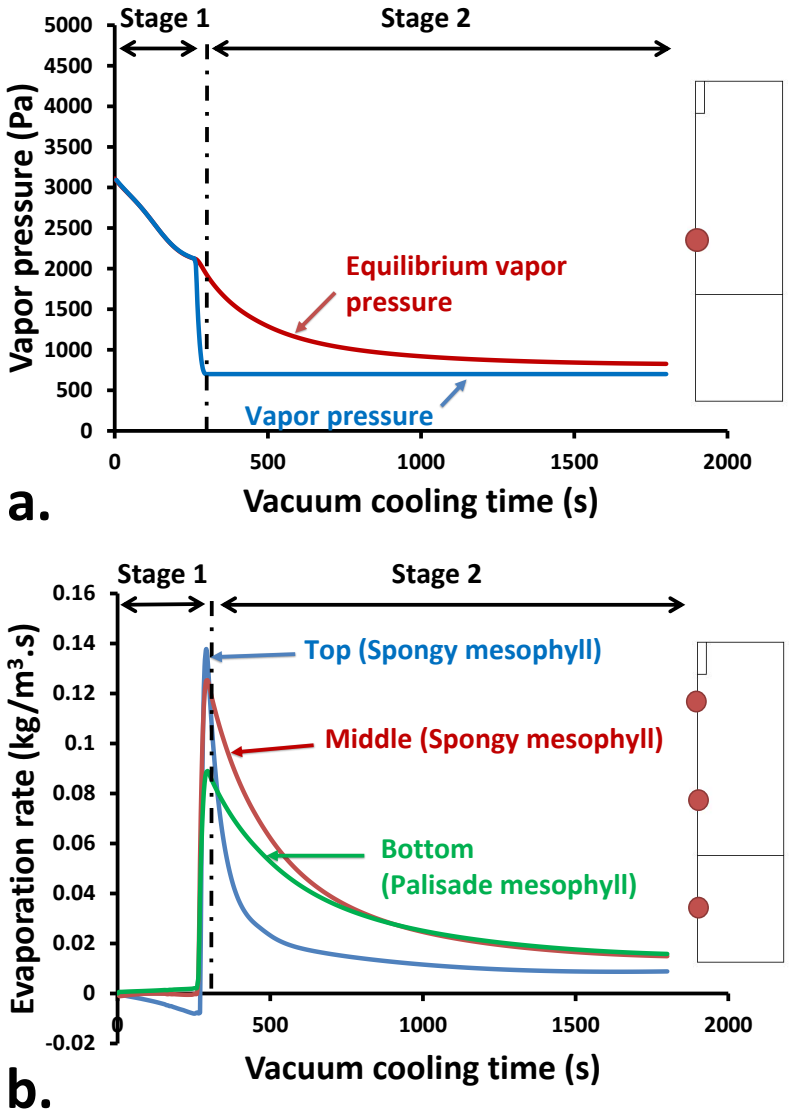

Figure 2.6: a) Computed vapor pressure compared with equilibrium vapor pressure at the midpoint of the leaf, and b) computed evaporation rate of water at three different depths in the leaf tissue.

physical, thermal and structural prosperities of the leaf) of the computations and those of the experiments. Convective heat transfer takes place at the leaf surface. Evaporative cooling also happens at the surfaces of the leaf and within its porous structure, as the vapor pressure drops below the equilibrium vapor pressure of water (Fig. 2.6a). Since the evaporative heat loss dominates the convective heat gain, the leaf cools down by the end of stage 1. As explained earlier, during stage 1, along with the reduction in the pressure gradients, the effect of evaporation gets temporarily weaker. Therefore, due to the dominance of the convective heat transfer at the leaf surface over evaporative cooling, as well as condensation within the leaf tissue (Fig. 2.6b), the rate of cooling is decreased at the end of stage 1. If this effect is strong enough, it can cause a small increase in the temperature of the produce (Cheng and Hsueh, 2007). After expulsion of the gas from the porous structure of the leaf, a sharp evaporation takes place (Fig. 2.6b) causing the temperature to fall rapidly. The temperature within the leaf section was uniform during the cooling process (Fig. 2.7c). Therefore, the trends shown in Fig. 2.7a and b are the same for the entire leaf tissue. The total cooling time depends on the amount of available water, characteristics of the leaf tissue (*e.g.*, porosity) and the target vacuum level. The higher the vacuum level, the shorter the cooling time, and the cooler the final product.

2.4.3 Transient temperature in a non-porous slab

To better understand the effect of the porous structure on the heat transfer in the leaf section during vacuum cooling, variation of temperature for a non-porous slab with the same thickness as a leaf, located in the vacuum chamber is also shown in Fig. 2.7a and b. The material properties of the slab was the same as the effective properties (Eq. 2.9-2.11) of a leaf, and the boundary conditions were the same as those at the leaf surfaces (Eq. 2.29). The temperature profile of the slab in stage 1 is quite close to that of a porous material. However, the temperature is slightly higher, which reflects the effect of some

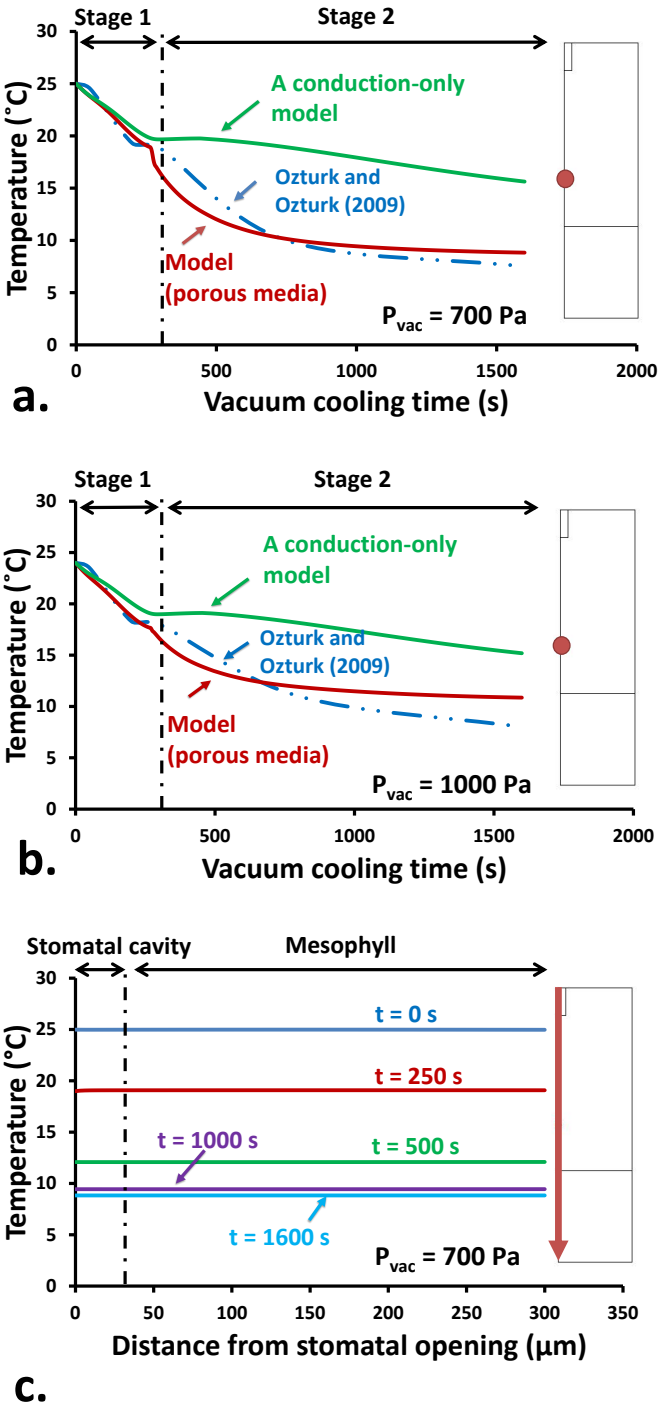

Figure 2.7: a) Computed temperature history of the midpoint of the leaf section compared with literature experimental data (Ozturk and Ozturk, 2009) at vacuum levels of 700 Pa, and b) 1000 Pa, and c) variation of temperature within the leaf depth at vacuum level of 700 Pa.

evaporative cooling within the leaf tissue. At the end of stage 1, there is an increase in the relative humidity of the gas within the vacuum chamber (Ozturk and Ozturk, 2009), which can decrease the effect of evaporative cooling at the leaf surface. Therefore, the convective heat gain dominates the evaporative heat loss at the surface of the slab and its temperature temporarily increases. After a while, during stage 2, following the expulsion of vapor from the chamber, relative humidity drops back, which results in a downward trend in the slab temperature. A comparison between the temperature profile of the slab and that of the porous material reflects the effect of volumetric cooling that can only take place in a moist porous material.

2.4.4 Transient moisture content in the leaf: validation

Variation of the average moisture content of the leaf during vacuum cooling at two vacuum levels of 700 Pa and 1000 Pa are illustrated in Fig. 2.8a. During stage 1, by generation of vapor within the porous tissue, the vapor pressure follows slightly the equilibrium curve (Fig. 2.6a) with a negligible moisture evaporation rate (Fig. 2.6b). Therefore, the amount of moisture loss becomes close to zero and moisture content takes a constant level (Fig. 2.8a). At the end of stage 1, the chamber pressure reaches the target vacuum level and moisture content drops due to the sharp evaporations (Fig. 2.6b). Similar experimental trends has been reported by He and Li (2008) for weight loss of iceberg lettuce during vacuum cooling. The predicted values for the total weight loss were in qualitative agreement with the available published data for vacuum cooling of leafy greens (Showalter and Thompson, 1956; He and Li, 2008; Fig. 2.8b).

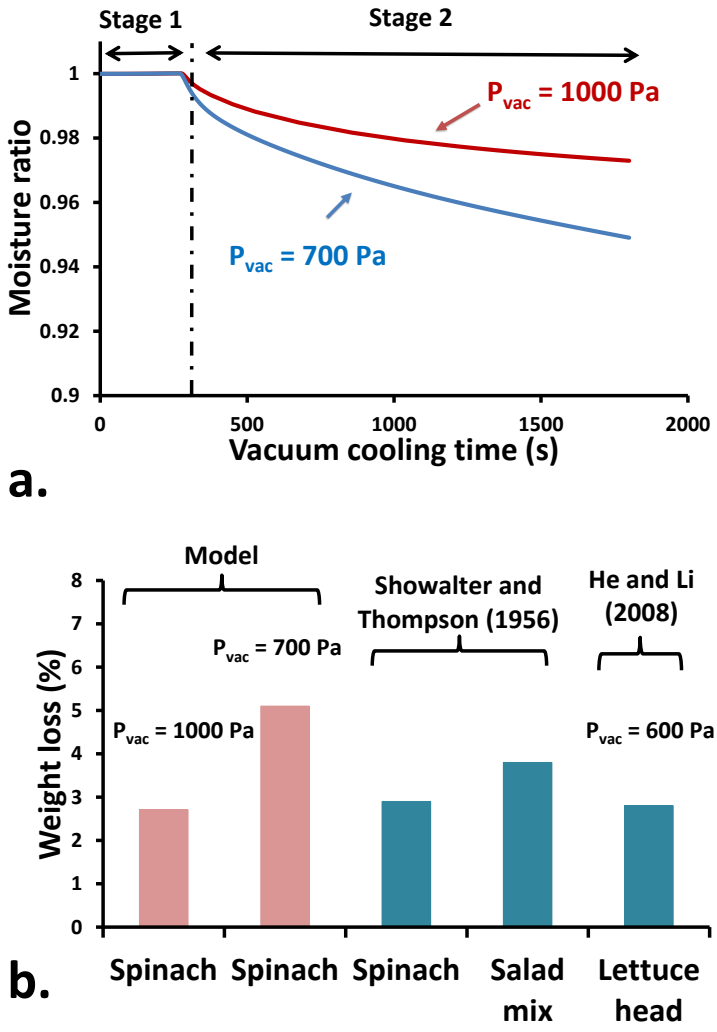

Figure 2.8: a) Computed leaf moisture content variation with time during vacuum cooling, and b) computed weight loss at the end of vacuum cooling qualitatively compared with experimental data for spinach and salad mix (Showalter and Thompson, 1956), and lettuce head (He and Li, 2008).

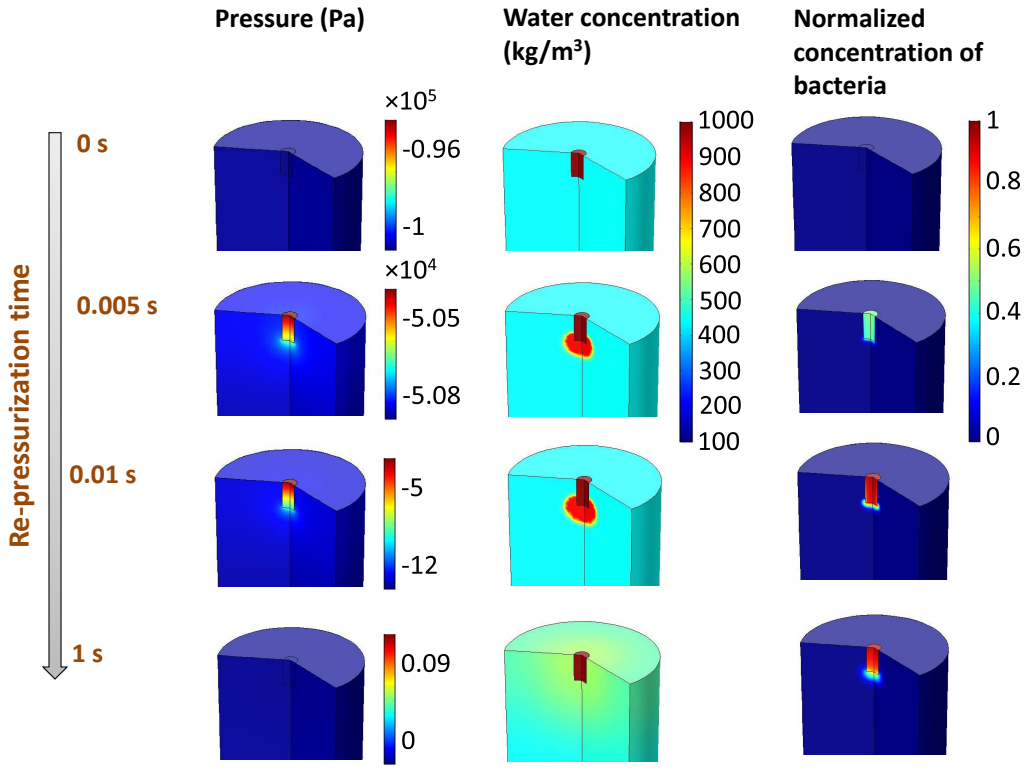

Figure 2.9: Computed spatial variation of pressure, water concentration, and bacterial normalized concentration around the stomatal cavity during re-pressurization stage of vacuum cooling process.

2.4.5 Spatial variation of pressure and water concentration during re-pressurization

A typical variation of water concentration and pressure within the leaf section during re-pressurization stage is shown in Fig. 2.9. When sufficient water is available at the stomatal opening, the pressure jump creates an inward flow into the stomatal cavity. The pressure build-up within the leaf mainly depends on the permeability of the porous zone to fluids. Higher permeabilities create faster pressure increase. As water enters the leaf section, it flows through the intercellular air spaces within the mesophyll tissue mainly driven by pressure. This is similar to the penetration of liquids into a porous

food material during a vacuum impregnation process (Tylewicz et al., 2012).

2.4.6 Bacterial infiltration

Before re-pressurization, bacteria are assumed to be dispersed within the water film at the leaf surface. The re-pressurization stage creates pressure gradients within the chamber and leaf section, pushing water and bacteria into the stomatal opening region (Fig. 2.9). The mechanism is similar to what happens during vacuum impregnation of plant tissues where the tissue is submerged in a liquid and subjected to a reduced pressure followed by a rapid re-pressurization (Simmons et al., 2009). This has been a common method for artificially infiltrating bacteria into the leaf section through available openings like stomata and wounds (Bechtold and Pelletier, 1998; Tague and Mantis, 2006; Vonasek and Nitin, 2016). Figure 2.9 shows that the short re-pressurization time made the infiltration of bacteria mainly restricted to the stomatal cavity region. For longer re-pressurization durations (data not shown), however, bacterial infiltrated much deeper into the leaf section. This is in agreement with the previous studies showing that a slow release of the vacuum would lead to better impregnation of water into the tissue (Baker and Wicker, 1996; Panarese et al., 2013). Within the stomatal cavity, water freely flows and bacterial infiltration is mainly due to convective transport. In contrast, in the porous zone, the velocities of water and bacteria decline as they face cellular obstacles and bacteria scatter around within the mesophyll tissue. Snapshots of the infiltrated GFP-tagged *E. coli* O157:H7 clusters at 12 μm beneath the surface of vacuum-cooled lettuce leaves (Li et al., 2008) showed that bacterial communities gathered within the stomatal cavities and scattered around them.

A typical variation of the total amount of bacterial infiltration into the leaf is illustrated in Fig. 2.10a. The model prediction for the total infiltrated bacteria is in qualitative agreement with the experimental data for infiltration of bacteria into spinach leaves during the vacuum cooling at 700 Pa (Shynkaryk et al., 2016). The normalized

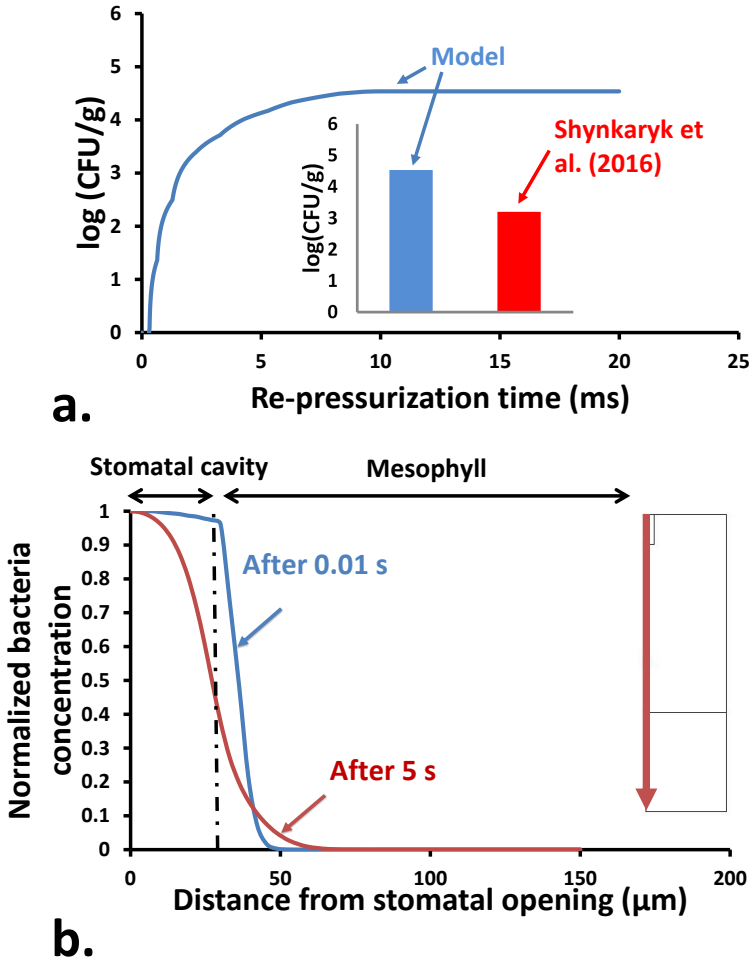

Figure 2.10: a) Amount and b) depth of infiltrated bacteria during re-pressurization stage of vacuum cooling process. The amount is qualitatively compared with literature experimental data (Shynkaryk et al., 2016).

concentration of infiltrated bacteria along the stomatal opening centerline is depicted in Fig. 2.10b. The highest concentration of bacteria is at the stomatal cavity region. As bacteria approach the porous structure of the mesophyll tissue, their concentration decreased rapidly toward the leaf depth. This is more evident right after the pressure jump from 700 Pa to atmospheric pressure. When the pressure reached the atmospheric level, bacteria spread out within the tissue due to the remaining pressure gradients and

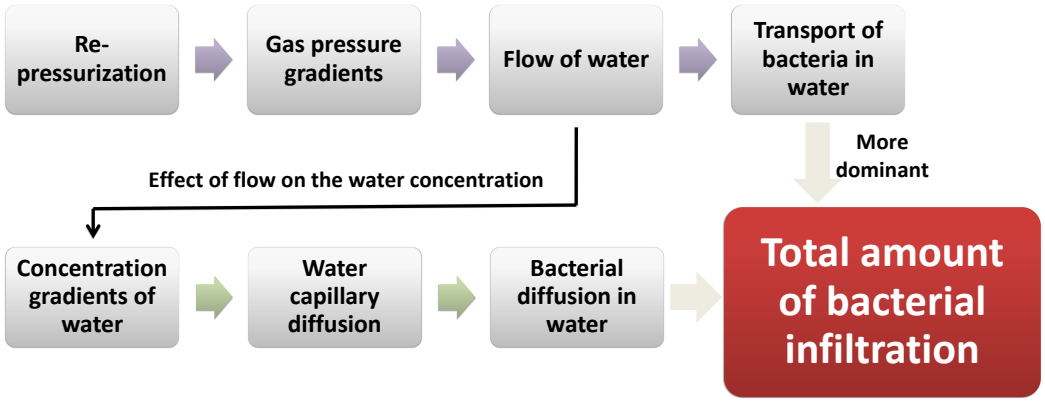

Figure 2.11: Mechanisms of bacterial infiltration during re-pressurization stage

diffusion. Available microscopy imaging data (Warmbrodt and VanDer Woude, 1990; Dymek et al., 2015) for cross section of the leafy greens show that there are relatively large air spaces within the mesophyll tissue with respect to the bacterial size. Within the spongy mesophyll, one can expect presence of air pockets with two (or higher) orders of magnitude larger than bacteria. Presence of these routes facilitate the passive transport of bacteria by water flood into the porous structure of the leaf.

The results of the present study showed that during pressure jump, the convective transport of bacteria by water was highly dominant in both the stomatal cavity (for ~100%) and mesophyll (for ~90%) regions. A summary of the mechanisms of water and bacterial infiltration during re-pressurization is shown in Fig. 2.11.

2.5 Sensitivity analysis

In order to determine the overall effects of some of the model parameters on the amount of water and bacterial infiltration into the leaf, sensitivity analyses were performed (Fig. 2.12 and 2.13). These parameters include 1) transport properties, *i.e.*, capillary diffusivity of water, diffusivity of bacteria, 2) leaf characteristics, *i.e.*, mesophyll per-

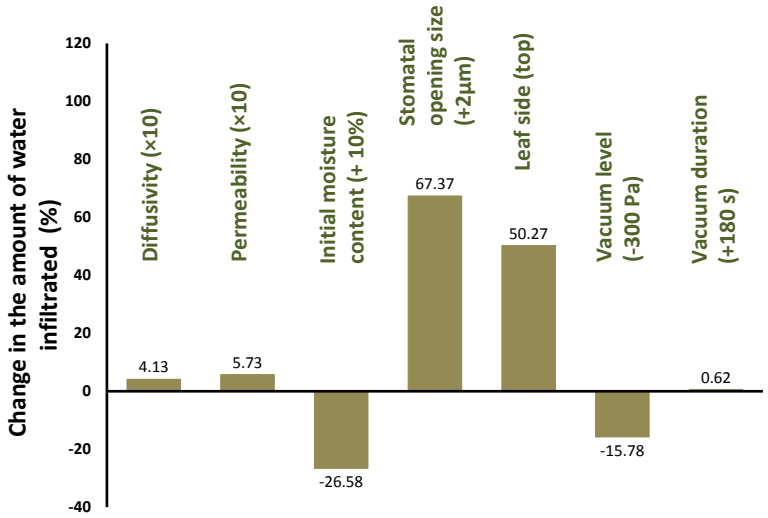

Figure 2.12: Sensitivity of the amount of water infiltration during re-pressurization stage to various process and product parameters.

meability, initial moisture content, stomatal opening size, and leaf side, and 3) process parameters, *i.e.* vacuum level, vacuum duration, and re-pressurization duration.

2.5.1 Transport properties

Capillary diffusivity

During re-pressurization, water is pushed through the stomatal opening and the leaf mesophyll due to the large pressure gradients created within the leaf section. As water flows into the pores, concentration gradients cause water to diffuse within the tissue. This observation neglects the hydrophobic nature of the exposed surfaces of the mesophyll cells for various plants (Steward, 1986). Figure 2.12 shows that one order of magnitude increase in the capillary diffusivity increases water infiltration by 4.13%. During vacuum impregnation of porous foods, the driving force for the infiltration of

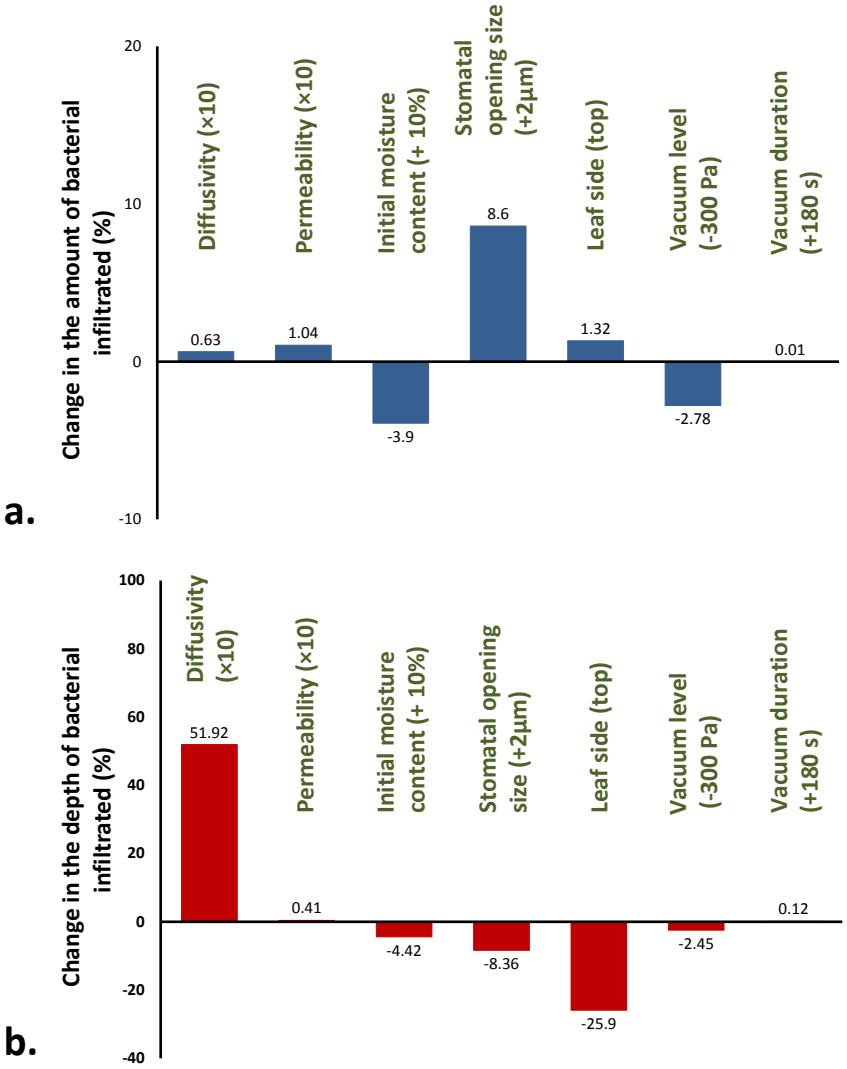

Figure 2.13: Sensitivity of the a) amount and b) depth of bacterial infiltration during re-pressurization stage to various process and product parameters.

the liquids into the porous structure is the gradients in the imposed pressure and the capillary pressure (Fito, 1994; Panarese et al., 2013). The higher the capillary pressure gradient (*i.e.*, capillary diffusivity), the more water can penetrate the pores.

Diffusivity of bacteria

Diffusion coefficient of bactreia in water can be different among various species. In general, motile bacteria can diffuse faster than non motile ones by about three orders of magnitude (Kim, 1996). Even so, bacterial diffusivity did not play a significant role on the amount of bacterial infiltration into the leaf during the re-pressurization stage. During pressure jump from 700 Pa to 1 atm, the contribution of diffusive transport within the porous structure of the leaf was less than 10%. This is due to the dominant effects of the pressure-driven convective transport of bacteria after vacuum release. One order of magnitude change in the bacterial diffusivity led to 0.63% change in the total amount of infiltrated bacteria (Fig. 2.13a). However, the depth of the infiltration was significantly affected (Fig. 2.13b). This is consistent with previous findings showing bacteria with higher diffusive (motile) capabilities spread more within a porous media (Licata et al., 2016). Note that the above observations ignore the effect of active plant-microbe interactions (for example, chemotaxis toward nutrients and biofilm formation) on the bacterial random walks and diffusivity. For later times after re-pressurization when bacteria sense the nutrients available within the leaf tissue, they may do chemotaxis toward the nutrients and actively attach to the plant cells and form colonies, which can cease their random walks. These active interactions are of longer time-scales than the re-pressurization time during vacuum cooling, and therefore are not considered in the present model.

2.5.2 Leaf properties

Permeability

Within the leaf section, water can either diffuse due to capillarity effects or flow due to the pressure gradients created during the vacuum cooling process. In Darcy's law, permeability reflects the sole effect of the porous matrix property on the fluid velocity. Leaves of various types and ages have different structural properties (*e.g.*, porosity, pore size distribution) and therefore different permeability to water and gas. As shown in Fig. 2.12, 5.73% more water infiltrated into the leaf through the stomatal opening when intrinsic permeability of the mesophyll tissue increased by one order of magnitude. This further caused 1.04% more bacteria to infiltrate into the leaf (Fig. 2.13a) with 0.41% increase in their maximum depth of infiltration (Fig. 2.13b). For higher permeabilities, water can more easily flow through the gas spaces of the mesophyll tissue and therefore more bacteria are transported into the leaf by convection. Similar relation between permeability of the produce tissue and the amount of water and bacterial infiltration were obtained in hydrocooling of tomato (Warning, et al., 2016). In the present study, as the convection-dominated flow time-scale is very short due to the short re-pressurization time, the effect of permeability on water infiltration was not very significant.

Initial moisture content

If the leaf loses moisture prior to the vacuum cooling process, more water can infiltrate it during the re-pressurization stage (Fig. 2.12). Dehydration (*i.e.*, lower water saturation) creates larger water concentration gradients, driving stronger capillary diffusion within the porous tissue (Parker et al., 1987). In addition, as the relative permeability is larger for the dehydrated porous structure, the pressure-driven flow will also increase (Warning et al., 2016). Therefore, due to stronger water transport, the amount and depth of the bacterial passive infiltration into the leaf is higher for a dehydrated tissue (Fig. 2.13).

Stomatal opening (cavity) size

Size of the stomatal opening varies over a leaf surface and also for various leaf types. In addition, this size may change when the leaf undergoes pressure changes as a result of water potential gradients across plasma membranes of stomatal guard cells (Raschke, 1970; Li et al., 2008; Sibbernsen and Mott; 2010). The model results showed that a 2 μm increase in the stomatal opening effective diameter (see Table 2.1 for nominal sizes) created a 67.37% increase in the amount of water infiltration (Fig. 2.12). This favored 8.6% more bacteria to infiltrate into the leaf tissue (Fig. 2.13a). Vacuum-induced infiltrated bacteria into lettuce leaf tissue was observed to be 5.4% of the initial cell population at the leaf surface (Li et al., 2008). From data of the amount of bacterial infiltration into spinach leaves reported by Shynkaryk et al., (2016), 0.02% of the initial cell population infiltrated into the leaf tissue. This considerable difference in lettuce and spinach infiltration can be partly explained by the fact that the stomatal opening size in lettuce is generally larger than those on spinach leaves (Iwabuchi and Kurata, 2003; Li et al., 2008). Indeed, other factors like differences in stomatal density and wettability of the leaves, process conditions, etc., could have also played roles in the bacterial infiltration. In a mathematical model for vacuum impregnation of a bacterial suspension into lettuce tissue, volume of the infiltrated bacterial suspension was directly proportional to the volume of the stomatal cavity (Simmons et al., 2009). The above results suggest that the stomatal opening size can play a role in the amount of bacterial infiltration.

Leaf side

The upper surface of the leaf has only about 25% as many stomata as the lower surface (Panarese et al., 2016). In addition, at the upper leaf surface, the region adjacent to the stomatal cavity is the palisade mesophyll which has less permeability to water (cells are tightly packed). Despite these structural characteristics, the total amount of water infiltrating the stomate at upper leaf surface is 50.27% of that of stomate located at lower leaf

surface (Fig. 2.12). At the interface between palisade and spongy mesophyll (Fig. 2.1a), there is a large gradient of water concentration, driving a fast diffusion of water out of the palisade tissue. However, the low permeability of the palisade mesopyll works as a barrier for bacteria. During the re-pressurization stage, as bacteria can hardly be transported into the palisade tissue, their concentration within the stomatal cavity increases to a point that would cease their velocity due to agglomeration (See Eq. 2.16). Therefore, they could not penetrate deeply into the leaf tissue from upper stomata (Fig. 2.13b) and the total amount of bacterial infiltration for the upper and lower sides of the leaf were not significantly different (Fig. 2.13a). These predictions follow the experimental evidences showing that the effect of leaf side on the amount of bactreia infiltration into lettuce leaf was not statistically significant, although infiltration from the top side of the leaf was slightly higher (Vonasek and Nitin, 2016).

2.5.3 Process operating parameters

Vacuum level

Applying higher levels of vacuum (around 700 Pa) ensures reaching safe levels of produce temperature (about 6 °C; Ozturk and Ozturk, 2009) during the vacuum cooling process (see Fig. 2.7). Although produce quality is improved due to lower temperature, high vacuum levels may promote the risk of infiltration during the re-pressurization stage. Lowering the vacuum (*i.e.*, increasing the absolute pressure) from 700 Pa to 1000 Pa (Ozturk and Ozturk, 2009), while maintaining the same rate of pressure increase during re-pressurization, led to lower amounts of water and bacterial infiltration into the leaf tissue (Fig 2.12 and 2.13a). With the vacuum lowered (*i.e.*, at 1000 Pa), the pressure gradient driving the flow is decreased between inside the leaf and outside. In addition, the time to reach atmospheric pressure is shorter when starting from 1000 Pa. Both these factors combine to reduce the amount and depth of water and bacteria entering

the mesophyll. These reductions in the amount and depth of infiltration at a lowered vacuum were indeed the experimental observation in infiltration of bacterial suspension into lettuce leaves during a vacuum impregnation process (Simmons et al., 2009; Simmons et al., 2014), thus validating the predictions.

Vacuum duration

As shown in Fig. 2.12, 10% increase in the vacuum duration, increased the amount of water infiltration to the leaf tissue by only 0.62%. This slight increase in the amount of water infiltration is because of having a more dehydrated product after longer vacuum duration. During re-pressurization, the larger water concentration gradients create more water capillary diffusion into the tissue. This would also slightly increase the amount and depth of bacterial infiltration (Fig. 2.13). The effect of vacuum duration might be more significant than what is predicted here. In reality, during stages 1 and 2, as the water film at the leaf surface evaporates, bacteria may be transported toward the leaf surface due to the evaporation-driven internal flows within the water film (Deegan et al., 1997), which is not included in the present model. Therefore, longer vacuum duration (*i.e.*, more evaporation of water film at the leaf surface) would accumulate bacteria closer to the leaf surface, and cause more infiltration into the leaf tissue during re-pressurization at stage 3. This is in agreement with the experimental observation of Vonasek and Nitin (2016) showing a low moisture condition at the leaf surface, created from air drying of water film a the leaf surface, led to more bacteria associate around stomatal openings.

Re-pressurization duration

Re-pressurization duration can play a role in the amount of water infiltration into the leaf. At the start of stage 3, when vacuum is broken, pressure inside the chamber in-

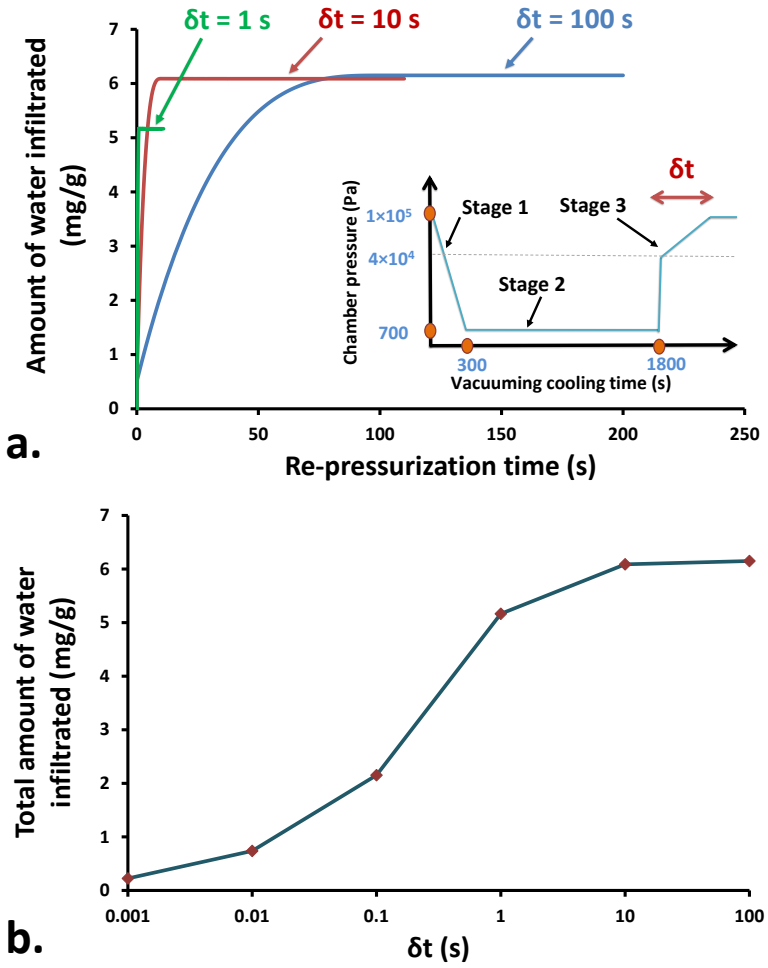

Figure 2.14: a) More water is infiltrated with longer re-pressurization time, until b) it becomes a constant value with no further increase.

creases very rapidly to a near atmospheric pressure level, typically followed by a more gradual increase to the atmospheric pressure (Cheng and Hsueh, 2007). If sufficient water is available at the leaf surface due to water spray on the leaves during vacuum cooling (Li et al., 2008; Vonasek and Nitin, 2016), extended re-pressurization duration can promote water infiltration into the leaf (Fig. 2.14a). Therefore, if the spray water is polluted by bacteria, the chance of infiltration would increase for longer re-pressurization durations. For very short re-pressurization durations, the pressure reaches the atmospheric level rapidly and the huge pressure gradients across the leaf section lead to a

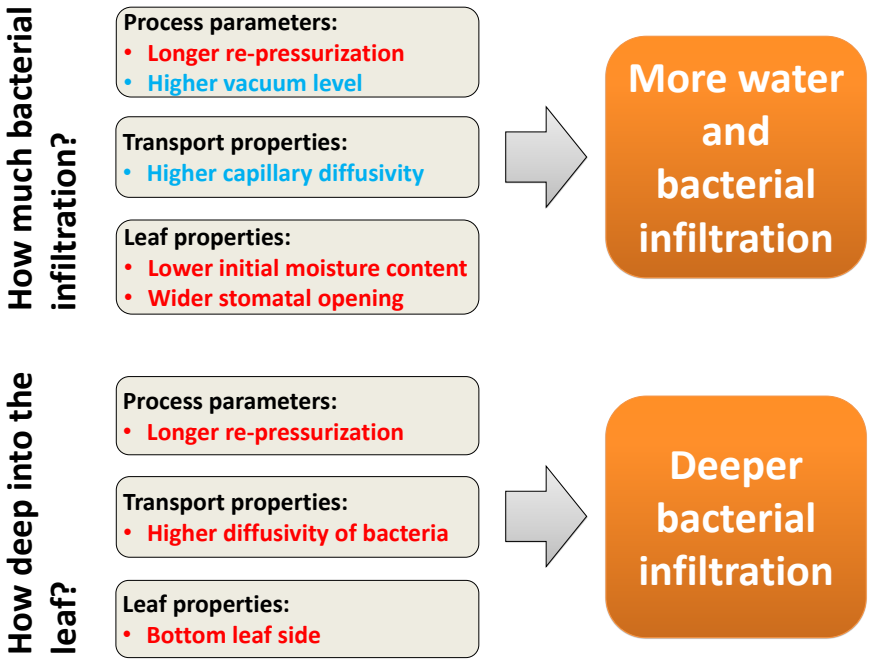

Figure 2.15: Factors affecting bacterial infiltration. Red and blue colors indicate the primary and secondary factors, respectively.

rapid water infiltration which is small in amount. The flow maintains until the gradients vanish with a rate depending on the permeability of the porous structure to water. For extended durations of re-pressurization, the pressure gradients are smaller but they last longer, infiltrating more water into the leaf (Baker and Wicker, 1996). However, such an increase in water infiltration as a function of re-pressurization duration is suppressed at some point and reaches a plateau as is shown in Fig. 2.14b. These predictions are in agreement with experimental evidences of vacuum impregnations of porous foods indicating a reduction in weight gain for faster re-pressurizations and reaching a constant weight gain level at longer re-pressurization durations (Paes et al., 2007). In reality, several plants respond to flooding of their intercellular air spaces with water by rapid (partly or complete) closure of stomata in a few minutes (Sibbernsen and Mott, 2010). Therefore, in long re-pressurization durations, they may limit or suppress water inflow through this defense mechanism.

2.5.4 Summary of factors affecting infiltration

Figure 2.15 summarizes the main conclusions from the sensitivity analysis. Re-pressurization duration, initial moisture content of the leaf and size of stomatal opening are the primary factors affecting water and bacterial infiltration into the leaf. The vacuum level and capillary diffusivity of water are the secondary factors. The depth of infiltration was primarily affected by re-pressurization duration, bacterial diffusivity, and leaf side. For extended re-pressurization duration, the pressure gradients last longer, causing more and deeper water infiltration. A low initial moisture content of the leaf leads to a stronger capillary diffusion of water within the leaf and creates stronger convective transport of water and bacteria by increasing the relative permeability. A wider stomatal opening significantly favored more water and bacterial infiltration. Bacteria having higher diffusivity (motility) were able to reach deeper locations in the leaf. Infiltration was deeper when occurred from the bottom side of leaf as the permeability to water is higher in the spongy mesophyll region.

2.6 Conclusions

The pressure-driven infiltration of bacteria into leafy greens through stomatal openings during the re-pressurization stage of the vacuum cooling process was studied using a mechanistic multiphase transport model considering the leaf as a porous medium. The model results for predictions of leaf tempearature, weight loss, and the amount of bacterial infiltration were validated against available experimental data with reasonable agreements. It was shown that when the vacuum is broken, pressure gradients occur across the leaf thickness, driving water on the leaf surface into the leaf section. Therefore, if the water on the leaf surface contains bacteria, they can be passively transported into the leaf tissue. The flow of water into the porous structure of the leaf also creates large concentration gradients of water, favoring diffusive transport of bacteria within

the mesophyll tissue. However, the role of convective transport were much more dominant in bacterial transport. Stomatal opening size, initial moisture content of the leaf, and prolongation of the re-pressurization time were among the primary factors affecting the amount of water and bacterial infiltration. Capillary diffusivity of water in the leaf and vacuum level were shown to play a secondary role on the infiltrations. The depth of the bacterial infiltration was significantly increased for higher bacterial diffusivity (motility), bottom versus top side of the leaf, and extended re-pressurization duration.

Acknowledgments

This work was supported by Grant 2014-70003-22357 from the USDA National Institute of Food and Agriculture.

BIBLIOGRAPHY

[1] Baker, R.A., Wicker, L. (1996). Current and potential applications of enzyme infusion in the food industry. Trends in Food Science and Technology 7, 279-284.

[2] Bear, J.(1972).Dynamics of Fluids in Porous Media. Dover Publications Inc.,New York.

[3] Bechtold N., Pelletier G. (1998). In planta Agrobacterium-mediated transformation of adult Arabidopsis thaliana plants by vacuum infiltration. Methods in Molecular Biology 82, 259-266.

[4] Buckley, Th. (2015). The contribution of apoplastic, symplastic and gas phase pathways for water transport outside the bundle sheath in leaves. Plant, Cell and Environment 38, 7-22.

[5] CDC. (2018). Centers for Disease Control and Prevention. E. coli O157:H7 Infections Linked to Romaine Lettuce. Retrieved from: https://www.cdc.gov/ecoli/2018/o157h7-04-18/map.html

[6] Cheng, H.P., Hsueh, C.F. (2007). Multi-stage vacuum cooling process of cabbage. Journal of Food Engineering 79(1), 37-46.

[7] Cheng, H.-P., Lin, C.-T. (2007). The morphological visualization of the water in vacuum cooling and freezing process. Journal of Food Engineering 78(2), 569-576.

[8] Deegan, R.D., Bakajin, O., Dupont, T.F., Huber, G., Nagel, S.R., Witten, Th.A. (1997). Capillary flow as the cause of ring stains from dried liquid drops. Nature 389, 827-829.

[9] DeWaal, C.S., Bhuiya, F. (2007). Outbreaks by the Numbers: Fruits and Vegetables. 1990-2005, vol. 2012.

[10] Dymek, h., Rems, L., Zorec, B., Dejmek, P., Galindo, F.G., Miklavi, D. (2015). Modeling electroporation of the non-treated and vacuum impregnated heterogeneous tissue of spinach leaves. Innovative Food Science and Emerging Technologies 29, 55-64.

[11] Evert R.F., Botha C.E.J., Mierzwa R.J. (1985). Free-space marker studies on the leaf of Zea mays L. Protoplasma 126, 6273.

[12] Fito, P. (1994). Modelling of Vacuum Osmotic Dehydration of Food. Journal of Food Engineering 22, 313-328.

[13] Foke, V. (2013). Modelling of sorption isotherms of blanched and unblanched spinach leaves. International Journal of Processing and Post Harvest Technology 4(2), 79-82.

[14] Gulati, T., Datta, A.K., (2013). Enabling computer-aided food process engineering: Property estimation equations for transport phenomena-based models.J.Food Eng. 116, 483504.

[15] Halder, A., Dhall, A., Datta, A.K. (2007). An improved, easy implementable porous media based model for deep fat frying, Part I: Model development and input parameters. Food and Bioproducts Processing 85(3), 209-219.

[16] He, S.-Y., Li, Y.-F. (2008). Experimental study and process parameters analysis on the vacuum cooling of iceberg lettuce. Energy Conversion and Management 49, 2720-2726.

[17] Incropera, F.P., DeWitt, D.P. (1990). Fundamentals of Heat and Mass Transfer,3rd edition. John Wiley and Sons, Inc., New York.

[18] Iwabuchi, K., Kurata, K. (2003). Short-term and long-term effects of low total pressure on gas exchange rates of spinach. Advances in Space Research 31(1), 241-244.

[19] Jongen, W. (2005). Improving the Safety of Fresh Fruit and Vegetables. Wood head Publishing Limited, Cambridge.

[20] Kim, Y-Ch. (1996). Diffusivity of bacteria. Korean Journal of Chemical Engineering, 13(3), 282-287.

[21] Li, H., Tajkarimi, M., Osburn, B. (2008). Impact of vacuum cooling on Escherichia coli O157:H7 infiltration into lettuce tissue. Applied and Environmental Microbiology 74(10), 3138-3142.

[22] Licata, N., Mohari, B., Fuqua, C., Setayeshgar, S. (2016). Diffusion of Bacterial Cells in Porous Media. Biophysical Journal 110, 247-257.

[23] Maurel, C. (1997). Aquaporins and water permeability of plant membranes. Annual Review of Plant Physiology and Plant Molecular Biology, 48(1), 399-429.

[24] McCabe, W.L., Smith, J.C., Harriott, P. (1956). Unit Operations of Chemical Engineering, vol. 5. McGraw-Hill, New York.

[25] Millington, R., Quirk, J. (1961). Permeability of porous solids. Transactions of the Faraday Society 57, 1200-1207.

[26] Murray, F.W. (1967). On the computation of saturation vapor pressure. Journal of Applied Meteorology 6, 203-204.

[27] Nobel, P.S. (2005). Physicochemical and Environmental Plant Physiology. 3rd Ed. Elsevier academic press, USA.

[28] Olaimat, A.N., Holley, R.A. (2012). Factors influencing the microbial safety of fresh produce: A review. Food Microbiology 32(1), 1-19.

[29] Ozturk, H.M., Ozturk, H.K. (2009). Effect of pressure on the vacuum cooling of iceberg lettuce. International Journal of Refrigeration 32, 402-410.

[30] Paes, S.S., Stringari, G.B., Laurindo, J.B. (2007). Effect of vacuum and relaxation periods and solution concentration on the osmotic dehydration of apples. International Journal of Food Science and Technology 42, 441-447.

[31] Panarese, V., Dejmek, P., Rocculi, P., Galindo, F.G. (2013). Microscopic studies providing insight into the mechanisms of mass transfer in vacuum impregnation. Innovative Food Science and Emerging Technologies 18, 169-176.

[32] Panarese, V., Herremans, E., Cantre, D., Demir, E., Vicent, A., Galindo, F.G., Nicolai, B., Verboven, P. (2016). X-ray microtomography provides new insights into vacuum impregnation of spinach leaves. Journal of Food Engineering 188, 50-57.

[33] Parker, J.C., Lenhard, R.J., Kuppusamy, T. (1987). Parametric Model for Constitutive Properties Governing Multiphase Flow in Porous Media. Water Resources Research 23(4), 618-624.

[34] Pearce, R.S., Beckett, A. (1985). Water droplets in intercellular spaces of barley leaves examined by low-temperature scanning electron microscopy. Planta 166, 335-340.

[35] Pyatkovskyy, T., Shynkaryk, M., Yousef, A., Sastry, S.H. (2017). Fresh produce sanitization by combination of gaseous ozone and liquid sanitizer. Journal of Food Engineering 210, 19-26.

[36] Rahman, M.Sh. (2005). Mass-Volume-Area-Related Properties of Foods. In, Rao, M.A., Rizvi, S.S.H., Datta, A.K. (Eds). Engineering Properties of Foods. 3rd Ed. CRC Press, Boca Raton, FL.

[37] Rahman, M.Sh. (2010). Food Properties Handbook. CRC Press, Boca Raton, FL.

[38] Raschke, K. (1970). Stomatal Responses to Pressure Changes and Interruptions in the Water Supply of Detached Leaves of Zea mays L. Plant Physiology 45, 415-423.

[39] Santakumari, M., Berkowitz, G.A. (1989). Protoplast Volume:Water Potential Relationship and Bound Water Fraction in Spinach Leaves. Plant Physiology 91, 13-18.

[40] Schonherr, J., Bukovac, M. (1972). Penetration of stomata by liquids: Dependence of surface tension, wettability, and stomatal morphology. Plant Physiology 49, 813-819.

[41] Shirai, H., Datta, A.K., Oshita, S. (2017). Penetration of aerobic bacteria into meat: A mechanistic understanding. Journal of Food Engineering 196, 193-207.

[42] Showalter, R.K., Thompson, B.D. (1956). Vacuum Cooling of Florida Vegetables. Florida State Horticultural Society, 132-135.

[43] Shynkaryk, M., Pyatkovskyy, T., Mohamed, H., Yousef, A., Sastry, S. (2015). The physics of fresh produce safety: the role of diffusion and tissue reaction in sanitization of leafy green vegetables with liquid and gaseous sanitizers. Journal of Food Protection 78 (12), 2108-2116.

[44] Sibbernsen E., Mott, K.A. (2010). Stomatal responses to flooding of the intercellular air spaces suggest a vapor-phase signal between the mesophyll and the guard cells. Plant Physiology 153, 1435-1442.

[45] Simmons, Ch.W., VanderGheynst, J.S., Nitin, N. (2014). Attachment of Agrobacterium tumefaciens to Leaf Tissue in Response to Infiltration Conditions. American Institute of Chemical Engineers, 1137-1144.

[46] Simmons, Ch.W., VanderGheynst, J.S., Upadhyaya, Sh.K. (2009). A Model of Agrobacterium tumefaciens Vacuum Infiltration Into Harvested Leaf Tissue and Subsequent In Planta Transgene Transient Expression. Biotechnology and Bioengineering 102(3), 965-970.

[47] Song, X-Y., Liu, B-L., Jaganathan, G.K. (2016). Mathematical simulation on the surface temperature variation of fresh-cut leafy vegetable during vacuum cooling. International Journal of Refrigeration 65, 228-237.

[48] Steward, F.C. (1986). Plant Physiology 9: A Treatise: Water and Solutes in Plants. Academic Press Inc., Orlando, FL.

[49] Tague B., Mantis, J. (2006). In planta Agrobacterium-mediated transformation by vacuum infiltration. Methods in Molecular Biology 323, 215-223.

[50] Tanikawa, W., Shimamoto, T., (2009). Comparison of Klinkenberg-corrected gas permeability and water permeability in sedimentary rocks.International Journal of Rock Mechanics and Mining Sciences 46(2),229-238.

[51] Thompson, J. F., Mitchell, F. G., Rumsey, T. R., Kasmire, R. F., Crisosto, C. H. (1998). Commercial cooling of fruits, vegetables, and flowers. University of California, Davis, CA.

[52] Tindall, M.J., Maini, P.K., Porter, S.L., Armitage, J.P. (2008). Overview of Mathematical Approaches Used to Model Bacterial Chemotaxis II: Bacterial Populations. Bulletin of Mathematical Biology 70, 1570-1607.

[53] Tylewicz, U., Lundin, P., Cocola, L., Dymek, K., Rocculi, P., Svanberg, S., Dymek, P., Galindo, F.G. (2012). Gas in scattering media absorption spectroscopy (GASMAS) detected persistent vacuum in apple tissue after vacuum impregnation. Food Biophysics 7, 28-34.

[54] USDA, A. (2016). USDA National Nutrient Database for Standard Reference, Release 28. https://ndb.nal.usda.gov/ndb/foods/show/3167.

[55] Vonasek, E., Nitin, N. (2016). Influence of vacuum cooling on Escherichia coli O157:H7 infiltration in fresh leafy greens via a multiphoton-imaging approach. Applied and Environmental Microbiology 82 (1), 106-115.

[56] Wang, J.H. 1965. Self-Diffusion Coefficients of Water. The Journal of Physical Chemistry, 4412.

[57] Warmbrodt, R.D., VanDer Woude, W.T. (1990). Leaf of Spinacia oleracea (Spinach): Ultrastructure, and Plasmodesmatal Distribution and Frequency, in Relation to Sieve-Tube Loading. American Journal of Botany, 77(10), 1361-1377.

[58] Warning, A., Datta, A.K., Bartz, J.A. (2016). Mechanistic understanding of temperature-driven water and bacterial infiltration during hydrocooling of fresh produce. Postharvest Biology and Technology 118, 159-174.

[59] Warning, A., Verboven, P., Nicolai, B., van Dalen, G., Datta, A.K. (2014). Computation of mass transport properties of apple and rice from X-ray microtomography images. Innovative Food Science and Emerging Technologies 24, 14-27.

[60] Winter, H., Robinson, D.G., Heldt, H.W. (1994). Subcellular volumes and metabolite concentrations in spinach leaves. Planta 193: 530-535.

[61] Zaritsky, A., Woldringh, C.L. (1987). Chromosome Replication Rate and Cell Shape in Escherichia coli: Lack of Coupling. Journal Of Bacteriology, 135(2), 581-587

[62] Zhang GD, Ma L, Beuchat LR, Erickson MC, Phelan VH, Doyle MP. (2009). Lack of internalization of Escherichia coli O157:H7 in lettuce (Lactuca sativa). Journal of Food Protection 72 (10), 2028-2037.

CHAPTER 3

MECHANISTIC MODELING OF LIGHT-INDUCED CHEMOTACTIC INFILTRATION OF BACTERIA INTO LEAF STOMATA

3.1 Abstract

Light is one of the factors that can play a role in bacterial infiltration into leafy greens by keeping stomata open and providing photosynthetic nutrients for microorganisms. Despite the known infiltration risks, limited mechanistic knowledge regarding this important infiltration pathway is available. In this work, by looking at one stomatal opening, we model chemotactic transport of bacteria within a leaf tissue in response to the photosynthesis occurring within plant mesophyll and guard cells. This first-time comprehensive model includes transport of carbon dioxide, oxygen, bicarbonate, sucrose/glucose, bacteria, and autoinducer-2 within the leaf tissue. Biological processes of carbon fixation in chloroplasts, and respiration in mitochondria of the plant cells, as well as motility, chemotaxis, nutrient consumption and communication in the bacterial community are considered. The model results for the amount of bacterial infiltration into the leaf tissue are validated by conducting microbiological experiments. The results showed that presence of light is enough to boost bacterial chemotaxis through the stomatal opening and toward photosynthetic nutrients within the leaf tissue. Bacterial ability to do chemotaxis was a major player in infiltration. It was shown that the plant stomatal defense in closing the stomata as a perception of microbe-associated molecular patterns is an effective way to inhibit the infiltration.

3.2 Introduction

Several human pathogenic bacteria such as *Salmonella*, and *Escherichia coli* are able to attach the microstructure at the surface of plant leaves, such as trichomes, stomata and grooves (Warning and Datta, 2017), and localize at sites that are not accessible for wash water and sanitizers. The bacteria are also able to infiltrate into available openings at the leaf surface, such as stomata, cuts and wounds to reach tens of micrometer depths below the leaf epidermis (Kroupitski et al., 2009). This infiltration presents a risk to the public health by causing serious foodborne outbreaks as consumption of raw leafy greens have been on the rise over the past decades (Olaimat and Holley, 2012).

Light is one of the driving forces that can promote infiltration of pathogenic bacteria into plant leaves. Incubation of *Salmonella enterica* on iceberg lettuce leaves in the light led to association of bacteria near open stomata and infiltration into the leaf tissue. However, a dark condition caused a scattered attachment pattern at the leaf surface and a poor stomatal infiltration (Kroupitski et al., 2009). Nutrients, such as glucose and sucrose, produced by photosynthetically active cells in the leaf tissue during light exposure are attractive for bacteria that may be initially present at the leaf surface (Golberg, Kroupitski, Belausov, Pinto and Sela, 2011). Opening of the stomata in light brings up an opportunity for bacteria to do chemotaxis toward the gradients of nutrients into the leaf interior. Many plants have evolved stomatal defense machinery to close the stomata upon perception of bacterial surface structures, known as microbe-associated molecular patterns (MAMPs) (Melotto, Panchal and Roy, 2014). However, it is not always successful and some human pathogens could penetrate the leaf interior through a process involved with chemotaxis and motility (Kroupitski et al., 2009).

The process of light-driven infiltration is complex involving plant photosynthesis and respiration, and transport of gases, nutrients and bacteria, that are all interconnected. These processes are affected by various factors including leaf properties, bacterial features and environmental conditions. A deeper understanding of such a complex

system can be obtained through development of a mechanistic model that integrate all the relevant biological processes together with the physics of transport. A mechanistic model can provide a comprehensive understanding of how various factors contribute to the overall process. Such a model, by its nature, can isolate the effect of a particular factor that is difficult to obtain through experiment alone. While models exist for individual elements of this complex such as for bacterial chemotaxis (Tindall, Maini, Porter and Armitage, 2008) and growth (Monod, 1949), and plant photosynthesis (Farquhar, von Caemmerer and Berry., 1980), they have not been combined for this complex system.

3.2.1 Objectives

The objectives of this manuscript are to: 1) develop a model for chemotactic and motile transport of bacteria through an open stoma into the leaf interior toward the concentration gradients of photosynthetic products of glucose and oxygen, 2) couple this model with a model of photosynthesis and respiration, and related multicomponent transport and generation of gases and sugar inside the leaf as a porous medium, 3) validate the models against literature and experimental data for photosynthetic products generated and the amount of bacterial infiltration into the leaf interior, and 4) identify the most important parameters and quantify their relative contributions to light-driven bacterial infiltration.

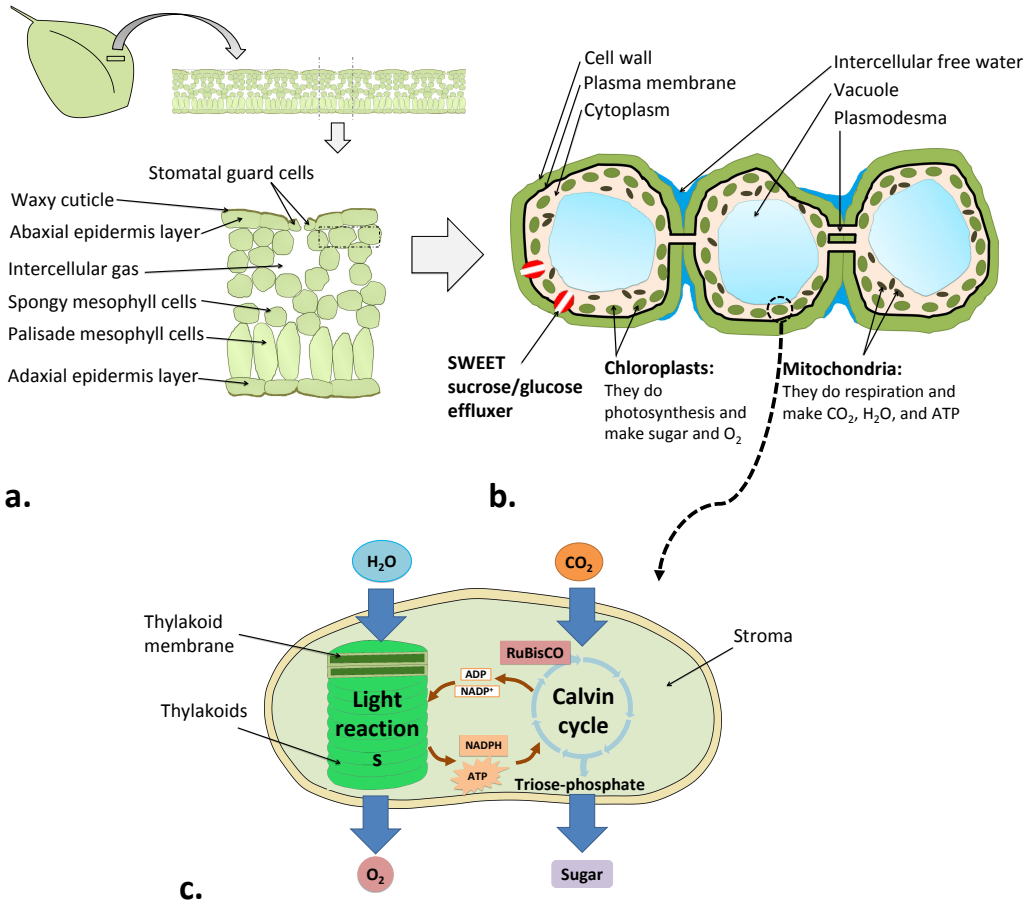

Figure 3.1: a) A leaf cross section with b) an illustration of cell organs. c) A schematic of a chloroplast with various functions that lead to photosynthesis in plant cells. The chloroplast image inspired by Campbell et al. (2008). Note that only organs and functions that are of interest in the present study are shown. Location of the SWEET sucrose/glucose effluxers is inspired from Chen (2014).

3.3 Model development

3.3.1 Biological aspects

As the model includes various biological issues related to plant and bacteria, they are briefly discussed here.

Leaf

A typical leaf section is shown in Fig. 3.1a. It includes a mesophyll tissue in the middle and two epidermis layers at top and bottom. The leaf surfaces are covered by a waxy cuticle. Stomatal openings are responsible for selective mass exchange between the leaf tissue and outside environment based on various biotic and abiotic environmental conditions (Shimazaki et al., 2007; Melotto et al., 2014; Panchal et al., 2016). Inside plant cells (Fig. 3.1b), the cytoplasm is covered by a plasma membrane and a cell wall. The majority of the cytoplasm volume is occupied by vacuoles which mainly contain water. Guard cells and mesophyll cells contain chloroplasts which are responsible for photosynthesis; production of organic nutrients. All cells within the leaf section have mitochondria which are responsible for respiration; production of energy from oxidation of organic nutrients. Water and nutrients can move from one cell to another through plasmodesmata, known as symplastic transport. In contrast, mainly in apoplastic phloem loaders such as spinach leaves, nutrients are also available in the apoplastic region (Voitsekhovskaja et al., 2000). Here, any water outside of the plasma membrane is called free water whereas intracellular water is called bound water.

During process of photosynthesis (Fig. 3.1c), light reactions occur within thylakoid membranes in which water is consumed as an electron donor and releases oxygen, hydrogen ions and electrons. The electrons are supplied to two successive electron transport chains that end up with production of ATP and NADPH to contribute in carbon fixation. Calvin cycle uses these molecules to convert carbon dioxide (CO_2) to triose phosphates (TPs) (*i.e.*, three-carbon sugar-phosphate molecule) that are building blocks for sugars production. The enzyme that catalyzes this carbon fixation step is RuBP carboxilase/oxygenase, or RuBisCO. The cycle runs three times to generate one molecule of triose-phosphate that is then provided to the plant to synthesize starch and sugars (e.g., sucrose). If the concentration of CO_2 declines, RuBisCO can bind oxygen molecules (O_2) in place of CO_2. This process is called photorespiration which does not

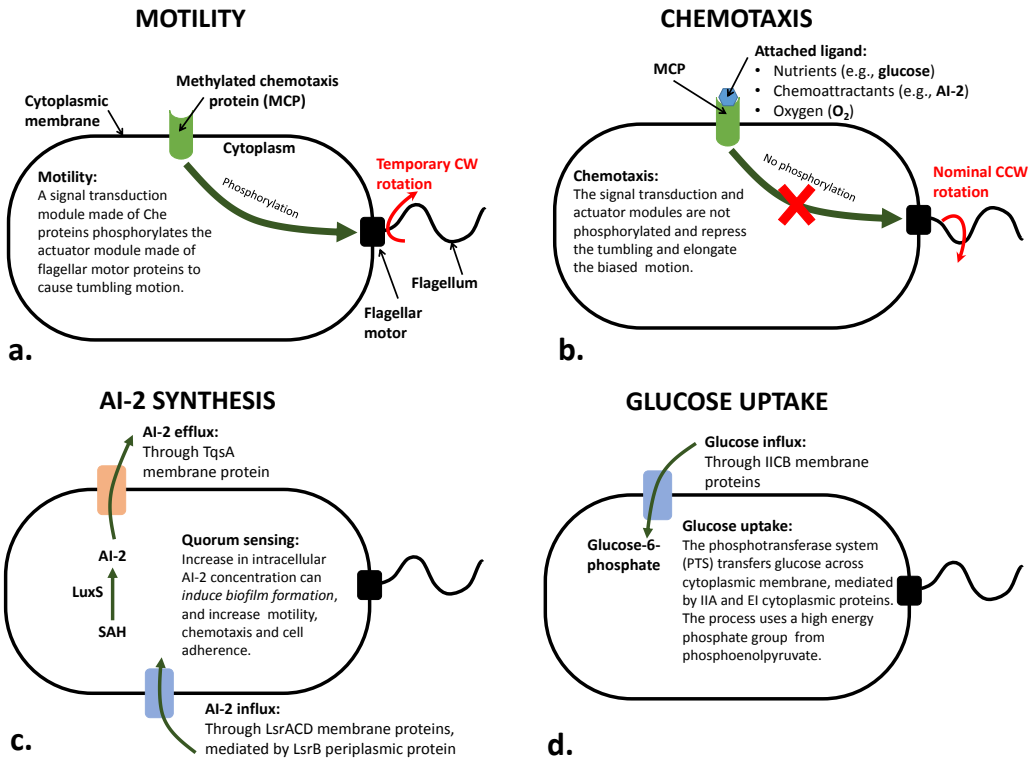

Figure 3.2: A brief illustration of the underlying pathways leading to a) bacterial cell motility, b) chemotaxis, c) AI-2 signaling, and e) glucose uptake by bacteria.

generate ATP. See Campbell et al. (2008) for more details.

Sucrose is synthesized in cytoplasm from TPs coming from chloroplast (Sharkey, 1985). In apoplastic phloem loaders, sucrose/glucose diffuse into the apoplast, mediated by SWEET transporter proteins located at the cell plasma membrane (Chen, 2014) (Fig 3.1), and then actively transported into sieve elements via SUT1 sucrose transporter (Rennie and Turgeon, 2009; Doidy et al., 2012). In the appoplast (and also within cells), invertase enzymes hydrolyse sucrose into glucose and fructose where they can be accessible by microorganisms present at the intercellular spaces of the leaf tissue (Vargas and Salerno, 2010).

Bacteria

The underlying pathways related to transport and growth of bacteria (*i.e.*, *E. coli*) are shown in Fig. 3.2. Bacterial motility (Fig. 3.2a) is referred as the random tumbling motion of a bacterium cell due to rapid changes in the direction of flagellar rotation. At the cytoplasmic membrane of bacteria, several chemoreceptors called methylated chemotaxis proteins (MCPs) exist that are sensitive to different extracellular molecules (*i.e.*, ligands). While there is no external molecule bound to the MCPs, bacterium continues the tumbling motion (McAdams et al., 2004). If an external attractant molecule binds to the MCPs (Fig. 3.2b), bacterium continues to swim toward the attractive chemicals (e.g., glucose, AI-2, O_2).

Bacteria communicate by producing and sensing signaling molecules. The intercellular signaling known as quorum sensing (QS) allows bacteria to regulate production of gene products such as enzymes, and coordinate behavioral responses at high cell densities (Laganenka et al., 2016). Among various QS systems discovered in *E. coli* (Zohar and Kolodkin-Gal, 2015), auto-inducer 2 (AI-2) signaling pathway is considered here (Fig. 3.2c). AI-2 has a key role in quorum sensing and biofilm formation in *E. coli*. AI-2 is a chemoattractant for *E coli* in a process mediated by LsrB binding protein and type Tsr of MCPs (Jani et al., 2017) . It enhances bacterial chemotaxis toward external attractants (Long et al., 2017), like glucose and oxygen.

Bacterial growth is often limited by availability of nutrients. In *E. coli* the growth limiting nutrients (Peterson et al., 2005; Bren et al., 2013) can be sources of carbon (*e.g.*, glucose), nitrogen (e.g., ammonium), phosphorus (inorganic phosphate), etc. Oxygen can also affect the growth of *E. coli* as a facultative anaerobe (McDaniel et al., 1965). Most of the microorganisms, including *E. coli*, prefer glucose as their primary carbon source (Gorke and Stulke, 2008). If sufficient glucose is present in the growth medium, synthesis of the enzymes needed for transport and metabolism of the less favorable sugars will be repressed. This phenomena is called carbon catabolite repression (CCR)

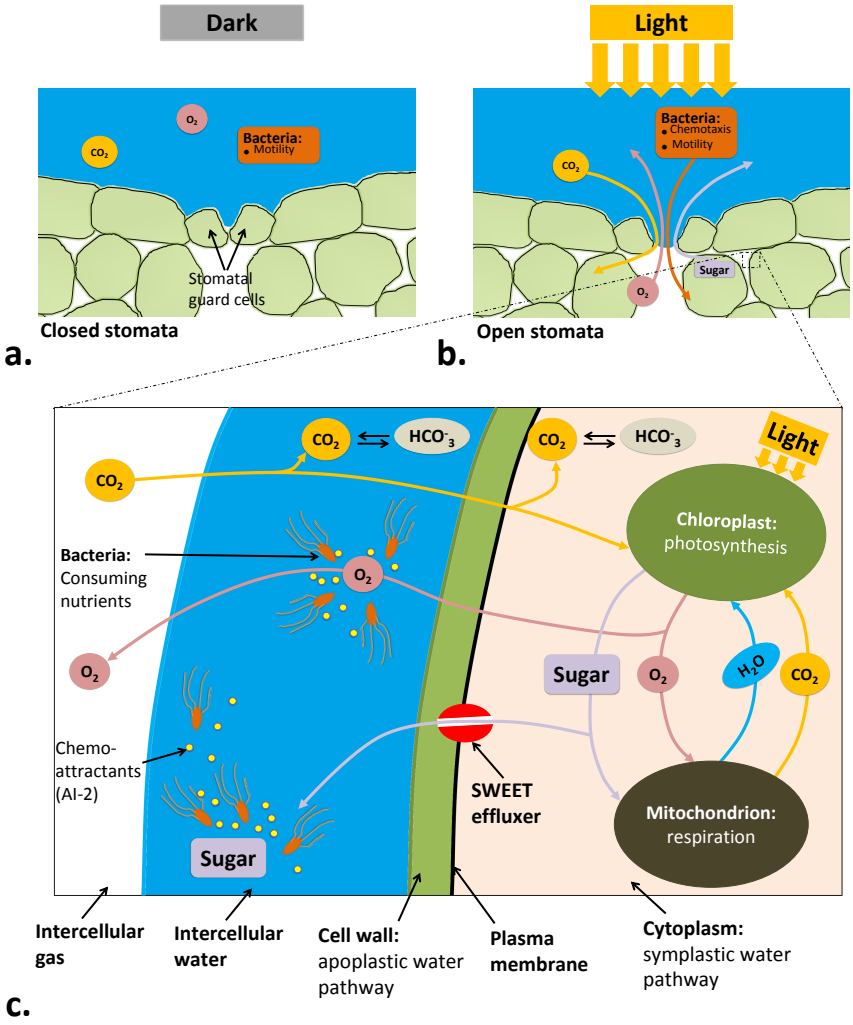

Figure 3.3: Physical schematic focusing on a stomatal opening under a) dark and b) light conditions. c) A closeup look at the underlying pathways within a leaf tissue that result in light-induced bacterial infiltration into the leaf.

(Luo et al., 2014). Glucose (and many other carbohydrates) is assimilated by bacteria through the phosphotransferase system (PTS) (Fig. 3.2d) (Gorke and Stulke, 2008).

3.3.2 Problem description and assumptions

Simplified overview of the processes

Figure 3.3 shows a schematic of the physical processes in light-driven active internalization of chemotactic bacteria into leaves through stomatal opening. This study considers the leaf surface to be covered by a thick layer of water containing bacteria. In absence of light (Fig. 3.3a), stomatal guard cells remain closed. Shedding light on the leaf (Fig. 3.3b) triggers opening of the stomatal pore (Shimazaki et al., 2007) which enhances the gas exchange into or out of the leaf tissue. Exposure to light also induces carbon fixation in the photosynthetic cells, including mesophyll cells and stomatal guard cells, leading to synsthesis of various types of sugars as well as oxygen. These nutrients attract bacteria, initially being within the water film at the leaf surface, to reach stomatal opening and infiltrate the leaf (Kroupitski et la., 2009).

A closer look at the major pathways happening within a mesophyll cell that end up to the bacterial attraction to synthesized nutrients is shown in Fig. 3.3c. Carbon dioxide (CO_2) can transport into the leaf tissue and diffuse in intercellular water, cell wall and plasma membrane to reach the chloroplast . Meanwhile, some CO_2 may be hydrated into bicarbonate (HCO_3^-). Sugar (which is assumed to be glucose/sucrose) and O_2 are produced due to photosynthesis in the chloroplast, portion of it being reused in mitochondrion to regenerate CO_2 and water. The excessive O_2 diffuses out of the cell into intercellular water (where it can attract bacteria) and gas. In apoplastic loader plants like spinach, the excessive sugar is transported to the apoplast to be loaded into the phloem (Doidy et al., 2012). Here, it is assumed that sugar efflux through SWEET transporter proteins happens at the mesophyll plasma membrane (Chen, 2014). So, sugar can diffuse into the intercellular water and be consumed by bacteria (Fig. 3.3c). Bacteria transport via motility and chemotaxis toward nutrients and chemoattractants (AI-2), starting from the layer of water outside to the intercellular space of the leaf interior.

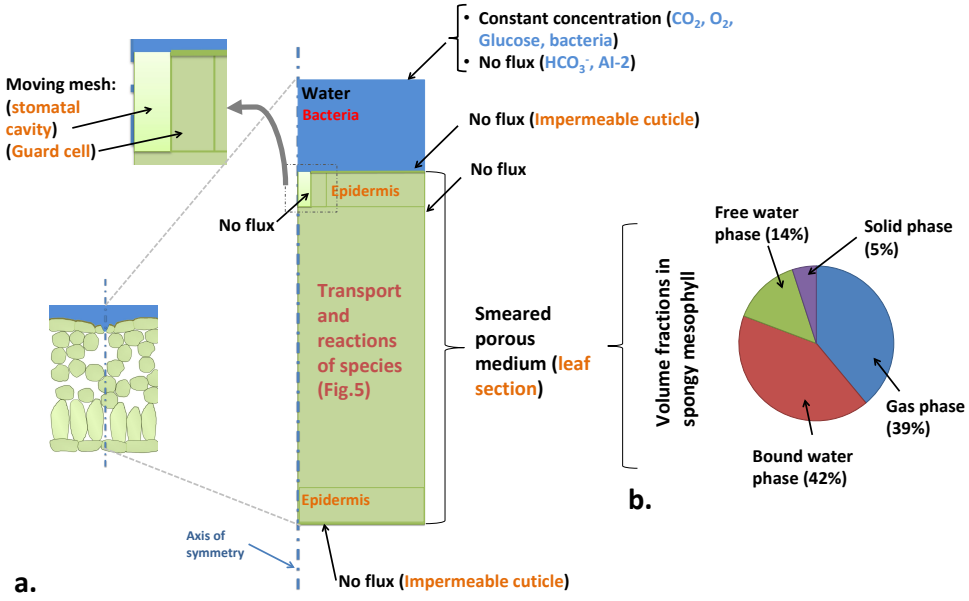

Figure 3.4: a) Model schematic showing the computational solution domain including boundary conditions and reactions. Note that this image is shown as a schematic and does not imply the exact dimensions of the different domains used in the simulations. b) Volume fractions of various phases in a computational representative elementary volume located in the spongy mesophyll region.

Computational schematic and assumptions

The computational schematic of the problem is shown in Fig. 3.4a. A 2D-axisymmetric domain around one stomatal pore, including the leaf tissue and a water film at the leaf surface, was considered as the solution domain. Transport and interactions of seven species including CO_2, O_2, HCO_3^-, symplastic glucose/sucrose, apoplastic glucose/sucrose, bacteria, and AI-2 are studied in an isothermal condition. For all species other than bacteria, a diffusion-reaction equation describes their time and spatial evaluations. For bacteria, in addition to a diffusion transport term which describes their motile (diffusion-like) motion, a convective term defines their tactic (convective-like) motion in the free water phase. The leaf tissue was assumed to be a porous media containing solid, gas and water phases (Fig. 3.4b). Due to uncertainty about the situ-

ation of gas and free water within the stomatal cavity, this region was also considered as a porous zone and each phase inside that is determined by its own saturation. In this approach, saturation of free water is a measure of wettability of the stomatal guard cells. The leaf surfaces are assumed to be impermeable to mass transfer due to the presence of the waxy cuticle layer. It was assumed that chloroplasts and mitochondria are homogeneously distributed within the leaf tissue. Within guard cell and mesophyll regions, there are photosynthesis, photorespiration, respiration, and CO_2 hydration reactions. For epidermis layers, only CO_2 hydration reaction is considered. A reaction term describes the exchange of sugar, between symplast and apoplast, through SWEET transporter proteins. Bacterial uptake of apoplastic glucose and O_2 are also modeled as a reaction term.

3.3.3 Governing Equations

Model overview

An overview of the model, including all involved species and their interconnections are shown in Fig. 3.5. Temporal and spatial evolution of each species is described by a diffusion-reaction equation. For bacteria, a convective term is also added to the transport equation to account for the chemotactic motion toward nutrients.

Basic Definitions

The solution domain includes a leaf section and a water film at the leaf surface (Fig. 3.4a). Within the leaf section, a total porosity, ϕ, is defined as the volume fraction occupied by all fluid phases:

$$\phi = \frac{1}{\delta V} \sum_i \delta V_i \tag{3.1}$$

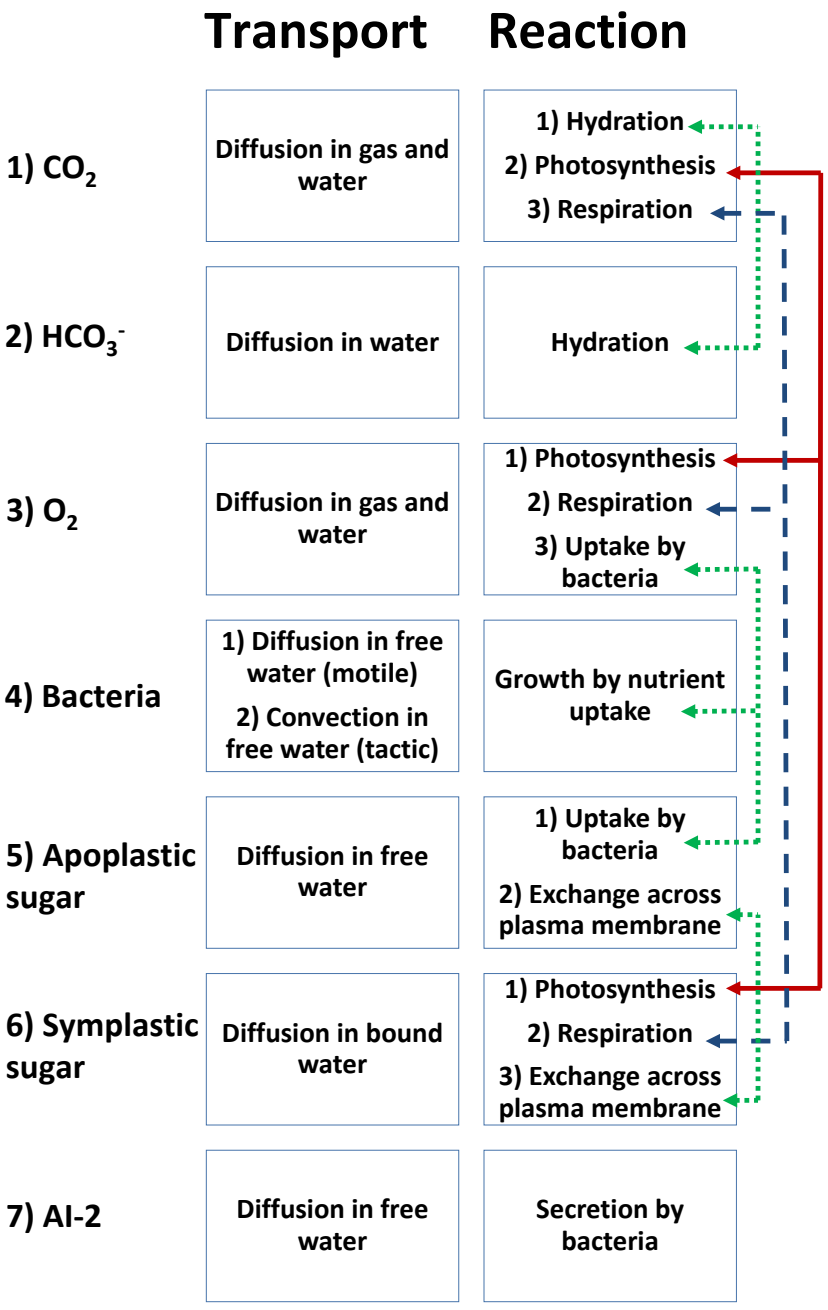

Figure 3.5: A big picture of the model showing the interconnection between all species via reaction terms.

Here $i = wf, wb, g$ represent free (intercellular) water, bound (intracellular) water, and gas phases, respectively, and δV_i is the volume occupied by the ith phase within a representative elementary volume (REV), δV. Each fluid has a saturation which is defined as a fraction of the total fluid volume within the REV:

$$S_i = \frac{\delta V_i}{\phi \, \delta V} \tag{3.2}$$

Therefore, $S_g + S_{wf} + S_{wb} = 1$. Volume fractions of jth cell organelles (*i.e.*, chloroplasts, and mitochondria) are defined by a sub-saturation coefficient as a fraction of the bound water volume:

$$\gamma_j = \frac{\delta V_j}{S_{wb}\phi \, \delta V} \tag{3.3}$$

Concentration of species (CFU/m^3 for bacteria, and mol/m^3 for others), i, within the computational domain is defined as:

$$c_i = S_g \phi c_{i,g} + S_{wf} \phi c_{i,wf} + S_{wb} \phi c_{i,wb} \tag{3.4}$$

where $c_{i,g}$, $c_{i,wf}$ and $c_{i,wb}$ are concentrations in the gas, free water and bound water phases, respectively. For some species, one or two of these concentrations can be zero. For instance, for bacteria: $c_{i,g} = 0$ and $c_{i,bw} = 0$. Solution of a transport equation for species i gives the distribution of c_i within an REV. Then Eq. 3.4 can be used to solve for the concentration values in each phase.

Transport of CO_2

As light drives the stomata to open, disolved CO_2 in the water film at the leaf surface can diffuse into the porous leaf tissue (Fig. 3.3) and be consumed in the chloroplasts during photosynthesis. Also due to photorespiration in chloroplast and dark respiration in the mitochondria some of the photosynthetic products will be oxidized, producing CO_2. In addition, CO_2 may be hydrated in the aqueous medium. Assuming CO_2 in the gas and liquid phases are in equilibrium (Ho et al., 2006), the transport equation for CO_2 in the

leaf tissue can be written as (see Appendix I for derivation):

$$\frac{\partial c_{co_2}}{\partial t} = \nabla \cdot (D_{co_2,eff} \nabla c_{co_2}) - R_{phs}\gamma_{chl}S_{wb}\phi + R_{res}\gamma_{mit}S_{wb}\phi - R_{hyd}(S_{wf} + S_{wb})\phi \tag{3.5}$$

where R_{phs} is the net photosynthesis rate, *i.e.*, CO_2 fixation rate in the chloroplasts (mol/m$^3 \cdot$ s), R_{res} is the rate of dark respiration in mitochondria (mol/m$^3 \cdot$ s). R_{hyd} is the rate of CO_2 hydration in water phase (mol/m$^3 \cdot$ s), and $D_{co_2,eff}$ is the effective diffusivity of CO_2 in the leaf (m^2/s).

Transport of bicarbonate

Bicarbonate (HCO_3^-) diffuses within the water phase. It is generated from hydration of CO_2 and makes it unavailable for photosynthesis in chloroplast. Transport equation for HCO_3^- is as:

$$\frac{\partial c_{HCO_3^-}}{\partial t} = \nabla \cdot (D_{HCO_3^-,w} \nabla c_{HCO_3^-}) + R_{hyd}(S_{wf} + S_{wb})\phi \tag{3.6}$$

where R_{hyd} is the rate of hydration of CO_2 (mol/m$^3 \cdot$ s).

Transport of O_2

Oxygen is absorbed by the water phase from intercellular gas, and within cells it is consumed during respiration in mitochondria and generated during photosynthesis. Bacteria can consume oxygen as a nutrient. The transport of O_2 in th porous media takes place in both gas and water phases (see Appendix I for derivation):

$$\frac{\partial c_{o_2}}{\partial t} = \nabla \cdot (D_{o_2,eff} \nabla c_{o_2}) + R_{phs}\gamma_{chl}S_{wb}\phi - R_{res}\gamma_{mit}S_{wb}\phi - R_{o_2,bac}S_{wf}\phi \tag{3.7}$$

where $D_{o_2,eff}$ is the effective diffusivity of O_2 in the leaf (m^2/s). $R_{o_2,bac}$ is the rate of uptake of O_2 by bacteria (mol/m$^3 \cdot$ s).

Transport of symplastic sugar

Light exposure triggers sugar synthesis in the plant cells consisting chloroplasts. Glucose/sucrose transports through plasmodesmata and membrane proteins (*i.e.*, SWEET transporters; Chen et al., 2012; Doidy et al., 2012) to be available in the apoplast. Transport of symplastic sugar is modeled as:

$$\frac{\partial c_{s,sug}}{\partial t} = \nabla \cdot (D_{sug,w} \nabla c_{s,sug}) + \alpha R_{phs} \gamma_{chl} S_{wb} \phi - R_{res} \gamma_{mit} S_{wb} \phi - R_{SWEET} S_{wb} \phi \tag{3.8}$$

where subscript s, sug denotes symplastic glucose or sucrose, R_{SWEET} is the rate of sugar transport across plasma membrane through SWEET transporters (mol/m$^3 \cdot$ s). To generate one molecule of glucose and sucrose, 6 and 12 molecules of CO_2 are consumed, respectively, therefore *i.e.*, $\alpha_{gluc} = \frac{1}{6}$ and $\alpha_{suc} = \frac{1}{12}$.

Transport of apoplastic sugar

Once the synthesized sugar reaches apoplast, it is available to the bacteria that have infiltrated the leaf tissue. Transport of apoplastic glucose/sucrose is modeled as:

$$\frac{\partial c_{a,sug}}{\partial t} = \nabla \cdot (D_{Asug,w} \nabla c_{a,sug}) + R_{SWEET} S_{wf} \phi - R_{sug,bac} S_{wf} \phi \tag{3.9}$$

where, subscript a, sug denotes apoplastic glucose or sucrose, $R_{sug,bac}$ is the rate of apoplastic sugar uptake by bacteria (mol/m^3.s).

Transport of AI-2

AI-2 is a chemoattractant molecule which is secreted by *E. coli* and enhances chemotaxis toward exogenous nutrients like glucose (Fig. 3.2; Lee and Lee, 2010). The transport of AI-2 in the leaf tissue is given by:

$$\frac{\partial c_{AI2}}{\partial t} = \nabla \cdot (D_{AI2,w} \nabla c_{AI2}) + R_{AI2} S_{wf} \phi \tag{3.10}$$

where, R_{AI2} is net rate of AI-2 production (mol/m$^3 \cdot$ s).

Transport of bacteria

The continuum Keller-Segel model (Tindall et al., 2008) is used to describe the distribution of bacteria. Within the leaf, bacteria can only transport in the free water layer at the surface of the mesophyll cells (Fig. 3.3c). The mechanisms of bacterial transport includes a random diffusion-like motion (motility) as well as chemotactic transport within free water film. The mass balance for bacteria is as:

$$\frac{\partial c_{bac}}{\partial t} + \nabla \cdot \left(c_{bac} \sum_i \mathbf{u}_{cht,i} \right) = \nabla \cdot (\eta_{bac} \nabla c_{bac}) + R_{bac,gr} S_{wf} \phi \tag{3.11}$$

where, i represents either nutrients (*i.e.*, glucose and O_2), and chemoattractants secreted by bacteria (*i.e.*, AI-2), c_{bac} is the concentration of bacteria (cell/m^3), η_{bac} is the coefficient of random motility (*i.e.*, bacteria diffusion coefficient) (m^2/s), $R_{bac,gr}$ is the rate of bacterial growth (CFU/m$^3 \cdot$ s). The rate of bacterial death is ignored here as they are assumed to be in their exponential phase of their growth.

The chemotaxtic velocity of bacteria is in the direction of the concentration gradients of species i, including glucose, O_2 and AI-2:

$$\mathbf{u}_{cht,i} = \chi_{cht,i} \frac{\nabla c_i}{c_i} \left(1 - \frac{c_{bac,wf}}{c_{bac,wf,max}} \right) \tag{3.12}$$

At high concentrations of nutrients or chemoattractants, bacteria sense the absolute gradients (∇c_i), while at low concentrations they sense the logarithmic gradients ($\nabla \log c_i = \nabla c_i / c_i$). Following Curk et al. (2013), a threshold value of 0.01 mol/m^3 was adopted to switch between these two modes of gradient sensing. At high concentrations, bacterial swimming path becomes limited. The inhibition function in Eq. 3.12 presents a simple approach to account for the effect of bacterial concentration on their chemotactic velocity. The maximum bacterial concentration, $c_{bac,wf,max}$ was adopted to be 1×10^{18} CFU/m^3

(Ranjbaran and Datta, 2019). The bacterial chemotactic coefficient (m^2/s), χ_{cht}, is defined as (Tindall et al., 2008):

$$\chi_{cht,i} = \chi_0 \frac{K_d}{(K_d + c_i)^2} \tag{3.13}$$

where χ_0 is chemotactic sensitivity coefficient (m^2/s), and K_d is the receptor-ligand binding dissociation constant (mol/m^3). Estimations of numerical values of these parameter for *E. coli* can be found in Tindall et al. (2008), Ford and Lauffenburger (1991), and Ford, Phillips, Quinn, Lauffenburger (1991). The porous structure of the leaf can affect bacterial migration and confine their motile and tactic movements (Bhattacharjee and Datta, 2019). To include this confinement effect, the amounts of coefficient of random motility, η_{bac}, and chemotactic sensitivity coefficient, χ_0, in the porous media were assumed to be two orders of magnitudes less than that in the water layer.

Rate of hydration of CO_2

Carbonic anhydrase (CA) can catalyze the hydration of CO_2 to HCO_3^-. However, its effect on the rate of photosynthesis was shown not to be significant (Ho et al., 2016). In the absence of carbonic anhydrase, the rate of hydration of CO_2 is defined as:

$$R_{hyd} = k_1 c_{co_2,w} - k_2 \frac{c_{H^+} c_{HCO_3^-,w}}{K_{hyd}} \tag{3.14}$$

k_1, k_2 and K_{hyd} are rate constants of the reaction. The concentration of c_{H^+} in (mol/m^3) was estimated based on the values of pH within the leaf and water layer, *i.e.*, pH $= -\log_{10}\left(10^{-3} c_{H^+}\right)$.

Rate of photosynthesis

Photosynthesis is one of the most studied and best understood physiological processes (Yin and Struik, 2009). Recently, very detailed biochemical models including light reactions, proton transport, enzymatic reactions and regulatory functions have been developed (Laisk and Oja, 2006; Zhu et al., 2007; Zhu et al., 2013). However, due to high

level of complexity, these models cannot be used to model photosynthesis in leaf-level applications (Yin and Struik, 2009). Instead, the biochemical model of Farquhar et al (1980) (*i.e.*, the FvCB model) can be effective for this purpose. The art of this model is that it makes no attempt to model all processes of photosynthesis but rather focuses on a few key processes involved in C3 photosynthesis (Yin and Struik, 2009). Considering FvCB model, the net photosynthesis rate, *i.e.*, CO_2 fixation rate (mol/m^3 · s), R_{phs}, in the chloroplasts of the C3 plant cells is described as:

$$R_{phs} = \min\{A_c, A_j, A_p\} \tag{3.15}$$

$$A_c = \frac{(p_{co_2} - \Gamma^*)V_{c,max}}{p_{co_2} + K_{m,co_2}(1 + p_{o_2}/K_{m,o_2})} \tag{3.16}$$

$$A_j = \frac{(p_{co_2} - \Gamma^*)J}{4p_{co_2} + 8\Gamma^*} \tag{3.17}$$

$$A_p = \frac{3T_p^*}{1 - \Gamma^*/p_{co_2}} \tag{3.18}$$

where A_c is the RuBisCO-limited rate of CO_2 assimilation (mol/m^3 · s), A_j is the electron transport-limited rate of CO_2 assimilation (mol/m^3 · s), and A_p is TP utilization-limited (TPU-limited) rate of CO_2 assimilation (mol/m^3 · s). In Eq. 3.16, p_{co_2} and p_{o_2} are CO_2 and O_2 partial pressures (Pa) in chloroplast, $V_{c,max}$ is the maximum carboxilation capacity of RuBisCO (mol/m^3 · s), K_{m,co_2} and K_{m,o_2} are Michaelis-Menten constants of RuBisCO for CO_2 (during photosynthesis) and O_2 (during photorespiration) (Pa), and Γ^* is CO_2 compensation point without dark respiration (Pa). In Eq. 3.17, J is the volumetric rate of electron transport (mol/m^3·s) that includes the effects of light intensity and wavelength on the rate of photosynthesis. In Eq. 3.18, T_p^* is the volumetric TPU rate (mol/m^3 · s).

Rate of respiration

Based on the available values for the dark respiration at 25°C (Farquhar et al., 1980; Ho et al., 2016), the following equation was used to described temperature dependence of the dark respiration (mol/m^3 · s), R_{res}:

$$R_{res} = 1.1 \times 10^{-6}\alpha_t \exp\left(\frac{66405(T - 298)}{298RT}\right) \tag{3.19}$$

To convert the rate of respiration to a volumetric value, α_t was assumed to be the reciprocal of the leaf thickness (1/m).

Rate of sugar efflux by SWEET transporters

SWEET proteins are energy-independent transporters (Chen et al., 2012; Doidy et al., 2012; Ayre and Turgeon, 2018), and transport of glucose/sucrose across them is facilitated by molecular diffusion. The rate of sugar efflux by SWEET transporters depends on the concentration gradient across plasma membrane, population density of the transporters on the plasma membrane, and the level of the saturation of the transporter. The volumetric rate of sugar transport (mol/m^3 · s) across plasma membrane through SWEET transporters can be written as:

$$R_{SWEET} = P_{sug}\left(c_{Ssug} - c_{Asug}\right) A_{SWEET}\rho_{SWEET}\left(\frac{c_{Ssug}}{K_{SWEET} + c_{Ssug}}\right)\alpha_p \tag{3.20}$$

The permeability (m/s) of a SWEET transporter to the sugar of interest was estimated from diffusion coefficient of the sugar in water phase and the thickness of the plasma membrane (7 nm) (Nobel, 2005) as $P_{sug} = D_{sug,w}/l_{plm}$. In the above equation, A_{SWEET} is the pore surface area of the SWEET transporter (m^2), ρ_{SWEET} is the population density of SWEET transporters at the plasma membrane of the plant cells (transporter/m^2), K_{SWEET} is the half-saturation constant for the transporter (mol/m^3), and α_p is the specific surface area (m^2/m^3) of the porous structure of the leaf.

Rate of uptake of glucose and oxygen by bacteria

The rate of uptake of glucose and O_2 by bacteria can be modeled as (Tindall et al., 2008):

$$R_{i,bac} = \zeta_{gr,i} c_{bac} Y_{i/bac} f_{QS} \tag{3.21}$$

where i denotes apoplastic glucose or O_2, $\zeta_{gr,i}$ is the bacterial growth rate (1/s) defined in Eq. 3.24, $Y_{i/bac}$ is the yield coefficient of nutrients on bacteria (mol/cell), and f_{QS} is a switch function which represents the effect of quorum sensing of signaling molecules (*e.g.*, indole) during biofilm formation. It can be defined as a Hill function (Goryachev, 2011) to show state transition in bacterial biofilms. However, as the duration of the process of interest here (2 h) is much shorter than the time-scale for bacteria to reach stationary phase (Li and Young, 2013) and develop biofilms ($>>$ 2 h), one can write $f_{QS} = 1$.

Rate of synthesis of AI-2

Synthesis of AI-2 by *E. coli* increases during exponential phase of the cells' growth. However, as cells reach the stationary phase, they uptake the extracellular AI-2 (Wang et al., 2005; Xavier and Bassler, 2005). When glucose is present in the growth medium, synthesis of AI-2 in the exponential phase is boosted, while its uptake in the stationary phase is weakened (Li et al., 2006). Since in this study bacteria are always in their exponential phase, only the synthesis of AI-2 is modeled, and its uptake by bacteria is ignored:

$$R_{AI2} = k_{1,AI2} c_{bac} \tag{3.22}$$

Here, R_{AI2} is the rate of synthesis of AI-2 (mol/m^3·s) , and $k_{1,AI2}$ is AI-2 synthesis rate constant (mol/cell · s) whose value depends on the presence of glucose in the medium. The estimated values for this rate constant based on the experimental and simulation data of Xu et al. (2017), Wang et al. (2005) and Li et al. (2006) are included in Table 3.1.

Rate of bacterial growth

The rate of bacterial growth as a result of nutrients uptake is:

$$R_{bac,gr} = \zeta_{gr} c_{bac} f_{QS} \tag{3.23}$$

The bacterial growth rate constant (1/s), ζ_{gr}, is defined using Monod kinetics (Monod, 1949):

$$\zeta_{gr} = \zeta_{max,gr} \prod_i \frac{c_i}{K_{s,i} + c_i} \tag{3.24}$$

Here, i stands for glucose and O_2, $\zeta_{max,gr}$ is the maximum growth rate constant (1/s), and $K_{s,i}$ is the Monod half saturation constant (mol/m^3). Note that here $f_{QS} = 1$, as bacteria are in their exponential phase of growth.

3.3.4 Boundary and initial conditions

Table 3.1 shows all numerical values used for boundary and initial conditions in this study. Initial concentrations of CO_2 and O_2 in the solution domain were calculated based on the saturation of each phase and the Henry's law. Their concentration in the gas phase were equal to atmospheric levels. Initial concentrations of sugars were in spinach and lettuce leaves were obtained from Voitsekhovskaja et al. (2000) and Kroupitski et al. (2009), respectively. For HCO_3^-, initial concentration in the water phase was set as 0.001 mol/m^3 (assumed from Allakhverdiev et al., 1997). Bacterial concentration was initially normalized to 1 in the water film, and was set to 0 in the leaf tissue. Concentration of AI-2 was initially zero in the entire domain.

An overview of the boundary conditions is shown in Fig. 3.4a. The constant concentration boundary condition at the top boundary of the water film is defined as:

$$c_i = c_{i,\infty} \tag{3.25}$$

where i stands for CO_2, O_2, glucose/sucrose, and bacteria. Note that for CO_2 and O_2, the concentrations in the water phase can be estimated by Henry's law based on their partial pressures in the gas phase (Ho et al., 2016):

$$c_{co_2,\infty} = RTK_{H,co_2}c_{co_2,g} \tag{3.26}$$

$$c_{o_2,\infty} = RTK_{H,o_2}c_{o_2,g} \tag{3.27}$$

where K_{H,co_2} and K_{H,o_2} are the Henry's constants for CO_2 and O_2 ($mol/m^3 \cdot Pa$), respectively, R is the universal gas constant ($J/mol \cdot K$), and T is temperature (K). The no flux condition for species i applied to several boundaries in the solution domain (see Fig. 3.4a) is written as:

$$-D_{i,f}\frac{\partial c_i}{\partial n} = 0 \tag{3.28}$$

where subscript f stands for fluid phase, and n denotes the normal direction to the boundary.

3.3.5 Input parameters

Input data for the simulations are shown in Table 3.1. Details of some of the input parameters are discussed here.

Table 3.1: Input Parameters

Parameter	Symbol	Value	Units	Source
Dimensions				
Stomatal aperture	D_{stoma}	Fig. 3.12	m	Measured
Depth of leaf section	H_{leaf}	700×10^{-6}	m	Vogelmann and Evans (2002)
Depth of spongy mesophyll layer	H_{spg}	370×10^{-6}	m	Assumed
Depth of palisade mesophyll layer	H_{pls}	270×10^{-6}	m	Assumed
Depth of epidermis layer	H_{stoma}	30×10^{-6}	m	Assumed
Width of the domain	W_{leaf}	80×10^{-6}	m	Assumed
Density				
Carbon dioxide	ρ_{co_2}	Ideal gas	kg/m^3	Assumed
Oxygen	ρ_{o_2}	Ideal gas	kg/m^3	Assumed
Diffusivity				
Motile-only bacteria in water	$\eta_{bac,mot}$	1×10^{-12}	m^2/s	Wu et al. (2006)
Wild type bacteria in water	$\eta_{bac,wt}$	5×10^{-11}	m^2/s	Wu et al. (2006)
Carbon dioxide in air	$D_{co_2,g}$	1.6×10^{-5}	m^2/s	Lide (1999)

Oxygen in air	$D_{o_2,g}$	1.6×10^{-5}	m^2/s	Lide (1999)
Carbon dioxide in water	$D_{co_2,w}$	1.67×10^{-9}	m^2/s	Lide (1999)
Oxygen in water	$D_{o_2,w}$	2.01×10^{-9}	m^2/s	Lide (1999)
HCO_3^- in water	$D_{HCO_3^-,w}$	1.17×10^{-9}	m^2/s	Geers and Gros (2000)
Glucose in water	$D_{gluc,w}$	0.67×10^{-9}	m^2/s	Nobel (2005)
Sucrose in water	$D_{suc,w}$	0.52×10^{-9}	m^2/s	Nobel (2005)
AI-2 in water	$D_{AI2,w}$	1×10^{-10}	m^2/s	Assumed from Stewart (2003)
Leaf properties				
Porosity	ϕ	0.95	m^3/m^3	Ranjbaran and Datta (2019)
Specific surface area of porous zone	α_p	1×10^5	m^2/m^3	Calculated from Rahman (2005)
SWEET transporters				
Permeability, glucose	P_{gluc}	1.34×10^{-1}	m/s	Calculated
Permeability, sucrose	P_{suc}	1.04×10^{-1}	m/s	Calculated

Population density on plasma membrane	ρ_{SWEET}	1×10^{12}	$1/m^2$	Assumed from Nobel (2005)
Cross section area	A_{SWEET}	1×10^{-19}	m^2	Calculated from Carruthers (1990), and Dend and Yan (2016)
Half saturation constant	K_{SWEET}	9.1	mol/m^3	Assumed from Chen et al. (2010)
Saturations				
Spongy mesophyll, gas	$S_{g,spg}$	0.41	m^3/m^3	Ranjbaran and Datta (2019)
Spongy mesophyll, free water	$S_{fw,spg}$	0.15	m^3/m^3	Ranjbaran and Datta (2019)
Spongy mesophyll, bound water	$S_{bw,spg}$	0.44	m^3/m^3	Ranjbaran and Datta (2019)
Palisade mesophyll, gas	$S_{g,pls}$	0.20	m^3/m^3	Ranjbaran and Datta (2019)
Palisade mesophyll, free water	$S_{fw,pls}$	0.15	m^3/m^3	Ranjbaran and Datta (2019)

Palisade mesophyll, bound water	$S_{bw,pls}$	0.65	m^3/m^3	Ranjbaran and Datta (2019)
Epidermis layer, gas	$S_{g,epd}$	0.20	m^3/m^3	Assumed
Epidermis layer, free water	$S_{fw,epd}$	0.15	m^3/m^3	Assumed
Epidermis layer, bound water	$S_{bw,epd}$	0.65	m^3/m^3	Assumed
Stomatal cavity, gas	$S_{g,stm}$	0.90	m^3/m^3	Assumed
Stomatal cavity, free water	$S_{fw,stm}$	0.10	m^3/m^3	Assumed
Sub-saturation coefficients				
Chloroplast, mesophyll	$\gamma_{chl,mes}$	0.254	m^3/m^3	Winter et al., (1994)
Chloroplast, guard cell	$\gamma_{chl,grd}$	0.254	m^3/m^3	Assumed
Chloroplast, epidermis	$\gamma_{chl,epd}$	0	m^3/m^3	Assumed
Mitochondria	γ_{mit}	0.0082	m^3/m^3	Winter et al., (1994)
Gas solubility in water				
Gas solubility in water				

Henry's constant for CO_2, at 20 °C	K_{H,co_2}	0.3876×10^{-3}	$mol/m^3 \cdot Pa$	Lide (1999)
Henry's constant for O_2, at 20 °C	K_{H,o_2}	0.0137×10^{-3}	$mol/m^3 \cdot Pa$	Lide (1999)
Carbon dioxide hydration				
Reaction constant 1	k_1	0.039	$1/s$	Jolly (1985)
Reaction constant 2	k_2	23	$1/s$	Jolly (1985)
Acid dissociation constant for H_2CO_3	K_{hyd}	0.25	mol/m^3	Jolly (1985)
pH	pH	7.0, Water 6.5, Leaf		Assumed Assumed from Babic and Watada (1996)
Light absorption by chloroplasts				
Specific absorption, Blue light	$a^*_{chl,blu}$	2600	m^2/mol	Assumed from Vogelmann and Evans (2002)

Specific absorption, Green light	$a^*_{chl,grn}$	1500	m^2/mol	Assumed from Vogelmann and Evans (2002)
Specific absorption, Red light	$a^*_{chl,red}$	2000	m^2/mol	Assumed from Mitchell and Kiefer (1988) and Vogelmann and Evans (2002)
Specific absorption, white light	$a^*_{chl,wht}$	2100	m^2/mol	Assumed
Nutrient uptake by bacteria				
Yield of glucose on bacteria	$Y_{gluc/bac}$	9.4×10^{-15}	mol/cell	Assumed from Kayser et al. (2005)
Yield of oxygen on bacteria	$Y_{o_2/bac}$	2.9×10^{-14}	mol/cell	Assumed from Shiloach and Fass (2005)
AI-2 reaction				

Synthesis rate constant	$k_{1,AI2}$	1×10^{-24}, no glucose	mol/cell · s	Li et al. (2006), Xu et al. (2017) and Wang et al. (2005)
		1×10^{-23}, with glucose	mol/cell · s	
Bacterial chemotaxis				
Chemotactic sensitivity coefficient, *E. coli*	χ_0	10×10^{-9}	m^2/s	Ford et al. (1991)
Receptor-ligand dissociation constant	K_d	0.1	mol/m^3	Ford and Lauffenburger (1991)
Bacteria growth				
Maximum growth rate constant, at 25 °C	$\zeta_{max,gr}$	1.00×10^{-4}	1/s	Assumed from Kovarova et al. (1996)
Monod half saturation constant, glucose	K_{gluc}	184.8×10^{-6}	mol/m^3	Kovarova et al. (1996)
Monod half saturation constant, Oxygen	K_{o_2}	121×10^{-6}	mol/m^3	Stolper et al. (2010)

Effective diffusivities

The effective diffusivity of CO_2 and O_2 in the leaf, $D_{i,eff}$, accounts for both diffusion coefficients in the gas, $D_{i,g}$, and water, $D_{i,w}$, phases by considering the interphase equilibrium based on the Henry's law (see Appendix I for full derivation):

$$D_{i,eff} = \frac{S_g D_{i,g} + (S_{wf} + S_{wb}) RTK_{H,i} D_{i,w}}{S_g + (S_{wf} + S_{wb}) RTK_{H,i}} \tag{3.29}$$

CO_2 assimilation parameters

RuBisCO-limited: Temperature dependence of kinetics parameters of RuBisCO (in Eq. 3.16) including $V_{c,max}$, K_{m,co_2} and K_{m,o_2} can be described by Arrhenius equations (Farquhar, 1980). The activation energy for the maximum carboxilation capacity of RuBisCO, $V_{c,max}$, in spinach leaves was 64900 J/mol. Based on the data of Yamori et al. (2008) at 25°C, the maximum carboxilation capacity (mol/m^3 · s) was calculated as:

$$V_{c,max} = 49.9 \times 10^{-6} \alpha_t \exp\left(\frac{64900(T - 298)}{298RT}\right) \tag{3.30}$$

The temperature dependence of the Michaelis-Menten constants of RuBisCO (Pa), within a range of 5-40 °C, were calculated as (Yin and Struik, 2009):

$$K_{m,co_2} = 27 \exp\left(\frac{80990(T - 298)}{298RT}\right) \tag{3.31}$$

$$K_{m,o_2} = 16500 \exp\left(\frac{23720(T - 298)}{298RT}\right) \tag{3.32}$$

The CO_2 compensation point without dark respiration (Pa), Γ^*, is defined as the partial pressure of CO_2 at which no net assimilations occurs (Yin and Struik, 2009). The temperature dependence of Γ^* was reported by Medlyn et al. (2002) for spinach leaves:

$$\Gamma^* = 0.101325 \left(42.7 + 1.68(T - 298.15) + 0.0012(T - 298.15)^2\right) \tag{3.33}$$

Electron transport-limited: The volumetric rate of electron transport (in Eq. 3.17; mol/m^3.s), J, can be described in terms of light limited, J_{ll}, and light saturated, J_{ls},

rates of electron transport in PS II (Buckley and Farquhar, 2004):

$$J = \frac{J_{ll} + J_{ls} - \sqrt{(J_{ll} + J_{ls})^2 - 4\theta J_{ll} J_{ls}}}{2\theta} \alpha_t \tag{3.34}$$

where $\theta = 0.97$. The light limited rate of electron transport (mol/m$^2 \cdot$ s), J_{ll}, is determined from the amount of the available light (mol/m$^2 \cdot$ s), I, to be absorbed by the chlorophyll pigments which can vary by the light wavelength (Vogelmann and Evans, 2002):

$$J_{ll} = \alpha_{PSII} \Phi_{PSII} I \tag{3.35}$$

where $\alpha_{PSII} = 0.5$ is the fraction of absorbed photons driving PS II electron transport, and $\Phi_{PSII} = 0.85$ mol/mol is the maximum quantum efficiency of PS II in electron transport. The distribution of light within the leaf tissue was calculated using Beer-Lambert's law:

$$\frac{\partial I}{\partial z} = a_{chl} I \tag{3.36}$$

where a_{chl} is the absorption coefficient of chlorophyll a which depends on the specific absorption (m^2/mol) (Mitchell and Kiefer, 1988; Vogelmann and Evans, 2002), a^*_{chl}, and the density of chlorophyll a within the leaf tissue (mol/m^3), ρ_{chl}:

$$a_{chl} = a^*_{chl} \rho_{chl} \tag{3.37}$$

The profile of chlorophyll density within spinach leaves was obtained from Vogelmann and Evans (2002) who measured the chlorophyll fluorescence profiles within spinach leaves. The light saturated rate of electron transport (mol/m$^2 \cdot$ s) is defined as:

$$J_{ls} = \beta J_{max} \tag{3.38}$$

where β is defined here as the relative photosynthetic capacity whose profile was obtained from Evans and Vogelman (2003), and J_{max} is the maximum rate of electron transport (mol/m$^2 \cdot$ s), and can be calculated by (Harley et al., 1992):

$$J_{max} = 1 \times 10^6 \frac{\exp\left(37.08 - \frac{79500}{RT}\right)}{1 + \exp\left(\frac{650T - 201000}{RT}\right)} \tag{3.39}$$

TPU-limited: A value of 9.19×10^{-6}mol/m$^2 \cdot$ s was adopted for the TPU rate (in Eq. 3.18; mol/m$^2 \cdot$ s), T_p (Harley et al., 1992; Ho et al., 2016). So, the volumetric value of TPU rate is:

$$T_p^* = T_p \alpha_t \tag{3.40}$$

3.3.6 Solution procedure

The governing equations were solved using a commercial finite element package, COMSOL Multiphysics version 5.4 (COMSOL Multiphysics Burlington, MA). The time-step size was varied between 0.001 s to 0.1 s. The relative and absolute tolerances were 0.001 for all computations. A mesh of 2477 triangular elements was used for the 2D axisymmetric model for which the maximum element size was 1 μm within the mesophyll tissue and far from the stomatal cavity. MUMPS direct solver was used to solve the algebraic equations resulting from the finite element method. Run time for the simulations ranged from few to several minutes on a Windows machine with 32 GB of RAM, and 2 GHz dual core Intel© Xeon© CPU E5-2620 processor.

3.4 Experimental procedure

In order to validate the model predictions for the amount of bacterial infiltration, a couple of microbiological experiments were performed (Fig 3.6). In short, during each experiment, baby spinach leaves were inoculated with a prescribed bacterial suspension, and exposed to a certain illumination condition. Then the amount of infiltrated bacteria were determined by plating methods. In addition to the microbiological experiments, stomatal aperture of spinach leaves under exposure of different illumination conditions were examined using microscopy imaging. Details of all experiments are discussed here.

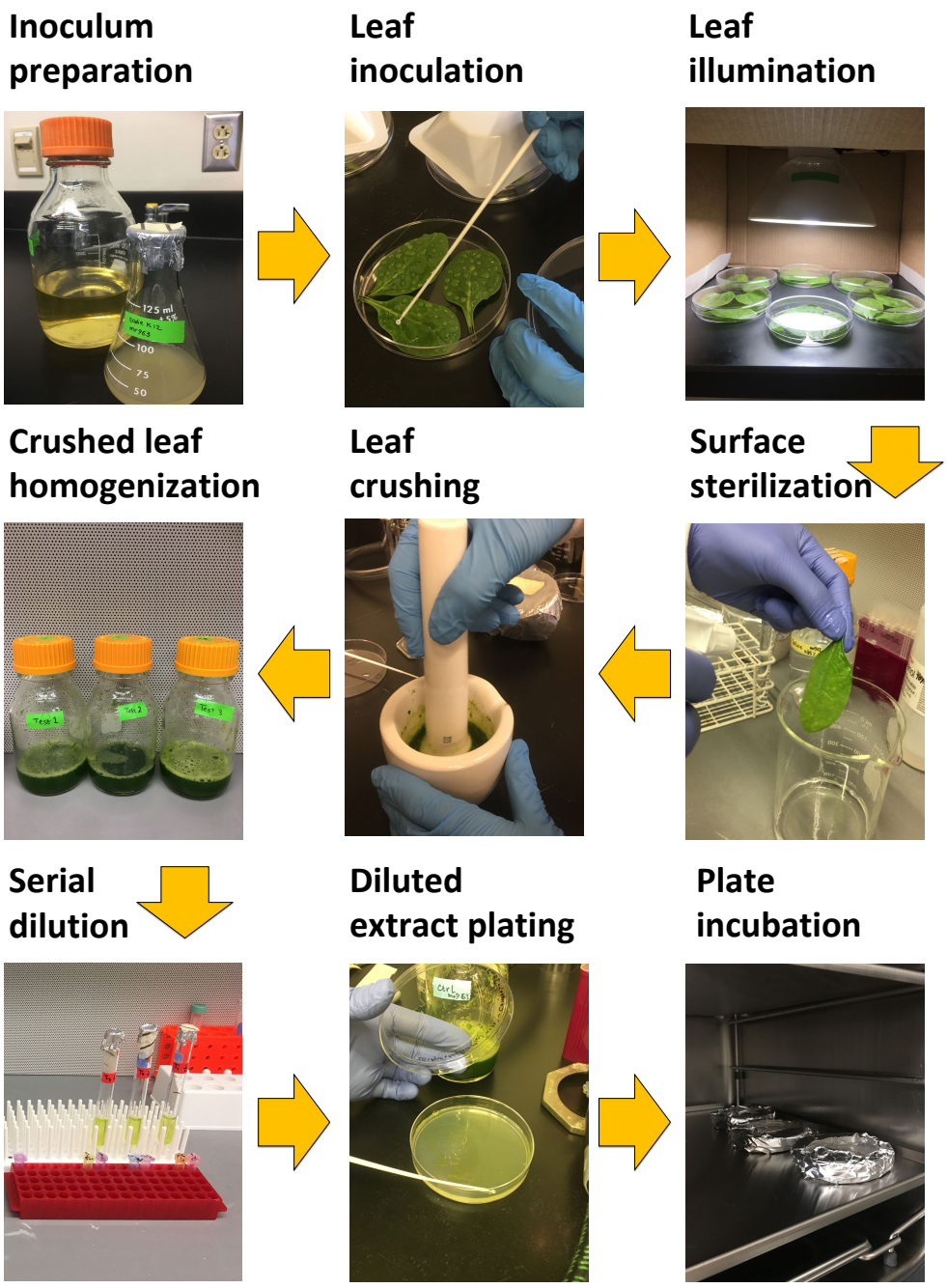

Figure 3.6: Experimental procedure to determine total amount of infiltration.

3.4.1 Bacterial strains and inoculum preparation

A loop of frozen (at -80 °C) culture of *E. coli* cells (wild type ampicillin-resistant K-12 MG1655, or incessantly motile (but not chemotactic) kanamycin-resistant K-12 BW25113 (Δ *CheZ*), gifts from John March, Cornell University) were grown in sterile LB broth (a 25 g/l of LB powder dissolved in Milli-Q water supplemented with 100 μg/ml ampicillin or 30 μg/ml kanamycin) and inoculated overnight in a shaker at 37 °C and 220 rpm. This was followed by a second overnight incubation in fresh LB broth. The bacterial culture were then harvested by two successive centrifugation steps (Sorrvall legend RT+centrifuge, Thermo Scientific, USA) at 2700 g for 10 min to efficiently remove the LB broth. The cell pellets were resuspended in sterile 0.85% NaCl (saline) solution and the concentration of final bacterial populations was adjusted to $\sim 10^8$ CFU/ml by using spectrophotometry analysis (Agilent Technologies, Inc., Mattapoiset, MA).

3.4.2 Leaf inoculation and light exposure

Fresh baby spinach leaves were purchased at a local retail store. Samples of 5 g containing about 8 leaves were used. The leaves were placed in sterile petri dishes with cover lids and were kept at room temperature for about 45 min under the illumination condition that was under study. This was done to make sure that the leaf microstructures are in equilibrium with the illumination condition. Then the samples were spot inoculated with 500 μl of *E. coli* cell suspension to reach an initial population of $\sim 3 \times 10^7$ CFU/g. The inoculum was then gently spread on the leaf surface using a sterile loop to uniformly cover the surface. The lid of petri dishes were placed to avoid evaporation of the inoculum at the leaf surface. The samples were exposed to white/blue/red/green light with intensity of 100 μmol/m$^2 \cdot$ s, or kept in dark. All exposures were performed at room temperature for 2 h. The light intensity was measured by a digital luxmeter (PM6612, Peak Meter ®, China) with $\pm$3% accuracy. The illumination chamber were

shielded thoroughly to make sure that the samples would only receive the expected wavelengths.

3.4.3 Bacterial infiltration assay

After exposure treatment, the surface of the leaves were washed by sterile 0.85% NaCl (saline) and let to dry. Then, they were sprayed with 70% ethanol in two successive steps to remove any surface bacteria. The surface sterilizatrion were examined (Fig 3.7) by gently pushing the surface of some treated leaves on LB agar plates and incubate them. The surface sanitation was considered effective when more than 99.99999% of inoculated bacteria at the surface were inactivated (about 8-log CFU/ml reduction).

The surface sterilized leaves of each sample were crushed in a sterile bowl and was added with 45 ml sterile 0.85% NaCl (saline). The homogenized sample were serially diluted in sterile 0.85% NaCl (saline) solution and surface plated onto LB agar containing 100 μg/ml ampicillin or 30 μg/ml kanamycin. To make sure that the natural microbiota on the leaf surface were not growing in the growth medium containing ampicllin or kanamycin, control samples without incubation were also homogenized and plated (Fig 3.8). The inoculated petri dishes were incubated at 30°C for 24 h, and the colonies were enumerated to find the bacterial count. No growth was observed in any of the uninoculated plates (data not shown) implying that the natural microbiota were not ampicillin or kanamycin resistant and would not be counted as infiltrated bacteria.

3.4.4 Microscopy imaging of stomatal aperture

The microscopy imaging experiments were done using an epi-fuorescent microscope (DM5500, Leica Microsystems, Exton, PA, USA) with 20x or 63x water immersion objectives. Before microscopy, three leaves were either exposed to white/blue/red/green

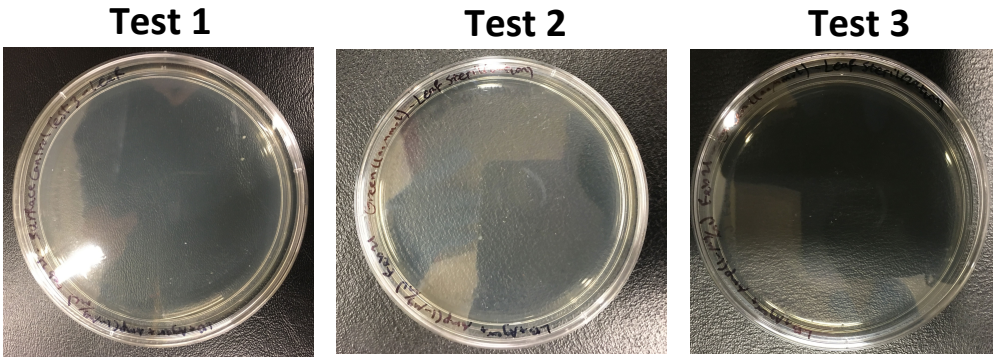

a.

Bacteria: ampicillin-resistant *E. coli* K-12 MG1655

	Illumination condition	Number of colonies detected	Dilution factor	Leaf side	Number of bacteria at the leaf surface after surface sanitation (CFU)
Test 1	White 100 (µmol/m².s)	3	1/1	Adaxial	3
Test 2	Green 100 (µmol/m².s)	1	1/1	Adaxial	1
Test 3	Green 100 (µmol/m².s)	0	1/1	Adaxial	0

b.

Figure 3.7: Results of the leaf surface sanitation treatments. The inoculated surface of the leaves were washed by sterile 0.85% NaCl (saline), after 2 h illumination, and let to dry. Then, they were sprayed with 70% ethanol in two successive steps to remove any surface bacteria.

light with an intensity of 100 μmol/m$^2 \cdot$ s, or were kept in dark for 45 min. After illumination, samples (5 mm × 5 mm) from three arbitrary locations of each leaf were cut and immediately used for microscopy. For each experimental condition, data of stomatal aperture were gathered from more than 100 stomata. The measurements were done using ImageJ software.

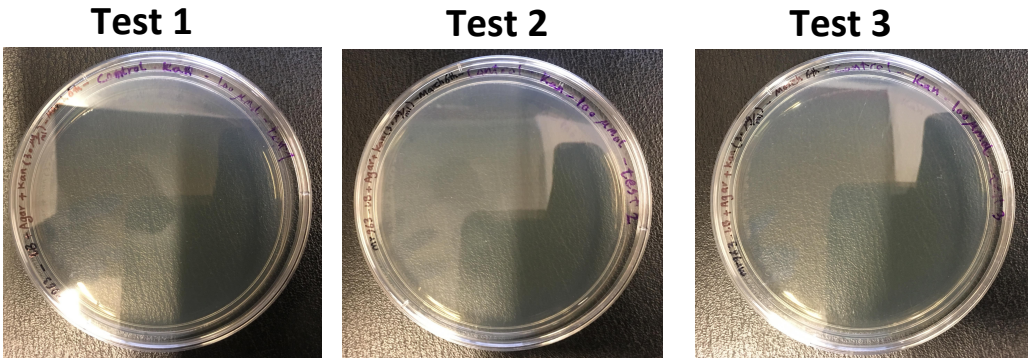

a.

No antibiotic-resistant bacteria

	Illumination condition	Antibiotic	Dilution factor	Leaf side	Number of colonies detected
Test 1	White 100 (µmol/m^2.s)	Kanamycin	1/500	Adaxial	0
Test 2	White 100 (µmol/m^2.s)	Kanamycin	1/500	Adaxial	0
Test 3	White 100 (µmol/m^2.s)	Kanamycin	1/500	Adaxial	0
Test 4	White 100 (µmol/m^2.s)	Ampicillin	1/500	Adaxial	0
Test 5	White 100 (µmol/m^2.s)	Ampicillin	1/500	Adaxial	0
Test 6	White 100 (µmol/m^2.s)	Ampicillin	1/500	Adaxial	0

b.

Figure 3.8: Control tests to make sure the natural microbiota on the leaf surface were not growing in the growth medium containing ampicllin or kanamycin.

3.5 Results and discussion

In this section, the model predictions and validations are presented for the rate of CO_2 fixation, and the amount of sugar production during photosynthesis. This is followed by studying the effects of light intensity and wavelength, bacterial transport mode, leaf side and stomatal defense on the amount of infiltration. After a sensitivity analysis on the most important parameters in the model, the primary and secondary factors affecting the infiltration are highlighted.

3.5.1 CO_2 fixation and nutrients production

To show the performance of the FvCB model (Farquhar et al., 1980) in predicting the rate of photosynthesis when coupled to the main model (Fig. 3.5), predicted rate of CO_2 assimilation in spinach leaves are compared with the experimental measurements of Harris et al. (1986) (Fig. 3.9a). The leaf was initially assumed to be in a dark condition where stoma was closed. As illumination occurred, the stoma was gradually opened by the moving mesh approach with a prescribed speed of 1 nm/s which is analogous to the rate of stomatal opening in 1 h (by assuming a constant rate). As CO_2 diffuses into the leaf tissue during illumination, the rate of CO_2 fixation increases until it equilibrates with the exposed conditions. A step function was used here to help predictions better match the experimental condition reported in Harris et al. (1983). The results are in agreement with predicted and experimental values of the rate of photosynthesis in tomato leaves (Ho et al., 2016).

Profiles of carbon fixation in the leaves are similar to those of light absorption through the leaf tissue (Evans, 1995). The predicted profiles of CO_2 fixation within the leaf tissue were qualitatively compared with experimental profiles of ^{14}C fixation within spinach leaves obtained from measurement of chlorophyll fluorescence profiles

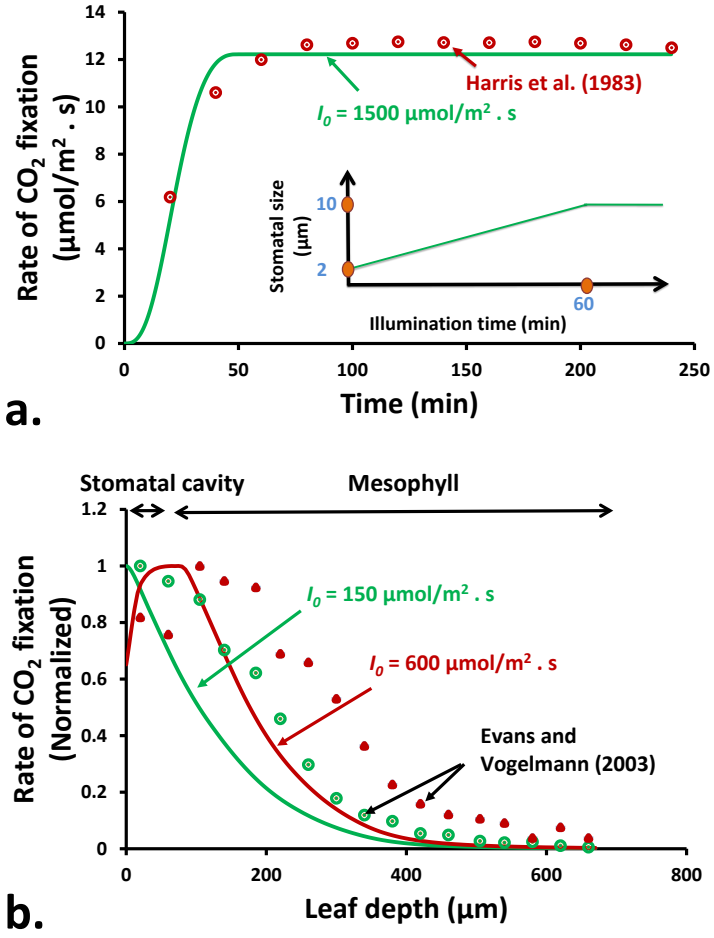

Figure 3.9: a) Variation of the rate of CO_2 fixation within spinach tissue at white light intensity of 1500 μmol/m$^2 \cdot$ s and atmospheric CO_2 level of 0.013 mol/m^3. The predicted results are compared with experimental data of Harris et al. (1983). b) Variation of the normalized rates of CO_2 fixation within the leaf tissue. The trends are compared with normalized trends of flourescent emissions within spinach tissue (Evans and Vogelmann (2003).

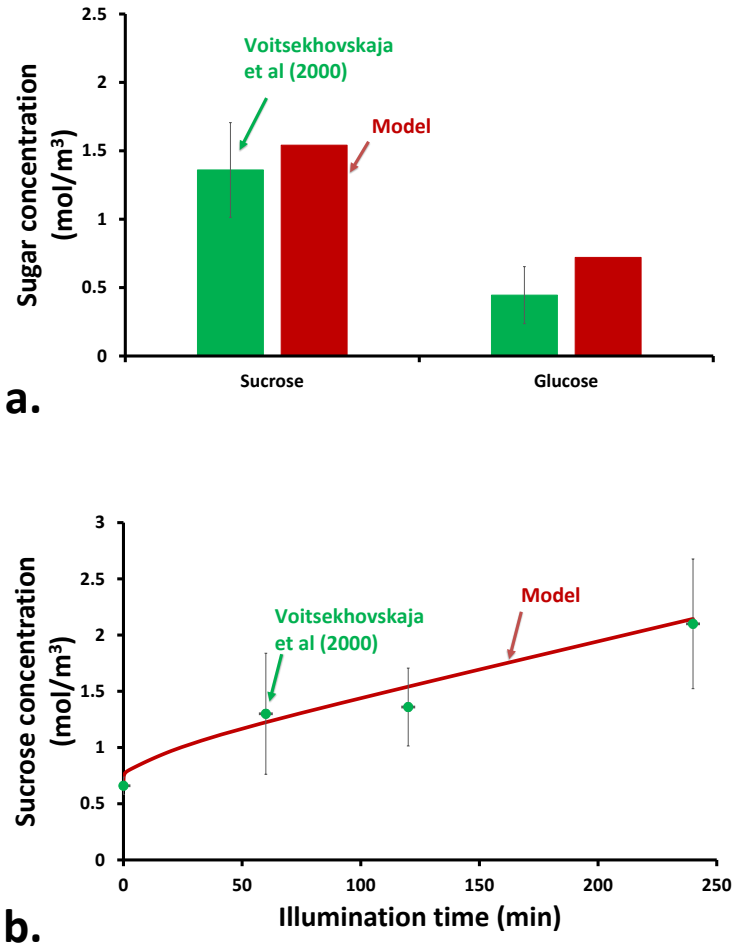

Figure 3.10: a) Total amount of apoplastic sucrose and glucose concentrations in spinach leaves, after 120 min illumination with light intensity of 300 μmol/m^3 · s (Voitsekhovskaja et al., 2000), and b) predicted and experimental (Voitsekhovskaja et al., 2000) variation of apoplastic sucrose concentration in spinach leaves during 4 h of illumination with a light intensity of 300 μmol/m^3 · s.

(Evans and Vogelmann, 2003) (Fig. 3.9b). The rate of carbon fixation declines as the light is absorbed by the chlorophyll pigments within the chloroplasts. It remains higher through the leaf tissue when a higher level of light intensity is exposed to the leaf because chlorophyll pigments in the depth of the leaf can absorb more light. Similar distributions of CO_2 fixation within the leaf tissue can be obtained for red, green and white lights (Nishio et al., 1993; Evans and Vogelmann, 2003; Evan et al., 2017).

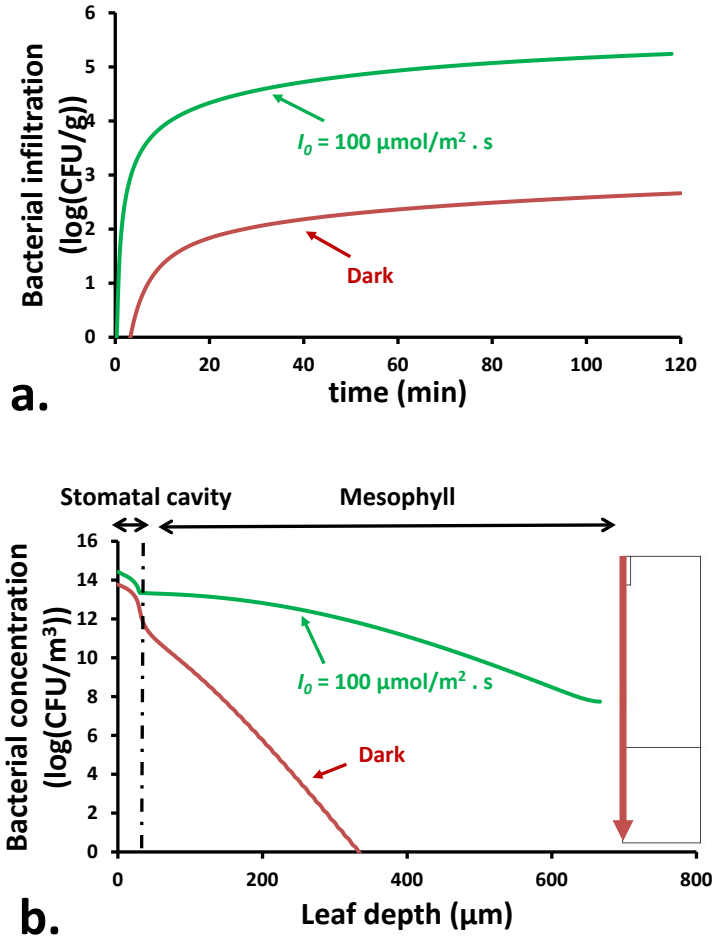

Figure 3.11: Variations of the a) amount and b) depth of bacterial infiltration into the leaf tissue under white light intensity of 100 μmol/m^2 · s and dark conditions.

As sugar is synthesized within the plant cells, it is effluxed by SWEET transporter proteins located at the plasma membrane into the apoplast. This results in an increase in the concentration of apoplastic sugar while the leaf is illuminated. The apoplastic sucrose and glucose in spinach leaves, with inhibited phloem transport, were measured in Voitsekhovskaja et al. (2000) and are compared with the predicted data and trends in Fig. 3.10a and Fig 3.10b, respectively. The data presented in Fig. 3.10 are for the condition that bacteria are absent.

3.5.2 Bacterial infiltration

Effect of light exposure on infiltration

Typical variations of total amount of bacterial infiltration into the plant leaf is illustrated in Fig. 3.11a. Also, the distribution of the infiltrated bacteria within the leaf depth is shown in Fig. 3.11b. These simulations assume that the bacteria is *E. coli* , and the leaf was initially in equilibrium with the illumination or dark conditions. Under light condition, stoma is open and photosynthesis and sugar efflux through SWEET transporters increase the level of apoplastic glucose. The infiltration happened mainly during the initial 30-min of the process. This is because the level of apoplatic sugar is high and a large concentration gradient of glucose causes enhanced bacterial chemotaxis toward the leaf tissue. During dark conditions, all stomata are not tightly closed (Fig. 3.12). The observations on iceberg lettuce also showed 1% of the stomata were open during dark condition (Kroupitski et al., 2009). This brings up an opportunity for the bacteria to infiltrate the leaf (Fig. 3.11a) through the available openings (Fig. 3.11a). Even very narrow openings slightly larger than bacterial cell diameter was shown to be enough for infiltration (Mannik et al., 2009). However, the amount of infiltration is much less than that in light, as the stomatal size is smaller and photosynthesis is inhibited under dark condition. Evidence shows that *Salmonella enterica* serovar Typhimurium was able to infiltrate iceberg lettuce leaves during dark condition, although the incidence of infiltrated stomata in dark was much less than that occurred under exposure of light (Kroupitski et al., 2009). The infiltration depth for the light condition was more than dark (Fig. 3.11b) due to more nutrient availability at the deeper locations of the leaf tissue when is exposed to light. Infiltrated bacteria are more concentrated within the stomatal cavity and distribute around as they reach the mesphyll tissue.

The predicted total amounts of infiltrated bacteria into spinach leaves are compared with the experimental data in Fig. 3.13, showing a reasonable predictions. The error bar

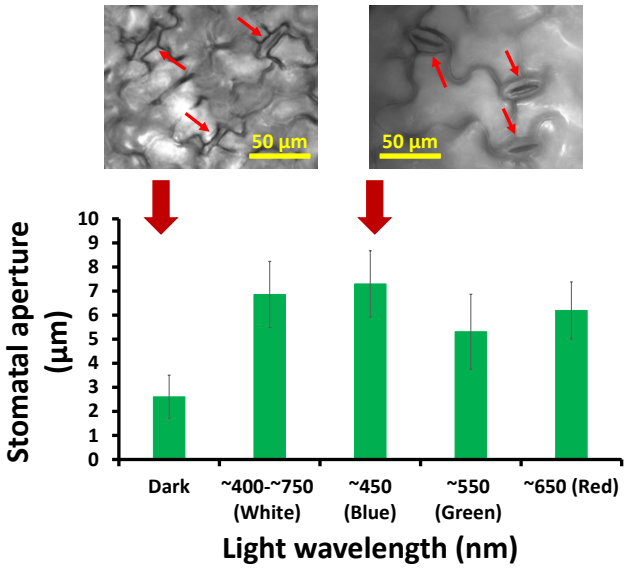

Figure 3.12: Measured stomatal aperture of spinach leaves under different light colors of 100 μmol/m^2 · s, and dark condition for 45 min. Representative confocal microscopy images related to dark condition (smallest aperture) and blue light illumination condition (widest aperture) are shown as insets. Red arrows in the inset images show the location of the stomata.

at experimental data shows the standard deviations, and those at predicted data reflect the effect of 30% change in the stomatal size. An increase in the light intensity created more bacterial infiltration into the leaf tissue (Fig. 3.13a). This is because the rate of photosynthesis is higher at higher light intensities which enhances the bacterial chemotaxis. In Fig. 3.13a, the control condition confirms that no natural microbiota at/inside the leaf tissue were able to survive at the LB-agar plates that were supplemented with ampicillin/kanamycin. Therefore, all observed colonies were related to the antibiotic-resistant bacterial strains. Light wavelength can also affect the amount of infiltration by altering the amount of nutrients production in the leaf and affecting size of the stomatal aperture. The highest infiltration was observed for the blue light exposure. A high intensity blue light (similar to that of other lights) can trigger photosynthesis in the guard cells leading to accumulation of sugars and opening of stomata. However, blue light can also serve as a signal in the stomatal opening process: a low intensity blue light is

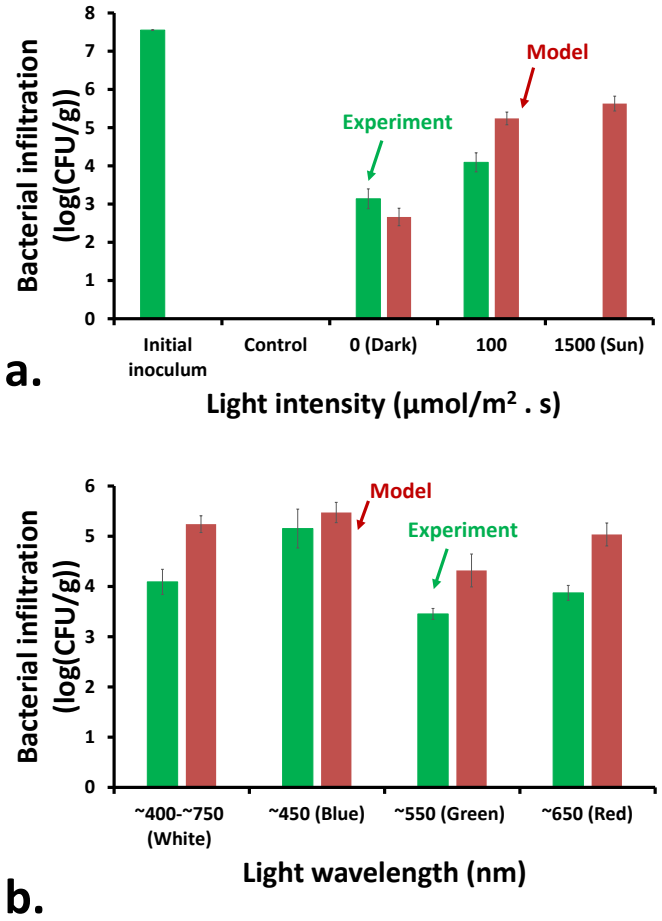

Figure 3.13: Total amount of bacterial infiltration for different levels of a) light intensities and b) wavelengths (at 100 μmol/m^2 $\cdot$ s).

enough to activate the electrogenic H^+ pumps located at the plasma membrane of the guard cells, leading to membrane hyperpolarization, K^+ uptake, and stomatal opening (Shimazaki et al., 2007). Therefore, the stomatal size under blue light are larger than that of other wavelengths (Fig. 3.12; Lurie, 1978).

Exposure to green light led to the least amount of bacterial infiltration (Fig. 3.13b). This is partly attributed to the size of stomatal opening under green light which is the least among other light wavelengths (Fig. 3.12; Kana and Miller, 1976). Also, green light is absorbed less than other wavelenghts by chlorophyll pigments, leading to less rate of photosynthesis in the mesophyll tissue, and weaker bacterial chemotaxis. Fig-

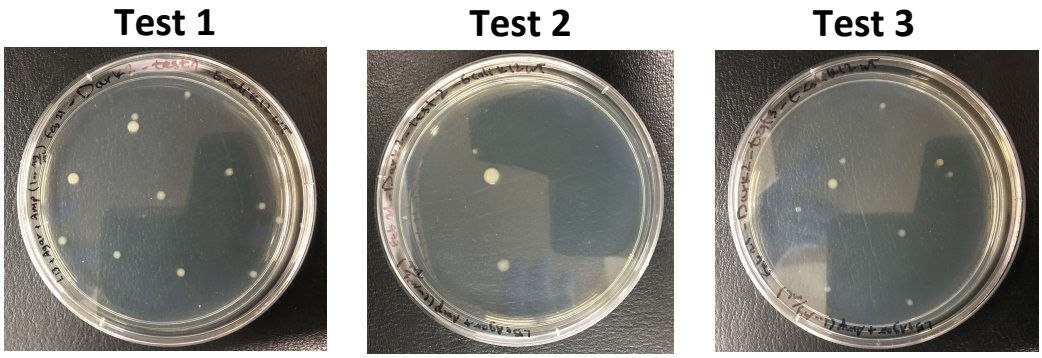

a.

Bacteria: ampicillin-resistant *E. coli* K-12 MG1655

	Illumination condition	Number of colonies detected	Dilution factor	Leaf side	Leaf sample weight (g)	Number of bacterial infiltration into the leaves (CFU/g)	Bacterial infiltration (log CFU/g)
Test 1	Dark	12	1/500	Adaxial	5.06	2400	3.38
Test 2	Dark	3	1/500	Adaxial	5.05	600	2.78
Test 3	Dark	9	1/500	Adaxial	5.01	1800	3.26
Mean						1600	3.13
Standard deviation						748.3	0.26

b.

Figure 3.14: Results of the colony growth of ampicillin-resistant *E. coli* K-12 MG1655 on LB-agar medium containing 100 g/ml ampicillin. The inoculated leaves were kept in dark condition for 2 h.

ures 3.14-3.18 show the details of the experimental data of bacterial infiltration that were compared with the model predictions in Fig 3.13.

The effect of light intensity and wavelength on the bacterial infiltration might be more complicated than what is considered in the present model. It has been shown that *E. coli* does phototaxis away from blue light (Taylor and Koshland JR, 1975; Braatsch and Klug, 2004), and gets more motile at high light intensities (Perlova et al., 2017, Wright et

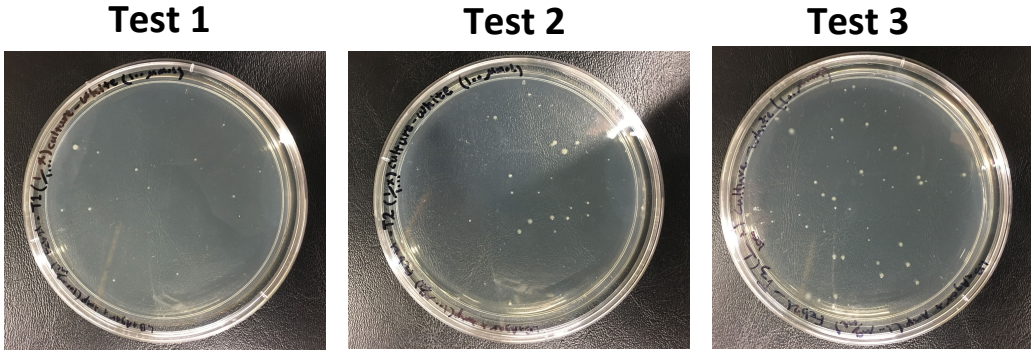

a.

Bacteria: ampicillin-resistant *E. coli* K-12 MG1655

	Illumination condition	Number of colonies detected	Dilution factor	Leaf side	Leaf sample weight (g)	Number of bacterial infiltration into the leaves (CFU/g)	Bacterial infiltration (log CFU/g)
Test 1	White 100 (µmol/m².s)	14	1/1000	Adaxial	5.015	5600	3.75
Test 2	White 100 (µmol/m².s)	39	1/1000	Adaxial	5.011	15600	4.19
Test 3	White 100 (µmol/m².s)	54	1/1000	Adaxial	5.013	21600	4.33
Mean						14266.7	4.09
Standard deviation						6599.7	0.25

b.

Figure 3.15: Results of the colony growth of ampicillin-resistant *E. coli* K-12 MG1655 on LB-agar medium containing 100 g/ml ampicillin. The inoculated leaves were exposed to white light, from adaxial side, with an intensity of 100 μmol/m^2 $\cdot$ s for 2 h.

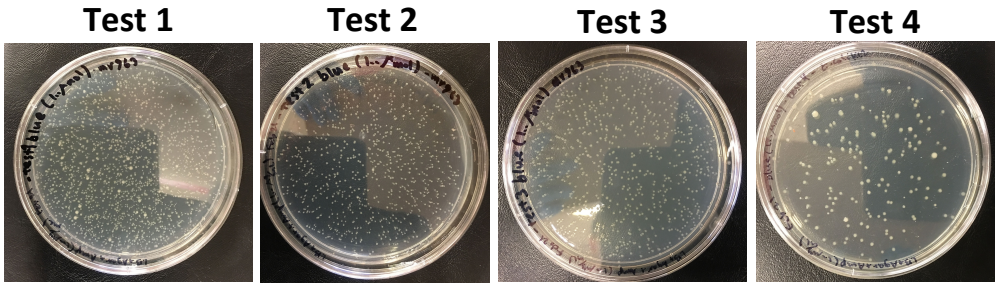

a.

Bacteria: ampicillin-resistant *E. coli* K-12 MG1655

	Illumination condition	Number of colonies detected	Dilution factor	Leaf side	Leaf sample weight (g)	Number of bacterial infiltration into the leaves (CFU/g)	Bacterial infiltration (log CFU/g)
Test 1	Blue 100 (µmol/m².s)	1978	1/500	Adaxial	5.012	395600	5.60
Test 2	Blue 100 (µmol/m².s)	887	1/500	Adaxial	5.010	177400	5.25
Test 3	Blue 100 (µmol/m².s)	861	1/500	Adaxial	5.021	172200	5.23
Test 4	Blue 100 (µmol/m².s)	170	1/500	Adaxial	5.011	34000	4.53
Mean						194800	5.15
Standard deviation						129413	0.39

b.

Figure 3.16: Results of the colony growth of ampicillin-resistant *E. coli* K-12 MG1655 on LB-agar medium containing 100 g/ml ampicillin. The inoculated leaves were exposed to blue light, from adaxial side, with an intensity of 100 μmol/m^2 $\cdot$ s for 2 h.

al., 2006). Therefore, a phototactic response and variations in the bacterial motility are also possible to contribute in light-driven bacterial infiltration into the leaf tissue.

An overview of the underlying mechanisms leading to light-driven bacterial infiltration is shown in Fig. 3.19.

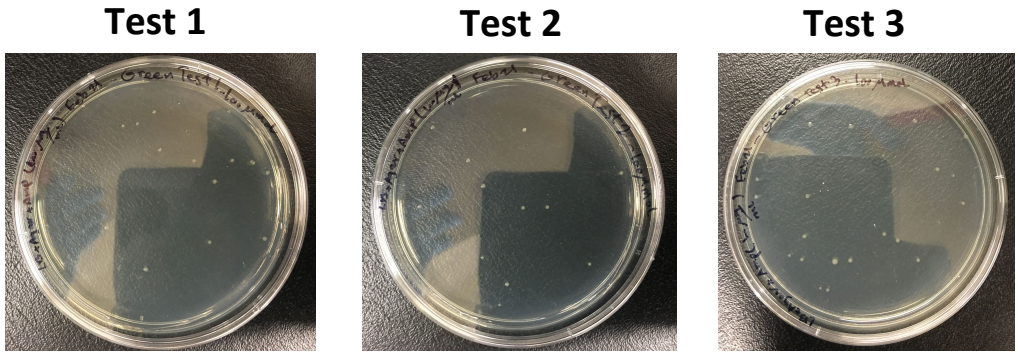

a.

Bacteria: ampicillin-resistant *E. coli* K-12 MG1655

	Illumination condition	Number of colonies detected	Dilution factor	Leaf side	Leaf sample weight (g)	Number of bacterial infiltration into the leaves (CFU/g)	Bacterial infiltration (log CFU/g)
Test 1	Green 100 (µmol/m².s)	13	1/500	Adaxial	5.051	2600	3.42
Test 2	Green 100 (µmol/m².s)	11	1/500	Adaxial	5.018	2200	3.34
Test 3	Green 100 (µmol/m².s)	20	1/500	Adaxial	5.008	4000	3.60
Mean						2933.3	3.45
Standard deviation						771.7	0.11

b.

Figure 3.17: Results of the colony growth of ampicillin-resistant *E. coli* K-12 MG1655 on LB-agar medium containing 100 g/ml ampicillin. The inoculated leaves were exposed to green light, from adaxial side, with an intensity of 100 μmol/m^2 $\cdot$ s for 2 h.

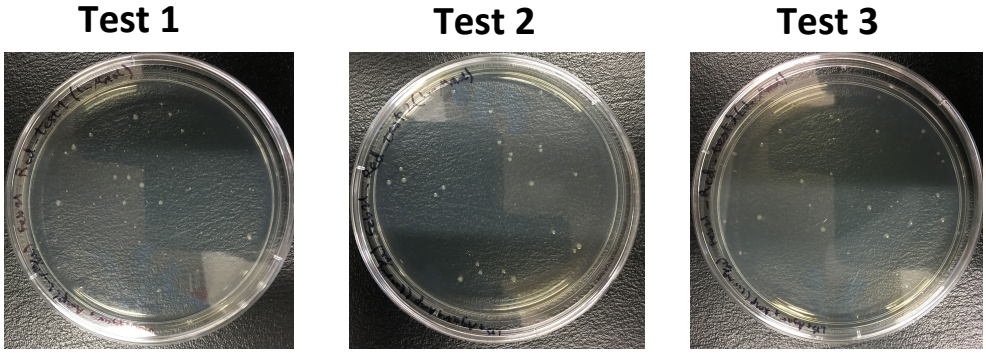

a.

Bacteria: ampicillin-resistant *E. coli* K-12 MG1655

	Illumination condition	Number of colonies detected	Dilution factor	Leaf side	Leaf sample weight (g)	Number of bacterial infiltration into the leaves (CFU/g)	Bacterial infiltration (log CFU/g)
Test 1	Red 100 (μmol/m².s)	60	1/500	Adaxial	5.010	12000	4.08
Test 2	Red 100 (μmol/m².s)	27	1/500	Adaxial	5.021	5400	3.73
Test 3	Red 100 (μmol/m².s)	32	1/500	Adaxial	5.001	6400	3.81
Mean						7933.3	3.87
Standard deviation						2904.4	0.15

b.

Figure 3.18: Results of the colony growth of ampicillin-resistant *E. coli* K-12 MG1655 on LB-agar medium containing 100 g/ml ampicillin. The inoculated leaves were exposed to red light, from adaxial side, with an intensity of 100 μmol/m^2 $\cdot$ s for 2 h.

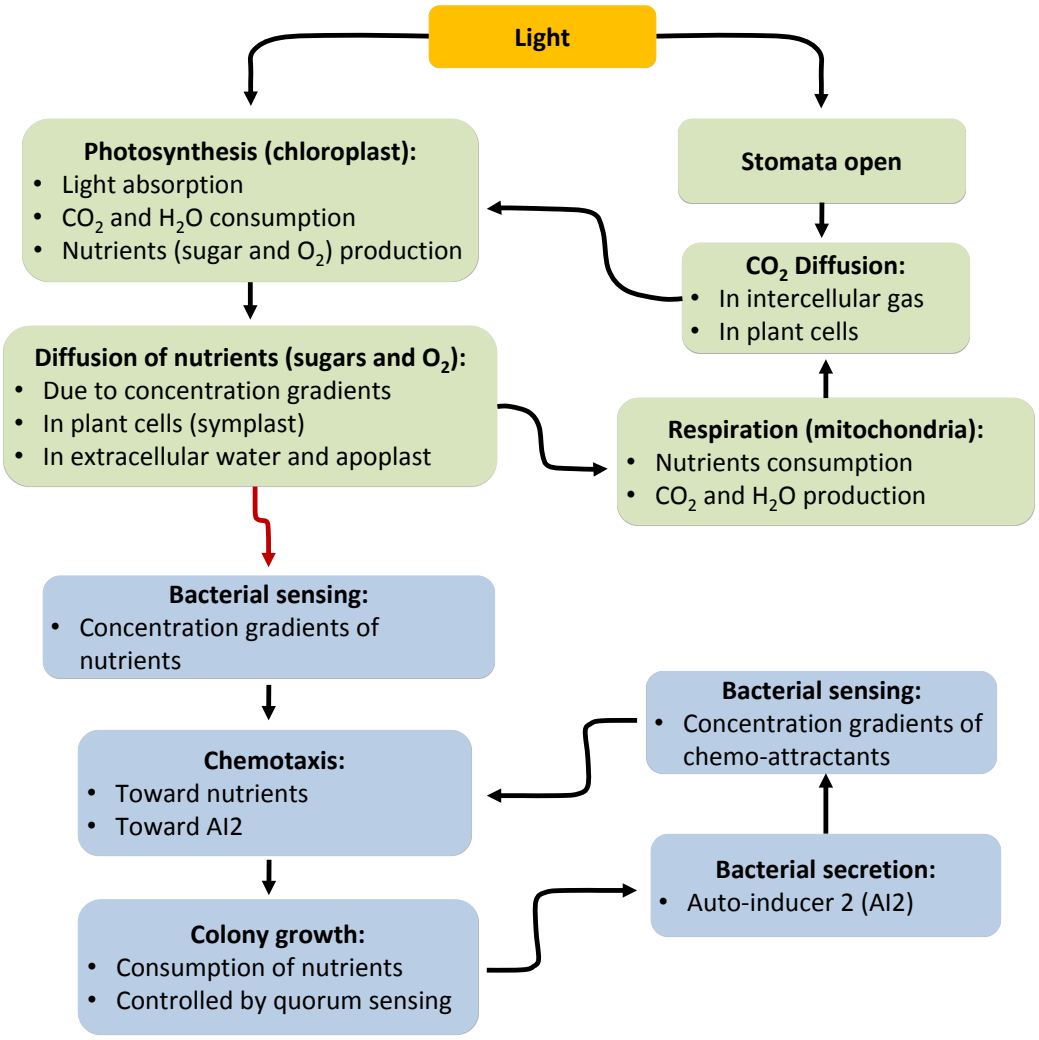

Figure 3.19: A flowchart of the mechanisms leading to light-driven bacterial infiltration within the leaf tissue.

Effects of motility and chemotaxis on infiltration

Total amount of bacterial infiltration for chemotactic and motile bacteria is compared in Fig. 3.20a with that of motile-only bacteria. Both experimental and computed results show that the ability to do chemotaxis plays a major role in infiltration. The wilde type *E. coli* K-12 MG1655 capable in both chemotaxis and motility showed 1.23 log (CFU/g) more infiltration compared with the *CheZ* mutant *E. coli* K-12 BW25113 which was motile-only. These results are also supported by previous observations showing

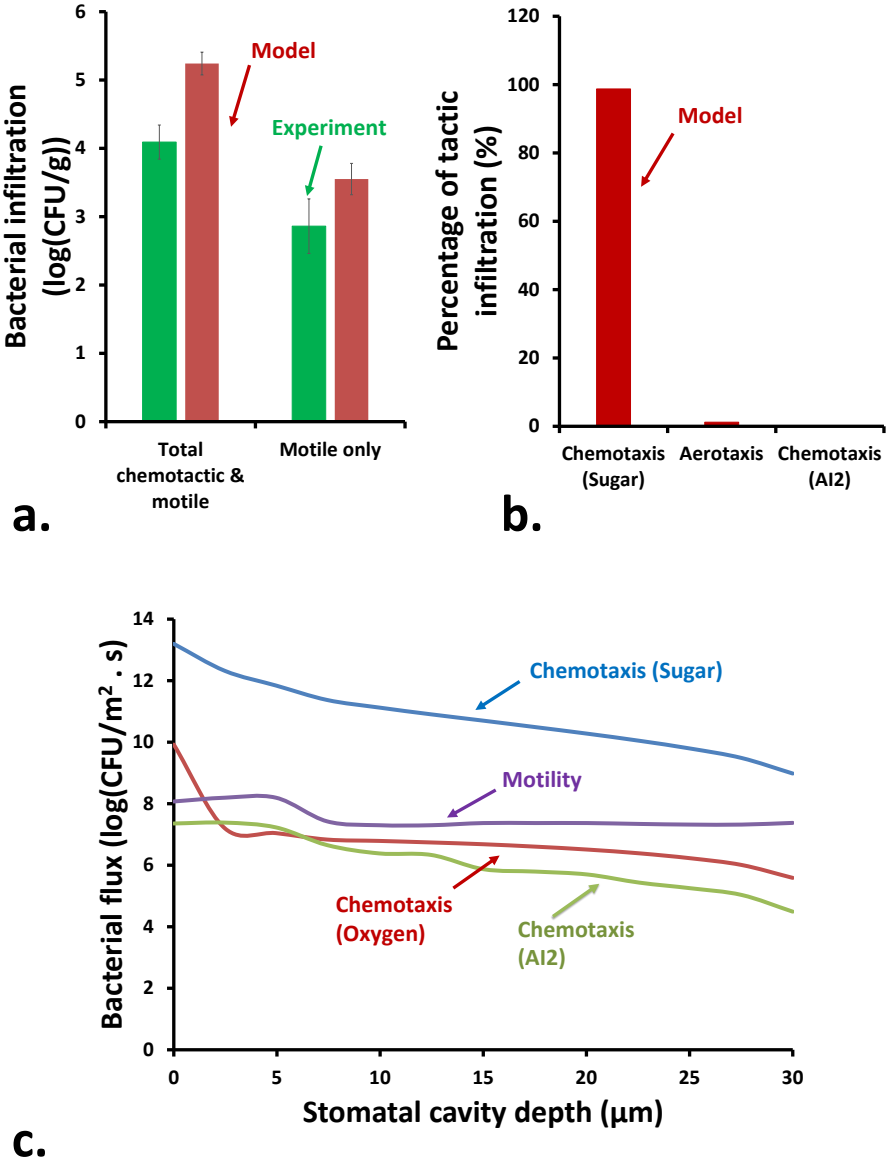

Figure 3.20: a) Total amount of bacterial infiltration for different modes of bacterial migration, b) relative contributions of the three different tactic migration modes, c) Variations of the downward bacterial flux within stomatal cavity after 1 h of illumination with white light intensity of 100 μmol/m^2 · s.

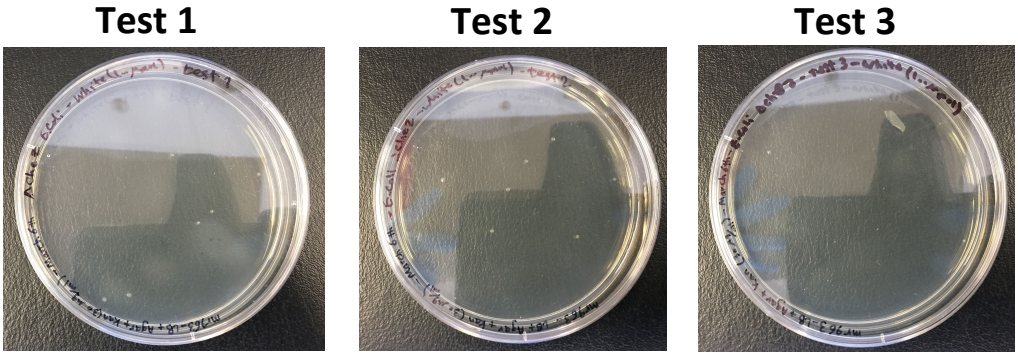

a.

Bacteria: kanamycin-resistant *E. coli* K-12 BW25113 (ΔCheZ)

	Illumination condition	Number of colonies detected	Dilution factor	Leaf side	Leaf sample weight (g)	Number of bacterial infiltration into the leaves (CFU/g)	Bacterial infiltration (log CFU/g)
Test 1	White 100 (µmol/m².s)	6	1/500	Adaxial	5.051	1200	3.08
Test 2	White 100 (µmol/m².s)	8	1/500	Adaxial	5.024	1600	3.20
Test 3	White 100 (µmol/m².s)	1	1/500	Adaxial	5.021	200	2.30
Mean						1000	2.86
Standard deviation						588.8	0.40

b.

Figure 3.21: Results of the colony growth of kanamycin-resistant *E. coli* K-12 BW25113 (Δ *CheZ*) on LB-agar medium containing 30 g/ml kanamycin. The inoculated leaves were exposed to white light, from adaxial side, with an intensity of 100 μmol/m^2 $\cdot$ s for 2 h.

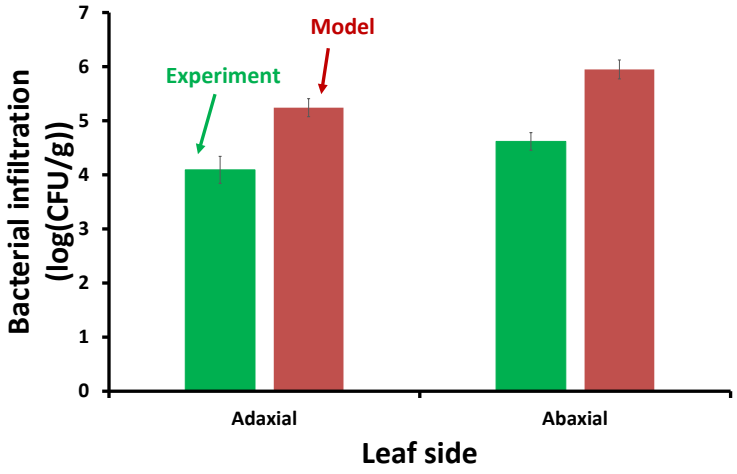

Figure 3.22: Total amounts of bacterial infiltration at white light intensity of 100 μmol/m^2 $\cdot$ s for two leaf sides.

that the entry of *cheY* mutants of *S. enterica* (defective in chemotaxis) into iceberg lettuce leaves, under light exposure, was significantly inhibited, while the wild type bacteria effectively reached the sub-epidermis leaf depths (Kroupitski et al., 2009). The simulation results show that chemotaxis toward sugar (glucose) had more than 98% contribution in the total tactic infiltration into the leaf tissue (Fig. 3.20b). This implies that the role of aerotaxis, and chemotaxis toward AI-2 was very insignificant. This is because large concentration gradients of sugar that are developeded between the leaf tissue and the water film at the leaf surface, causing a large chemotactic flux of bacteria within the stomatal cavity (Fig. 3.20c). Figure 3.21 shows the details of the experimental results of motile-only bacterial infiltration that was compared with model predictions in Fig. 3.20a.

Effects of leaf side and stomatal defense on infiltration

Leaf side can play a role in the amount of infiltration. Both experimental and computed results showed an increased bacterial infiltration for the abaxial side of the leaf (Fig. 3.22). When bacteria infiltrate the abaxial stomata they face the spongy mesophyll

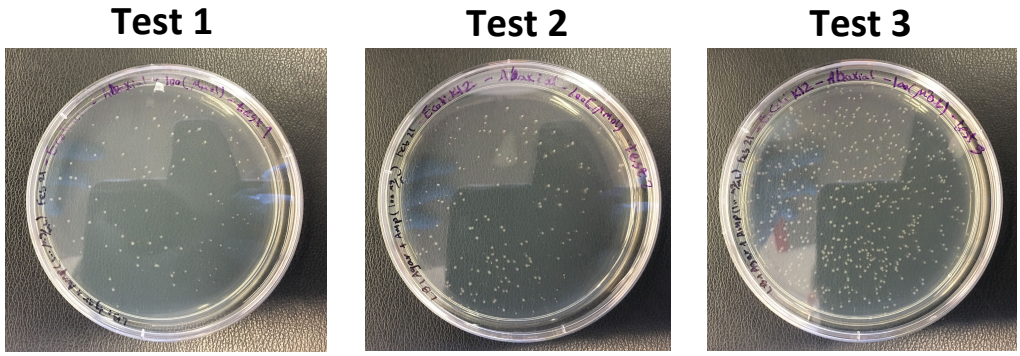

a.

Bacteria: ampicillin-resistant *E. coli* K-12 MG1655

	Illumination condition	Number of colonies detected	Dilution factor	Leaf side	Leaf sample weight (g)	Number of bacterial infiltration into the leaves (CFU/g)	Bacterial infiltration (log CFU/g)
Test 1	White 100 (µmol/m².s)	114	1/500	Abaxial	5.025	22800	4.36
Test 2	White 100 (µmol/m².s)	153	1/500	Abaxial	5.051	30600	4.49
Test 3	White 100 (µmol/m².s)	511	1/500	Abaxial	5.017	102200	5.01
Mean						51867	4.62
Standard deviation						35733	0.28

b.

Figure 3.23: Results of the colony growth of ampicillin-resistant *E. coli* K-12 MG1655 on LB-agar medium containing 100 g/ml ampicillin. The inoculated leaves were exposed to white light, from abaxial side, with an intensity of 100 μmol/m^2 $\cdot$ s for 2 h.

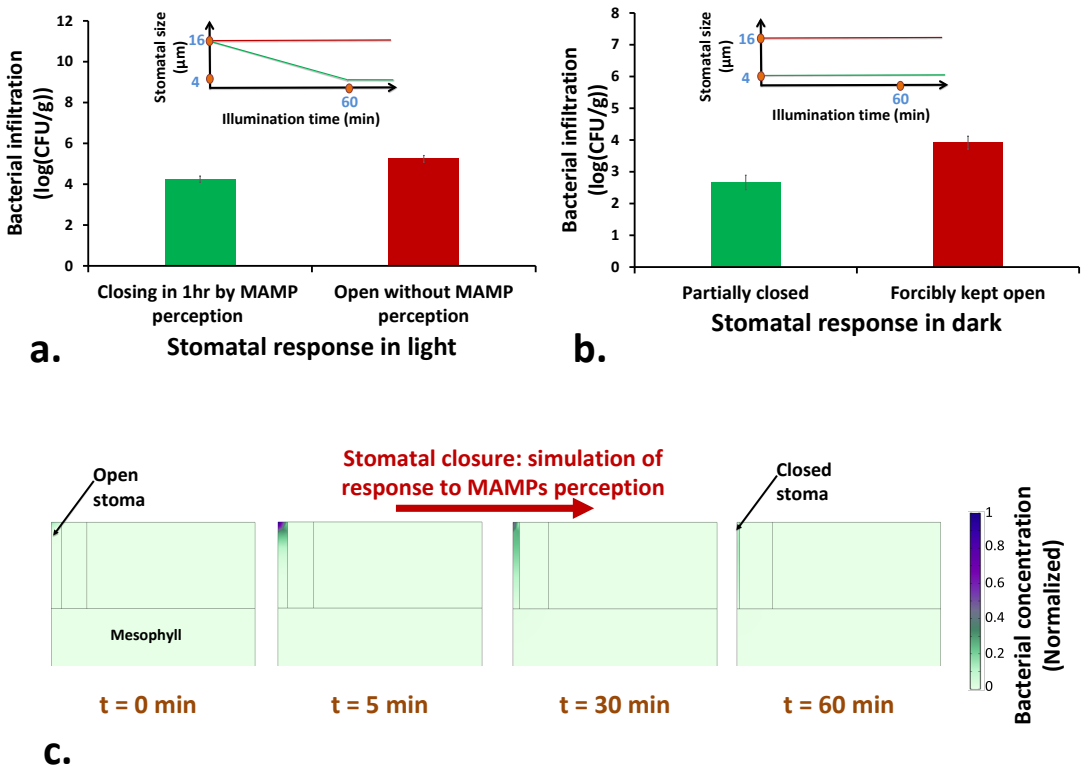

Figure 3.24: Total amounts of bacterial infiltration for various stomatal responses during a) light and b) dark conditions. c) Contours of bacterial concentration within the stomatal cavity that is being closed.

which are not as tightly packed as the palisade tissue. Moreover, the stomatal density at the abaxial side is much higher than that of the adaxial side (Panarese et al., 2016), providing more infiltration routes for bacteria. Therefore, although the photosynthesis is less in spongy region due to less chloroplast density of the spongy cells (compared to palisade cells), the total amount of infiltration from abaxial side is higher. Figure 3.23 shows the details of the experimental results of bacterial infiltration into abaxial side of the leaf that was compared with model predictions in Fig. 3.22.

Stomatal behavior depends on a number of biotic and abiotic factors. These external factors can influence the balance of phytohormones such as jasmonic acid (JA),

salicylic acid (SA), and abcisic acid (ABA) within the guard cells to affect the work-flow within the stomatal guard cells and regulation of the stomatal opening. In general, dominance of JA signaling over SA and ABA signaling (*e.g.*, in high humidity condition or under light exposure) favors stomatal opening while a reverse condition can lead to stomatal closure (Panchal and Melotto, 2017). Plant can sense the bacterial invasion through the pattern-recognition receptors (PRRs) that exist at the extracellular regions of the plant leaf. PPRs can sense the microbe-associated molecular patterns (MAMPs) (*e.g.*, components of bacterial surface structures such as flagellin, lipopolysaccharides) and trigger the pathogen-triggered immunity (PTI) which is the first line of the active defense against bacterial invasion (Melotto et al., 2014). One of the first outputs of the PTI, in response to perception of MAMPs, is stomatal closure. MAMPs perception up-regulates SA signaling and down-regulates JA signaling, leading to stomatal closure against bacterial invasion (Panchal and Melotto, 2017). Fig. 3.24a shows the amount of bacterial infiltration in light for the situations with or without stomatal defense capability. In the first scenario, the stomatal aperture becomes closed over 1 h (see Fig. 3.24c for visualization). This situation resembles the MAMPs-induced rapid stomatal closure ($<$ 2 h) of various plants in the presence of *E. coli* and *Pseudomonas syringae* pv. tomato (Melotto et al., 2006; Krouptiski et al., 2009). In the second scenario, stoma remains open in spite of bacterial presence in the medium. This situation is similar to the interaction of *S. enterica* serovar Typhimurium with lettuce leaves for which it was shown that the bacteria do not significantly induce stomatal closure (Krouptiski et al., 2009). As is shown in Fig 3.24a, presence of stomatal defense was effective in decreasing bacterial infiltration into the leaf for about 1-log. However, the stomatal defense is not always successful, since some bacteria such as *P. syringae* are able to override PTI and re-open the closed stomata after a few hours by expression of coronatine (COR), a molecular mimic of jasmonoyl-L-isoleucine (JA-Ile) that madiates stomatal opening (Panchal et al., 2016; Panchal and Melotto, 2017).

In Fig. 3.24b, the amount of bacterial infiltration for two different stomatal responses

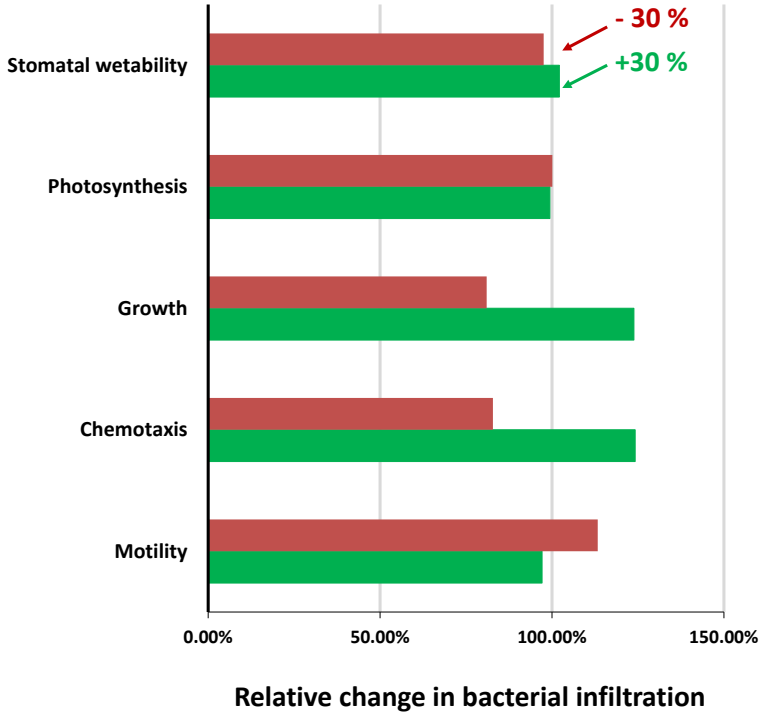

Figure 3.25: Sensitivity analysis on the leaf and bacterial parameters.

in dark are illustrated. In the first scenario, stomata are partially closed in dark which is a resemble of a natural situation. In the second scenario, the stomata are forcibly kept open in dark which is a simulation of applying stomatal opening reagent fusicoccin to the leaf (Turner and Graniti, 1969; Krouptiski et al., 2009), stomatal opening due to high humidity conditions (Panchal et al., 2016), or the situation when the dark-closed stomata are re-opened by COR during *P. syringae* pv. tomato infections (Panchal and Melotto, 2017). The amount of infiltration in the second scenario was more than 1-log higher than that of the first. The above predictions are in agreement with the experimental findings of Krouptiski et al. (2009) who showed that the amount of infiltration of *S. enterica* into iceberg lettuce leaves with forcibly-opened stomata was not significantly high, although it was higher than that of dark-closed stomata.

3.5.3 Sensitivity Analysis

To highlight the sole effects of motility, chemotaxis, growth, photosynthesis, and stomatal wettability on the amount of light-driven bacterial infiltration, parametric sensitivity analyses were performed (Fig. 5.12). While motile motion was shown to play a significant role in bacterial infiltration into plant leaves (Kroupitski et al., 2009), a 30% increase in the coefficient of random motility led to a 3% decrease in infiltration. Motility being a random movement, high motility reduces the chance of bacteria in the leaf surface water film to reach the stomatal pore. Increasing the bacterial chemotactic coefficient created 24% more infiltration. Greater infiltration from higher chemotaxis is expected since it is a directed movement toward stomata where sugar concentration are higher. Higher chemotaxis can also happen due to higher concentration gradients of nutrients. Addition of exogenous sugars (thus eliminating the concentration gradients) like glucose and fructose to the bacterial inoculum at the leaf surface was shown to significantly inhibit bacterial infiltration into iceberg lettuce during illumination (Kroupitski et al., 2009). Growth is also a significant factor in increasing the bacterial concentration stemming from infiltration. The effect of growth, of course, depends on the relative time scales of transport and growth which is described by Damkohler number (Da) (Plawsky, 2010). Considering the leaf depth as the characteristic length scale, Da was calculated in the range of 0.01 to 10, where the lower value belongs to a strong chemotactic transport and the higher one belongs to a motile-only transport. This range of Da shows that the growth rate is comparable to the transport rate, and thus can affect the bacterial concentration within the leaf tissue. The change in the rate of CO_2 fixation did not significantly impact the amount of infiltration which implying the mere existence of photosynthesis, regardless of its rate, is sufficient for promoting the infiltration. Stomatal wall wettability can play a role in availability of free water in the stomatal cavity (Nonomura et al., 2016) which facilitates bacterial transport into the leaf interior. Change in the stomatal wall wettability was simulated by changing the saturation of free water within the stomatal cavity region (Fig. 3.4a). A 30% decrease in

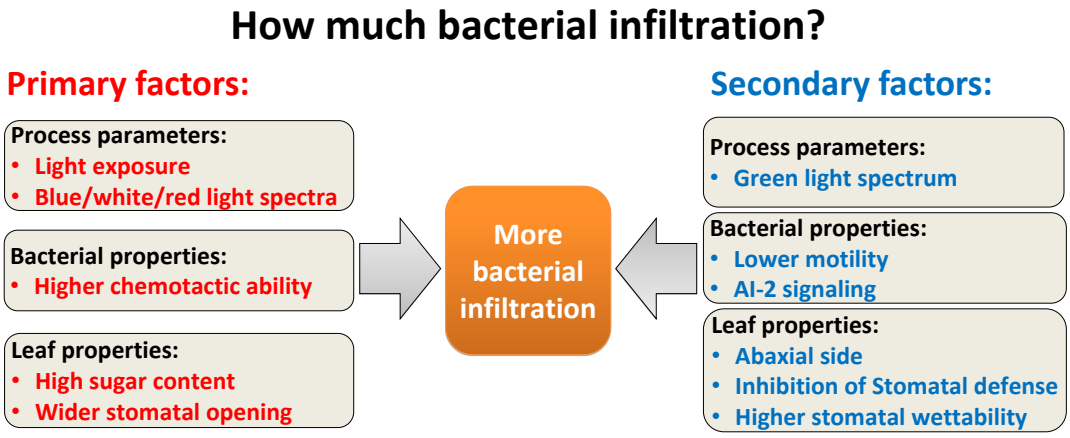

Figure 3.26: Primary and secondary factors leading to light-driven bacterial infiltration into plant leaves.

the stomatal wettability (more hydrophobic stomatal walls) decreased the infiltration for about 2%. This shows that the hydrophobic nature of the stomatal guard cells plays a defensive role in front of bacterial invasion.

3.5.4 Big picture: factors affecting infiltration

Based on the results presented above, the primary and secondary factors affecting the amount of infiltration into the leaf tissue are summarized in Fig. 3.26. It captures the overall understanding developed using the model and experiments in this study as well as experimental evidences reported in literature. Primary factors leading to more bacterial infiltration include the presence of blue/white/red light and photosynthesis, higher initial sugar content due to pre-exposure to light, high chemotactic ability of bacteria, and wider stomatal size. The secondary factors include presence of green light exposure, leaf abaxial side, lower bacterial motility, higher stomatal wettability and AI-2 signaling.

3.6 Conclusions

A mechanistic model of light-driven infiltration of bacteria into stomatal opening of plant leaves was presented. The concentration of photosynthetic sugar (glucose/sucrose) in the apoplast of the leaf tissue was predicted reasonably accurate, as compared with the experimental literature data. Based on the model results and experimental findings, it was shown that presence of light with moderate intensity (100 μmol/m$^2 \cdot$ s) is sufficient to induce chemotactic invasion of bacteria toward photosynthetic products within the leaf tissue. Bacteria were abale to infiltrate the leaf tissue during dark condition, however, the mount of infiltration was significantly less than that in the light. Blue light induced the highest amount of infiltration, while the green light caused the lowest. Ability of bacteria to do taxis was a major factor in penetration. Chemotaxis toward sugars was much more significant than aerotaxis or chemotaxis toward AI-2. Higher motility caused a decrease in infiltration as it decreased the chance of bacteria in the leaf surface water film to reach the stomatal pore. A more hydrophobic wall of the stomatal guard cells decreased the infiltration. Plant stomatal defense induced by perception of microbe-associated molecular patterns (MAMPs) was shown to play a role in inhibition of bacterial invasions into the leaf apoplast.

Acknowledgments

This work was supported by Grant 2014-70003-22357 from the USDA National Institute of Food and Agriculture. The authors thank Gozde Gencer, the graduate student at Biological and Environmental Engieering department of Cornell University, for her efforts in providing bacterial strains used for microbiological experiments. The microscopy imaging was done in the Plant Cell Imaging Center (PCIC) at Boyce Thompson Institute (BTI) of Cornell University.

Appendix I

Derivation of transport equations for CO_2 and O_2:

Transport of species, i, (*i.e.*, CO_2 and O_2) in the gas and water phases are governed by:

$$S_g \phi \frac{\partial c_{i,g}}{\partial t} = \nabla \cdot (S_g \phi D_{i,g} \nabla c_{i,g)} \tag{3.41}$$

$$(S_{wf} + S_{wb}) \phi \frac{\partial c_{i,w}}{\partial t} = \nabla \cdot \left((S_{wf} + S_{wb}) \phi D_{i,w} \nabla c_{i,w} \right) + (S_{wf} + S_{wb}) \phi R_{i,w} \tag{3.42}$$

where $R_{i,w}$ is an arbitrary source term (mol/m$^3 \cdot$ s). Assuming the equilibrium between gas and water phases to be described by Henry's law (Ho et al., 2006):

$$c_{i,w} = RTK_{H,i} c_{i,g} \tag{3.43}$$

and plugging in Eq. (3.4), the total concentration of each species in the REV is defined as:

$$c_i = \left(S_g + (S_{wf} + S_{wb}) RTK_{H,i} \right) \phi c_{i,g} \tag{3.44}$$

Using Eq. (3.44), the Eq. (3.42) can be rewritten as:

$$\begin{aligned} \left(S_g + (S_{wf} + S_{wb}) RTK_{H,i} \right) \phi \frac{\partial c_{i,g}}{\partial t} = \nabla \cdot \Big(& (S_g D_{i,g} + (S_{wf} + S_{wb}) D_{i,w} RTK_{H,i}) \phi \nabla c_{i,g} \Big) \\ & + (S_{wf} + S_{wb}) \phi R_{i,w} \end{aligned} \tag{3.45}$$

Finally, by adding Eq.(3.41) and Eq. (3.45) and applying Eq.(3.44), the combined transport equation in the REV is obtained as:

$$\frac{\partial c_i}{\partial t} = \nabla \cdot \left(D_{i,eff} \nabla c_i \right) + (S_{wf} + S_{wb}) \phi R_{i,w} \tag{3.46}$$

where $D_{i,eff}$ is effective diffusivity of species i in the porous media:

$$D_{i,eff} = \frac{S_g D_{i,g} + (S_{wf} + S_{wb}) D_{i,w} RTK_{H,i}}{S_g + (S_{wf} + S_{wb}) RTK_{H,i}} \tag{3.47}$$

BIBLIOGRAPHY

[1] Allakhverdiev, S.I., Yruela, I., Picorel, R. & Klimov, V.V. (1997). Bicarbonate is an essential constituent of the water-oxidizing complex of photosystem II. Proc. Natl. Acad. Sci. USA 94, 5050-5054.

[2] Ayre, B.G. & Turgeon, R. (2018). Export of Photosynthates from the Leaf. In Adams III, W.W., Terashima, I. (Eds.). The Leaf: A Platform for Performing Photosynthesis. Springer, Switzerland.

[3] Babic, I., Watada, A.E. Microbial populations of fresh-cut spinach leaves affected by controlled atmospheres. Postharvest Biology and Technology 9, 187-193.

[4] Bhattacharjee, T. & Datta, S.S. (2019). Bacterial hopping and trapping in porous media. Nature Communications 10, 2075.

[5] Braatsch, S. & Klug, G. (2004). Blue light perception in bacteria. Photosynthetic Research 79, 45-57.

[6] Bren, A., Hart, Y., Dekel, E., Koster, D., Alon, U. 2013. The last generation of bacterial growth in limiting nutrient. BMC Systems Biology 7, 27.

[7] Buckley T.N., Farquhar G.D.,2004. A new analytical model for whole-leaf potential electron transport rate. Plant, Cell and Environment 27, 1487-1502.

[8] Campbell, N.A., Reece, J.B., Urry, L.A., Cain, M.L., Wasserman, S.A., Minorsky, P.V., Jackson, R.B. 2008. Biology. 8th Ed. Pearson Custom Publishing, San Francisco, CA.

[9] Carruthers, A. 1990. Facilitated Diffusion of Glucose. Physiological Reviews 70(4), 1135-1176.

[10] Chen, L.Q. (2014). SWEET sugar transporters for phloem transport and pathogen nutrition. New Physiologists 201, 1150-1155.

[11] Chen, L.Q., Hou, B.H., Lalonde, S., Takanaga, H., Hartung, M.L., Qu, X.Q., Guo, W.J., Kim, J.G., Underwood, W., Chaudhuri, B., Chermak, D., Antony, G., White, F.F., Somerville, S.C., Mudgett, M.B., Frommer, W.B. 2010. Sugar transporters for intercellular exchange and nutrition of pathogens. Nature 468, 527-534.

[12] Chen, L.Q., Qu, X.Q., Hou, B.H., Sosso, D., Osorio, S., Fernie, A.R. & Frommer, W.B. (2012). Sucrose efflux mediated by SWEET proteins as a key step for phloem transport. Science 335, 207-211.

[13] Curk, T., Marenduzzo, D. & Dobnikar, J. (2013). Chemotactic Sensing towards Ambient and Secreted Attractant Drives Collective Behaviour of E. coli. PLoS ONE 8(10): e74878.

[14] Deng, D. & Yan, N. (2016). GLUT, SGLT, and SWEET: Structural and mechanistic investigations of the glucose transporters. Protein Science 25, 546-558.

[15] Doidy, J., Grace, E., Kuhn, Ch., Simon-Plas, F., Casieri, L. & Wipf, D. (2012). Sugar transporters in plants and in their interactions with fungi. Trends in Plant Science 17 (7), 413-422.

[16] Evans, J.R. (1995). Carbon Fixation Profiles do Reflect Light Absorption Profiles in Leaves. Aust. J. Plant Physiol.,22,865-73.

[17] Evans, J.R., Morgan, P.B. & von Caemmerer, S. (2017). Light quality affects chloroplast electron transport rates estimated from Chl fluoresce measurements. Plant and Cell Physiology 58(10), 1652-1660.

[18] Evans, J.R. & Vogelmann, T.C. (2003). Profiles of ^{14}C fixation through spinach leaves in relation to light absorption and photosynthetic capacity. Plant, Cell and Environment 26, 547-560.

[19] Farquhar, G.D., von Caemmerer, S. & Berry, J.A. (1980). A biochemical model of photosynthesis CO_2 assimilation in leaves of C_3 species. Planta 149, 78-90. 721-749.

[20] Ford, R. & Lauffenburger, D., (1991). Measurement of Bacterial Random Motility and Chemotaxis Coefficients: II. Application of Single-Cell-Based Mathematical Model. Biotechnology and Bioengineering 37, 661-672.

[21] Ford, R.M., Phillips, B.R., Quinn, J.A. & Lauffenburger, D.A. (1991). Measurement of Bacterial Random Motility and Chemotaxis Coefficients: I. Stopped-Flow Diffusion Chamber Assay.Biotechnology and Bioengineering 37(7), 647-660.

[22] Geers, C., Gros, G. 2000. Carbon dioxide transport and carbonic anhydrase in blood and muscle. Physiological Reviews 80(2), 681-715.

[23] Gorke B., Stulke, J. 2008. Carbon catabolite repression in bacteria: many ways to make the most out of nutrients. Nature Reviews Microbiology 6, 613-624.

[24] Golberg, D., Kroupitski, Y., Belausov, E., Pinto, R. & Sela, S. (2011). International Journal of Dood Microbiology 145, 250-257.

[25] Goryachev, A.B. (2011). Understanding Bacterial Cell-Cell Communication with Computational Modeling.Chem. Rev. 111, 238250.

[26] Harris, G.C., Cheesbrough, J.K. & Walker, D.A. (1983). Measurement of CO_2 and H_2O vapor exchange in spinach leaf discs. Plant Physiology 71, 102-107.

[27] Ho, Q.T., Berghuijs, H.N.C., Watt, R., Verboven, P., Herremans, E., Yin, X., Retta, M.A, Aernouts, B., Saeys, W., Helfen, L., Farquhar, G.D., Struik, P.C. & Nicola, B.M. (2016). Three-dimensional microscale modelling of CO_2 transport and light propagation in tomato leaves enlightens photosynthesis. Plant, Cell and Environment 39, 50-61.

[28] Ho, Q.T., Verlinden, B.E., Verboven, P., Vandewalle, S. & Nicolai, B.M. (2006). A permeation-diffusion-reaction model of gas transport in cellular tissue of plant materials. Journal of Experimental Botany 57(15), 4215-4224.

[29] Jani, S., Seely, A.L., Peabody V, G.L., Jayaraman, A., Manson, M.D. 2017. Chemotaxis to self-generated AI-2 promotes biofilm formation in Escherichia coli. Microbiology 136, 1778-1790.

[30] Jolly, W.L. 1985. Modern Inorganic Chemistry. McGraw-Hill, New York, NY., USA.

[31] Kana, T.M. & Miller, J.H. (1976). Effect of Colored Light on Stomatal Opening Rates of *Vicia faba* L. Plant Physiology 59, 181-183.

[32] Kayser, A., Weber, J., Hecht, V., Rinas, U. 2005. Metabolic flux analysis of Escherichia coli in glucose-limited continuous culture. i. growth-rate-dependent metabolic efficiency at steady state. Microbiology 151(3), 693-706.

[33] Kovarova, K., Zehder, A.J.B., Egli, T. 1996. Temperature-Dependent Growth Kinetics of Escherichia coli ML 30 in Glucose-Limited Continuous Culture. Journal Of Bacteriology 187(15), 4530-4539.

[34] Kroupitski,Y.,Golberg, D.,Belausov, E.,Pinto, R.,Swartzberg, D., Granot, D. & Sela, Sh. (2009). Internalization of Salmonella enterica in Leaves Is Induced by Light and Involves Chemotaxis and Penetration through Open Stomata. Applied and Environmental Microbiology, 6076-6086.

[35] Laganenka, L., Colin, R., Sourjik, V. 2016. Chemotaxis towards autoinducer 2 mediates autoaggregation in Escherichia coli. Nature Communications 7, 12984.

[36] Laisk, A., Eichelmann, H. & Oja, V. (2006). C_3 photosynthesis in silico. Photosynthesis Research 90, 4566.

[37] Lee, J.H. & Lee, J. (2010). Indole as an intercellular signal in microbial communities. FEMS Microbiology Reviews 34, 426-444.

[38] Li, J., Wang, L., Hashimoto, Y., Tsao, Ch.Y., Wood, Th.K., Valdes, J.J., Zafiriou, E.

& Bentley, W.E. (2006). A stochastic model of Escherichia coli AI-2 quorum signal circuit reveals alternative synthesis pathways. Molecular Systems Biology, 67.

[39] Lide, D.R. 1999. In: Handbook of Chemistry and Physics. Boca Raton, CRC Press.

[40] Long, Zh., Quaife, B., Salman, H., Oltvai, Z.N. 2017. Cell-cell communication enhances bacterial chemotaxis toward external attractants. Scientific reports 7, 12855.

[41] Lurie, S. (1978). The Effect of Wavelength of Light on Stomatal Opening. Planta 140, 245-249.

[42] Luo, Y., Zhang, T., Wu, H. 2014. The transport and mediation mechanisms of the common sugars in Escherichia coli. Biotechnology Advances 32, 905-919.

[43] Mannik, J., Driessen, R., Galajda, P., Keymer, J.E. & Dekker, C. (2009). Bacterial growth and motility in sub-micron constrictions. PNAS 106(35), 14861-14866.

[44] McAdams, H.H., Srinivasan, B., Arkin, A.P. 2004. The evolution of genetic regulatory systems in bacteria. Nature Reviews Genetics 5, 169-178.

[45] McDaniel, L.E., Bailey, E.G., Zimmerli, A. 1965. Effect of oxygen supply rates on growth of Escherichia coli, I. Studies in unbaffled and baffled shake flasks. Applied Microbiology 13(1), 109-114.

[46] Medlyn B.E., Dreyer E., Ellsworth D., et al. 2002. Temperature response of parameters of a biochemically based model of photosynthesis. II. A review of experimental data. Plant, Cell and Environment 25, 11671179.

[47] Melotto, M., Panchal, S. & Roy, D. (2014). Plant innate immunity against human bacterial pathogens. Frontiers in Microbiology 5, 411.

[48] Melotto, M., Underwood, W., Koczan, J., Nomura, K. & He, S.Y. (2006). Plant stomata function in innate immunity against bacterial invasion. Cell 126, 969-980.

[49] Monod J. 1949. The growth of bacterial culture. Annual Reviews in Microbiology 3, 371-394.

[50] Natarajan, A. & Srienc, F. (1999). Dynamics of Glucose Uptake by Single Escherichia coli Cells. Metabolic Engineering 1, 320-333.

[51] Nishio, J.N., Sun, J. & Vogelmann, T.C. (1993). Carbon fixation gradients across spinach leaves do not follow internal light gradients.The Plant Cell 5, 953-961.

[52] Nobel, P.S. (2005) Physicochenichal And Environmental Plant Physiology. 3rd Ed. Burlington, MA: Elsevier Academic Press.

[53] Nonomura, Y., Tanaka, T. & Mayama, H. (2016). Penetration behavior of a water droplet into a cylindrical hydrophobic pore. Langmuir 32, 6328-6334.

[54] Olaimat, A.N. & Holley, R.A. (2012). Factors influencing the microbial safety of fresh produce: A review. Food Microbiology 32(1), 1-19.

[55] Panarese, V., Herremans, E., Cantre, D., Demir, E., Vicente, A., Galindo, F.G., Nicolai, B. & Verboven, P. (2016). X-ray microtomography provides new insights into vacuum impregnation of spinach leaves. Journal of Food Engineering 188, 50-57.

[56] Panchal, S., Chitrakar, R., Thompson, B.K., Obulareddy, N., Roy, D., Hambright, W.S. & Melotto, M. (2016). Regulation of stomatal defense by air relative humidity. Plant Physiology 172, 2021-2032.

[57] Panchal, S. & Melotto, M. (2017). Stomate-based defense and environmental cues. Plant Signaling and Behavior 12(9), e1362517.

[58] Peterson, C.N., Mandel, M.J., Silhavy, Th.J. 2005. Escherichia coli Starvation Diets: Essential Nutrients Weigh in Distinctly. Journal of Biotechnology 187(22), 7549-7553.

[59] Plawsky,J.L. (2010). Transport Phenomena Fundamentals. CRC Press, Boca Raton, FL.

[60] Rahman, M.Sh. (2005). Mass-Volume-Area-Related Properties of Foods. In, Rao, M.A., Rizvi, S.S.H., Datta, A.K. (Eds). Engineering Properties of Foods. 3rd Ed. CRC Press, Boca Raton, FL.

[61] Ranjbaran, M. & Datta, A.K. (2019). Pressure-driven infiltration of water and bacteria into plant leaves during vacuum cooling: A mechanistic model. Journal of Food Engineering 246, 209-223.

[62] Reitzer, L. 2003. Nitrogen assimilation and global regulation in Escherichia coli. Annu Rev Microbiol. 57,155-176.

[63] Rennie, E. A., Turgeon, R. 2009. A comprehensive picture of phloem loading strategies. PNAS 106(33), 14162-14167.

[64] Shiloach, J., Fass, R. 2005. Growing E. coli to high cell density historical perspective on method development. Biotechnology advances 23(5), 345-357.

[65] Shimazaki, K.I., Doi, M., Assmann, S.M. & Kinoshita, T. (2007). Light regulation of stomatal movement. Annual Review of Plant Biology 58, 219-247.

[66] Stolper, D.A., Revsbech, N.P., Canfield, D.E. 2010.Aerobic growth at nanomolar oxygen concentrations. PNAS 107(44), 18755-18760.

[67] Stewart, P.S. 2003. Diffusion in Biofilms. Journal of Biotechnology 185(5), 1485-1491.

[68] Taylor, B.L. & Koshland, JR, D.E. (1975). Intrinsic and Extrinsic Light Responses of Salmonella typhimurium and Escherichia coli. Journal of Biotechnology 123(2), 557-569.

[69] Tindall, M.J., Maini, P.K., Porter, S.L. & Armitage, J.P. (2008). Overview of Mathematical Approaches Used to Model Bacterial Chemotaxis II: Bacterial Populations. Bulletin of Mathematical Biology 70: 15701607.

[70] Turner, N.C. & Graniti, A. (1969). Fusicoccin: a fungal toxin that opens stomata. Nature 223, 1070-1071.

[71] Vargas, W.A., Salerno, G.L. 2010. The Cinderella story of sucrose hydrolysis: alkaline/neutral invertases, from cyanobacteria to unforeseen roles in plant cytosol and organelles. Plant Science 178, 1-8.

[72] Verboven, P., Herremans, E., Helfen, L., Ho, Q.T., Abera, M., Baumach, T., Wevers, M. & Nicolai, B.M. (2015). Synchrotron X-ray computed laminography of the threedimensional anatomy of tomato leaves. The Plant Journal 81, 169-182.

[73] Vogelmann, T.C. & Evans, J.R. (2002). Profiles of light absorption and chlorophyll within spinach leaves from chlorophyll fluorescence. Plant, Cell and Environment 25, 1313-1323.

[74] Voitsekhovskaja, O.V., Pakhomova, M.V., Syutkina, A.V., Gamalei, Y.V. & Heber, U. (2000). Compartmentation of assimilate fluxes in leaves. II. Apoplastic sugar levels in leaves of plants with different companion cell types. Plant Biology 2, 107-112.

[75] Wang, L., Hashimoto, Y., Tsao, Ch.Y., Valdes, J.J. & Bentley, W.E. (2005). Cyclic AMP (cAMP) and cAMP Receptor Protein Influence both Synthesis and Uptake of Extracellular Autoinducer 2 in Escherichia coli. Journal of Biotechnology 187(6), 2066-2076.

[76] Warning, A. & Datta, A.K. (2017). Mechanistic understanding of non-spherical bacterial attachment and deposition on plant surface structures. Chemical Engineering Science 160(16), 396-418.

[77] Winter, H.,Robinson, D.G., Heldt, H.W. 1994. Subcellular volumes and metabolite concentrations in spinach leaves. Planta 193, 530-535.

[78] Wrigth, S., Walia, B., Parkinson, J.S. & Khan, S. Differential activation of Escherichia coli chemoreceptors by blue-light stimuli. Journal of Bacteriology, 3962-3971.

[79] Wu, M., Roberts, J.W., Kim, S., Koch, D.L., DeLisa, M.P. Collective Bacterial Dynamics Revealed Using a Three-Dimensional Population-Scale Defocused Particle Tracking Technique. Applied and Environmental Microbiology 72(7), 4987-4994.

[80] Xavier, K.B. & Bassler, B.L. (2005). Regulation of uptake and processing of the quorum-sensing autoinducer AI-2 in Escherichia coli. Journal of Biotechnology 187(1), 238-248.

[81] Xu, F., Song, X., Cai, P., Sheng, G. & Yu, H. (2017). Quantitative determination of AI-2 quorum-sensing signal of bacteria using high performance liquid chromatographytandem mass spectrometry. Journal of Environmental Sciences 52, 204-209.

[82] Yamori, W., Noguchi, K., Kashino, Y., Terashima, I. 2008. The role of electron transport in determining the temperature dependence of the photosynthetic rate in spinach leaves grown at contrasting temperatures. Plant Cell Physiol 49,583-591.

[83] Yin, X. & Struik, P.C. (2009). C_3 and C_4 photosynthesis models: An overview from the perspective of crop modelling. NJAS-Wageningen Journal of Life Sciences 57, 27-38.

[84] Zhu, X.G., Wang, Y., Ort, D.R. & Long, S.P. (2013). e-photosynthesis: a comprehensive dynamic mechanistic model of C3 photosynthesis: from light capture to sucrose synthesis. Plant, Cell and Environment 36, 1711-1727.

[85] Zohar, B.A., Kolodkin-Gal, I. 2015. Quorum Sensing in Escheichia coli: Interkingdom, Inter- and Intraspecies Dialogues, and a Suicide-Inducing Peptide. In, Kalia, V.C. (Ed.), Quorum Sensing vs Quorum Quenching: A Battle with No End in Sight. Springer. India.

CHAPTER 4

RETENTION AND INFILTRATION OF BACTERIA ON A PLANT LEAF DRIVEN BY SURFACE WATER EVAPORATION

4.1 Abstract

Evaporation-driven internal flows within a sessile droplet can transport microorganisms close to the leaf surface and facilitate their infiltration into the available openings, such as stomata. Here, using microfabricated surfaces out of Polydimethylsiloxane (PDMS), the sole effects of evaporation of sessile droplets in contamination of plant leaves was studied. These surfaces were patterned with stomata, trichomes and grooves that are common surface microstructures on plant leaves. Evaporation of sessile droplets, containing bacterial suspensions, on real leaves and fabricated surfaces were studied using confocal microscopy. To provide insight about the effects of leaf hydrophobicity and surface roughness on the bacterial retention and infiltration, variations of contact angle of sessile droplets at these surfaces were measured during evaporation. The results showed that evaporation-driven flow transported bacteria close to the surface of spinach leaves and fabricated surfaces, leading to distinct infiltration into the microstructures. Larger size and wider spacing of the micropores, and a more hydrophillic surface led bacteria to spread more at the droplet base area and infiltrate into more stomata. Evaporation-driven movement of contact line, that can sweep bacteria over the leaf surface, was shown to lead to bacterial infiltration into the stomatal pores. Findings should help improve microbial safety of leafy greens.

4.2 Introduction

Evaporation is a fundamental process that can happen at various stages of pre-harvest and post-harvest processing of leafy greens. Within an evaporating sessile droplet (i.e., a droplet that attached to a substrate) on a leaf surface, internal flows toward the contact line occur to compensate the high evaporation fluxes at the contact line region (Deegan et al., 1997; Hu and Larson, 2005a,b). These flows can carry bacteria, if present, toward the leaf surface and at the location of contact lines (Kasyap et al., 2014) and facilitate their access to the leaf interior.

Bacterial transport within an evaporating sessile droplet on a leaf surface can be due to several active and passive driving forces: 1) convective transport by the fluid flow (Deegan et al., 2000), 2) diffusive transport due to Brownian motion, that is as a result of continuous bombardment from molecules of the surrounding fluid, 3) tactic motions or active swimming toward nutrient sources (Thokchom et al., 2014), and 4) motile motions or the random runs and tumblings. Among these mechanisms, only the first one is purely induced by evaporation and can be a combination of capillary effects (driven by the surface tension of the liquid), thermo-capillary effects (driven by the gradient of the surface tension of the liquid at the liquid-gas interface), and flow due to the movement of the contact line (Snoeijer and Andreotti, 2013).

A leaf surface is a complex environment which includes several microstructures such as trichomes, stomata and grooves that can be attractive for bacteria (Kroupitski et al., 2009). In addition to the availability photosynthetic nutrients at the location of these microstructures (for example, stomata do photosynthesis), they also serve as shelters for bacteria to avoid harsh environments and settle them at the leaf surface. As bacteria get hidden at the location of these microstructures, they cannot easily be washed away following typical sanitation practices, thus presenting a risk to the consumer. Since evaporation of water films and sessile droplets on plant leaf surfaces is a process that frequently happens as leafy greens move from field to fork, its role on the microbial

contamination of the leafy greens needs to be better understood. Literature is scant on the specific effect of evaporation on bacterial retention at the leaf surface and their infiltration into leaf openings. This study intends to contribute to underling mechanisms of this evaporation-driven retention and infiltration process. Due to the complexities of a leaf surface in terms of its hydrophobicity and roughness, artificial patterned surfaces fabricated out of Polydimethylsiloxane (PDMS) are used here in conjunction with real leaves.

4.2.1 Objectives

The objectives of this work were:

- Design and fabrication of leaf surface surrogates out of PDMS patterned with three different common microstructures of stomata, trichomes and grooves that are normally found on plant leaves.
- To investigate how evaporation-driven flows, within a sessile droplet located on real leaves as well as fabricated patterned surfaces, lead to bacterial access to the surface microstructures.
- To investigate of the role of size and spacing of microstructures, and hydrophobicity of the surface, and bacterial concentration on bacterial deposition patterns.
- To investigate how evaporation-driven movements of contact lines leads to bacterial infiltration into stomatal opening.

4.3 Materials and Methods

The experimental approach taken here includes fabrication and characterization of patterned PDMS surfaces, measurement of contact angles of sessile droplets on real

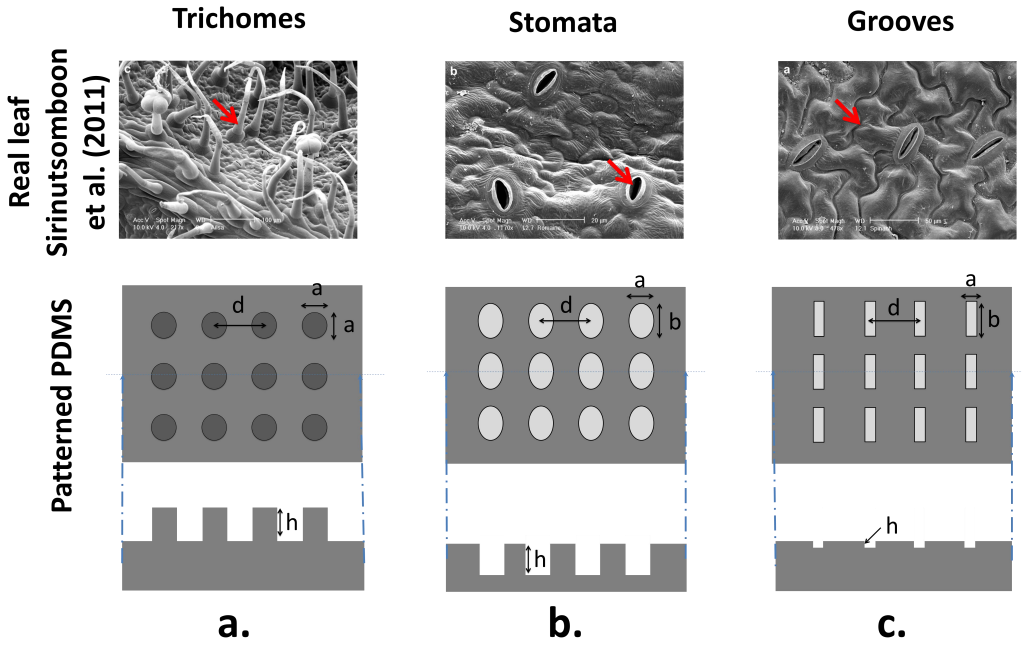

Figure 4.1: Microscopic images of three types of the microstructures at the surface of plant leaves, adapted from Sirinutsomboon et al. (2011), and their artificial surrogate patterns on PDMS. Dimensions a, b, d and h are shown in Table 4.1.

leaves and the PDMS surfaces, and microscopy imaging of drop (containing fluorescent bacteria/micro-particles) evaporation on real leaves and the PDMS surfaces. Details of these experiments are discussed here.

4.3.1 Fabrication of micropatterned surfaces

The three common micro-structures on the plant leaf surfaces were molded on the PDMS surfaces (Fig 5.4). These micro-structures include trichomes, stomata and grooves whose dimensions were chosen based on the available microscopic imaging data (Sirinutsomboon et al., 2011). For each micro-structure, two different sizes and spacing were fabricated. The PDMS surfaces were made in two different hydrophobicity levels within a range that many leafy vegetables sit (40° to 130°) (Lazouskaya et al.,

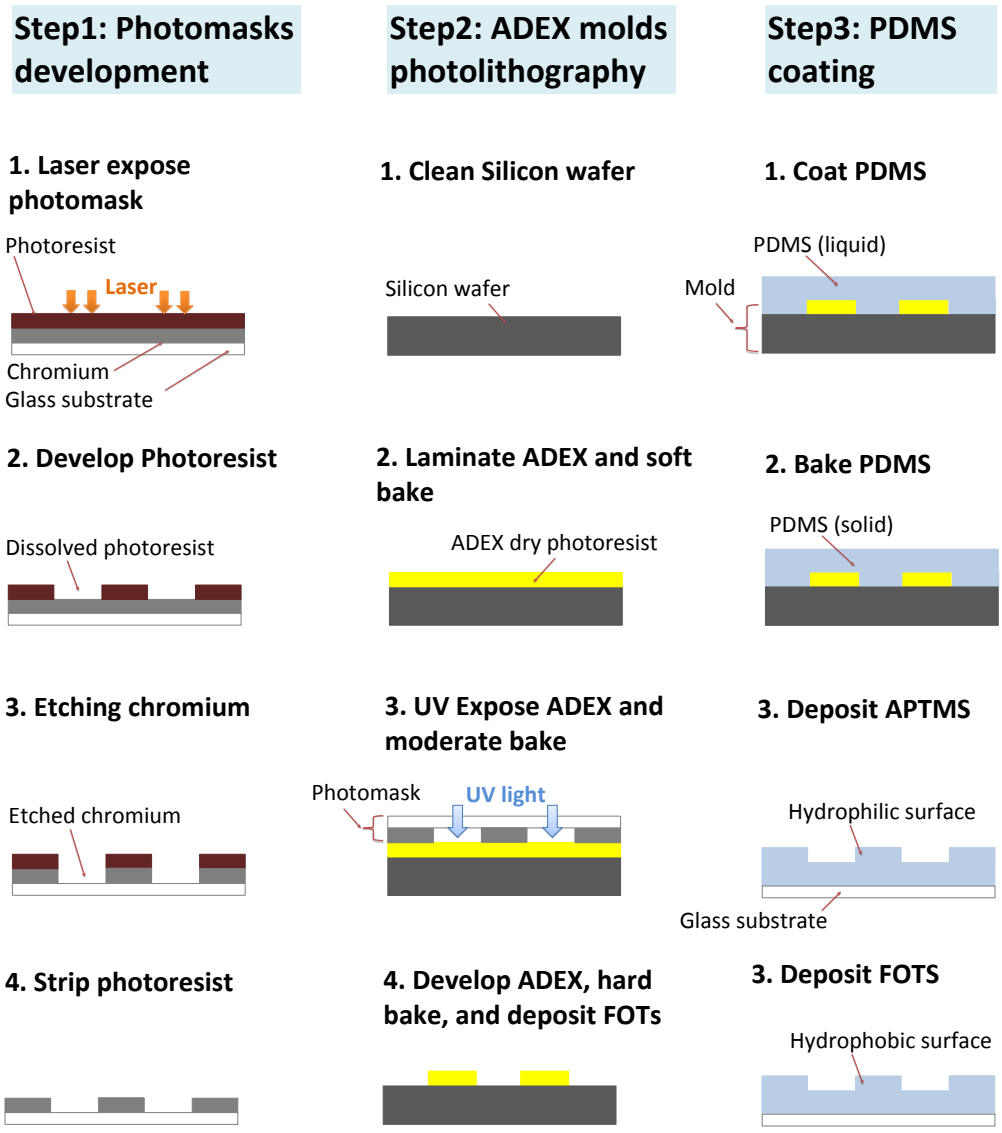

Figure 4.2: Fabrication steps taken during photomask development, ADEX molds fabrications and PDMS coating.

2016).

Typical fabrication steps are shown in Fig 4.2. In step 1, photomasks were prepared for the each type of micro-structures.The patterns, shown in Fig 4.1, were designed in L-Edit 15 (Mentor Graphics Corporation, OR, USA), and the CAD files (.gds format) were transferred to a Heidelberg mask writer (DWL2000, Heidelberg Instruments, Germany) to write the 5-inch chromium photomasks. After laser exposure, each photomask was developed and etched to remove the exposed layer of photoresist and uncovered chromium, respectively. Followed by a photoresist stripping, the masks were thoroughly rinsed and dried.

In step 2, the molds required to pattern PDMS were made using photolithography technique. ADEX sheets, dry-state negative photoresists, of various thicknesses were purchased from Integrated Micro Materials TM (TX, USA). The sheets were laminated on clean n-type one-sided silicon wafers of 100 mm diameter, using an ADEX hot-roll laminator (SKY-335R6, SKY-DSB Ltd., Korea) at roller velocity and temperature of 0.3 m/min and 65 $^{\circ}$C , respectively. Immediately after lamination, the wafers were baked at 65 $^{\circ}$C for 30 min. Then, by using the photomasks fabricated in the previous step, the wafers were exposed to i-line UV light by a contact aligner (ABM Inc., CA, USA) equipped with a short wavelength exclusion filter. The exposure dose for the ADEX sheets of 5 μm and 20 μm thickness were 90 mJ/cm^2 and 175 mJ/cm^2, respectively. This was followed by a post-exposure bake at 85 $^{\circ}$C for 10 min. The developing time for the ADEX sheets of 5 μm and 20 μm thickness were 5 min and 15 min, respectively, by using SU-8 developer. The developed devices were hard baked at 150 $^{\circ}$C for 60 min. In order to avoid the PDMS stick to the ADEX, a molecular layer of FOTS (a coating to make the surface hydrophobic) was deposited on the ADEX surfaces using a molecular vapor deposition machine (MVD-100, MVD TM.)

In step 3, these ADEX devices were used as molds to pattern PDMS. PDMS (with a mass ratio of base to curing agent of 10:1) was vacuumed for 20 min to remove all

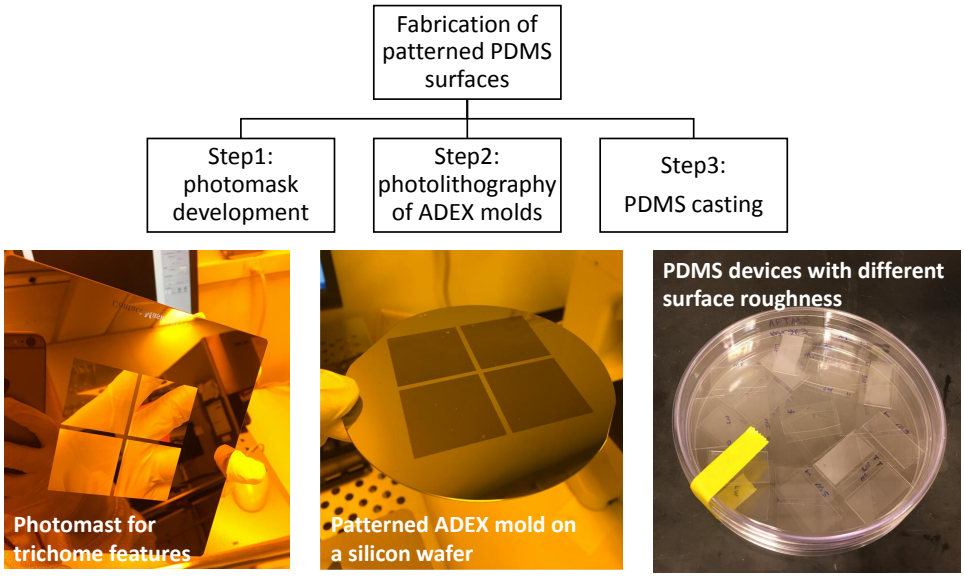

Figure 4.3: Fabricated photomask, ADEX mold, and PDMS surfaces patterned with trichomes of two different size and spacing. See Table 4.1 for the dimensions.

trapped air bubbles. It was then poured on the surface of the wafers and left at 65 °C for 120 min to solidify. The final patterned PDMS surfaces were placed on microscope cover-slips, after applying oxygen plasma on the attaching surfaces of the glass and PDMS to improve their stickiness. Hydrophobocity of the final PDMS device was adjusted by depositing a layer of FOTS (to make the surface hydrophobic)or APTMS (a coating to make the surface hydrophillic) using MVD-100 machine.

After fabrication of the PDMS devices, the size of the features were characterized by an optical microscope and an optical profilometer (NewView 7300, Zygo Corporation, CT, USA), as shown in Table 4.1.

Table 4.1: Dimensions of the micro-structures fabricated on the PDMS surfaces.

Definition	Microstructure dimension	Small features, size (μm)	Large features, size (μm)
Stomata			
Small diameter	a	16.0	25.7
Large diameter	b	27.6	29.5
Spacing	d	50 & 100	50 & 100
Depth	h	20	20
Trichomes			
Diameter	a	16.9	26.9
Spacing	d	50 & 100	50 & 100
Height	h	20	20
Grooves			
Width	a	2.8	5.2
Length	b	31.4	31.9
Spacing	d	50 & 100	50 & 100
Depth	h	20	20

4.3.2 Measurement of the contact angle

A contact angle goniomter (Rame-Hart 500, NJ, USA) was used do detect the variations of the contact angle of the droplet on various spinach leaves as well as the PDMS surfaces. For each experiment, a 1 μl droplet was placed on the surface and the variation of the contact angle was measured over evaporation time.

4.3.3 Drop evaporation experiments

To detect evaporation-driven bacterial collections on PDMS surfaces, a 1 μl drop of suspension of fluorescent *E. coli* RP437 cells (see supplementary for bacterial preparation procedure) was placed on each surface, and the evolution of the contact line region was sequentially imaged using an inverted confocal microscope (Olympus IX71, Olympus Corporation, Japan) (Kasyap et al., 2014). When needed, the same procedure was applied using 1 μm fluorescent tracer particles (Bangs Laboratories Inc., IN, USA) at a concentration of about 1×10^8 particles/ml. Drop evaporation and bacterial deposition experiments on real plant leaves was done using an upright confocal microscope (Leica TCS SP5, IL, USA). Both confocal microscopy experiments were performed at 10x magnification, and using a 488 nm argon laser.

4.4 Results and discussion

This section presents first the variations of the contact angle of a sessile droplet on real plant leaf and PDMS devices. Next, effects of presence of stomata, grooves and trichomes, their size and spacing, the hydrophobicity of the surface, and bacterial concentration on evaporation-driven retention and infiltration of plant leaves is discussed. Finally, the role of evaporation-driven movement of contact line in infiltration of bacteria into stomatal opening is elaborated.

4.4.1 Contact angle on a leaf and patterned surfaces during evaporation

Surface hydrophbicity of the plant leaves varies in a wide range. For instance, lettuce leaves are hydrophilic with an initial contact angle of less than 45°, while spinach leaves

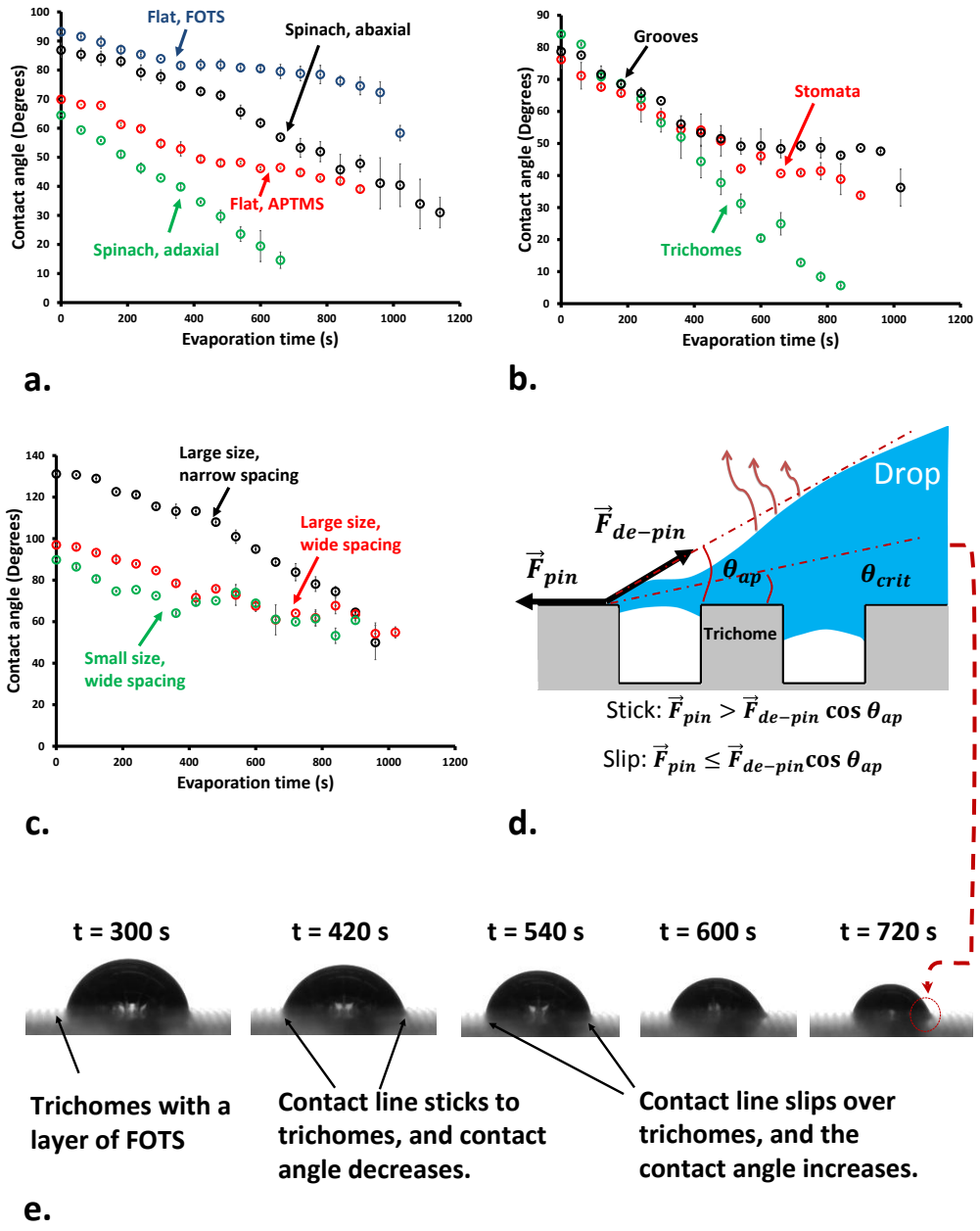

Figure 4.4: a) Variations of the contact angle on leaf and flat PDMS surfaces coated with FOTS (hydrophobic) and APTMS (hydrophillic). b) Variations of the contact angle on APTMS-deposited PDMS patterned with stomata, trichomes and grooves. c) Effect of size and spacing on the variation of the contact angle on FOTS-deposited PDMS surfaces patterned with trichomes. d) Schematic showing the underlying mechanisms of stick-slip behaviour of a contact line during evaporation. e) Images of an evaporating sessile droplet on a FOTS-deposited PDMS surfaces patterned with small trichomes with wide spacing.

are more hydrophobic, having a contact angle above 65° (Lazouskaya et al., 2016). Variation of the contact angle of sessile droplets during evaporation affects flow patterns within the droplet and thus transport of bacteria. Therefore, variation of the contact angle of sessile droplets on leaf and patterned surfaces are analyzed here. Figure 4.4a presents measured contact angle of 1 μl sessile droplets at the surfaces of spinach leaves and flat PDMS surfaces covered with FOTS or APTMS. In general, the contact angle decreases during evaporation times almost linearly on both leaf and fabricated surfaces. This is because the contact line often pined to the surface, and removal of mass from the droplet led to reduction in its contact angle. Abaxial side of spinach leaf is more hydrophobic than its adaxial surface (Lazouskaya et al., 2016). FOTS-deposited surfaces show closer surface characteristic to the abaxial side, while the APTMS-deposited surface better represents the adaxial side.

Addition of the microstructures to the flat surfaces of the same hydrophobicity makes some changes in the variation of contact angle during evaporation. For example, on APTMS-deposited PDMS patterned with trichomes, the contact angle decreased sharply during evaporation (Fig. 4.4b). This is because trichomes enhance pinning of the droplet to the surface, and therefore the contact angle decreases faster as the drop evaporates. On stomata and grooves, contact angle became somewhat constant after about 550 s which is due to the movement of the contact line over these microstructures. This constant contact angle trend that was also seen on a flat surface (Fig. 4.4a). On stomata, the contact line showed oscillations at these later times (Fig. 4.4b) due to a stick-slip behavior, which is explained later.

Spacing of the pattered features highly affected the contact line variation during evaporation (Fig. 4.4c). Wider spacing reduces the contact angle. The narrow spacing probably brings the drop closer to a Cassie state (*i.e.*, droplet sits on top of the microstructures without any contact with the surface) and causes a super hydrophobic behavior. When spacing stayed the same, contact angles were similar for two different sizes (Fig. 4.4c).

The oscillations seen in the contact angle on all three patterned surfaces after about 550 s of evaporation (Fig. 4.4b) is due to a stick-slip behavior of the contact line on the patterned surfaces (Chen et al., 2012, He et al., 2017). Figure 4.4d shows a schematic of the underlying mechanisms of the stick-slip behavior of contact line on a surface patterned with trichomes. Initially, the contact line is pinned to the surface of the features. As the droplet evaporates, surface tension forces cause the contact angle to decrease. This reduction in the contact angle continues until it reaches a critical value at which the de-pinning forces generated from the surface tension of the evaporating droplet exceed the pinning forces (Fig. 4.4d), leading to the slipping of the contact line over the feature. This behavior can be observed in Fig. 4.4e that shows the evaporation of a 1 μl sessile droplet on a FOTS-deposited PDMS surface patterned with trichomes of small size and wide spacing. The stick-slip behavior of the contact line, can contribute in the bacterial infiltration into the leaf opening, as discussed Section 4.4.3.

4.4.2 Evaporation-driven flows transport bacteria toward the leaf surface

Figure 4.5a shows a ring formed on a spinach leaf surface after evaporation of a 0.5 μl sesile droplet containing *E. coli* RP437 cells. When a sessile droplet containing bacteria evaporates on a leaf surface, it transports the bacterial cells close to the leaf surface and facilitates their access to the surface microstructures (Fig. 4.5b). Figure 4.5c and Fig. 4.5d confirm the bacterial accumulation at the location of the contact line and into the stomata and grooves after evaporation of the sessile droplet. These findings imply the effects of evaporation-driven internal flows, shown in Fig. 4.5b, in bacterial transport toward the contact line and close to the leaf surface. Similar patterns were also observed for 1 μm fluorescent beads (instead of bacteria) in a sessile droplet (Fig 4.5e), highlighting the dominant role of passive transport by evaporation-driven internal flows.

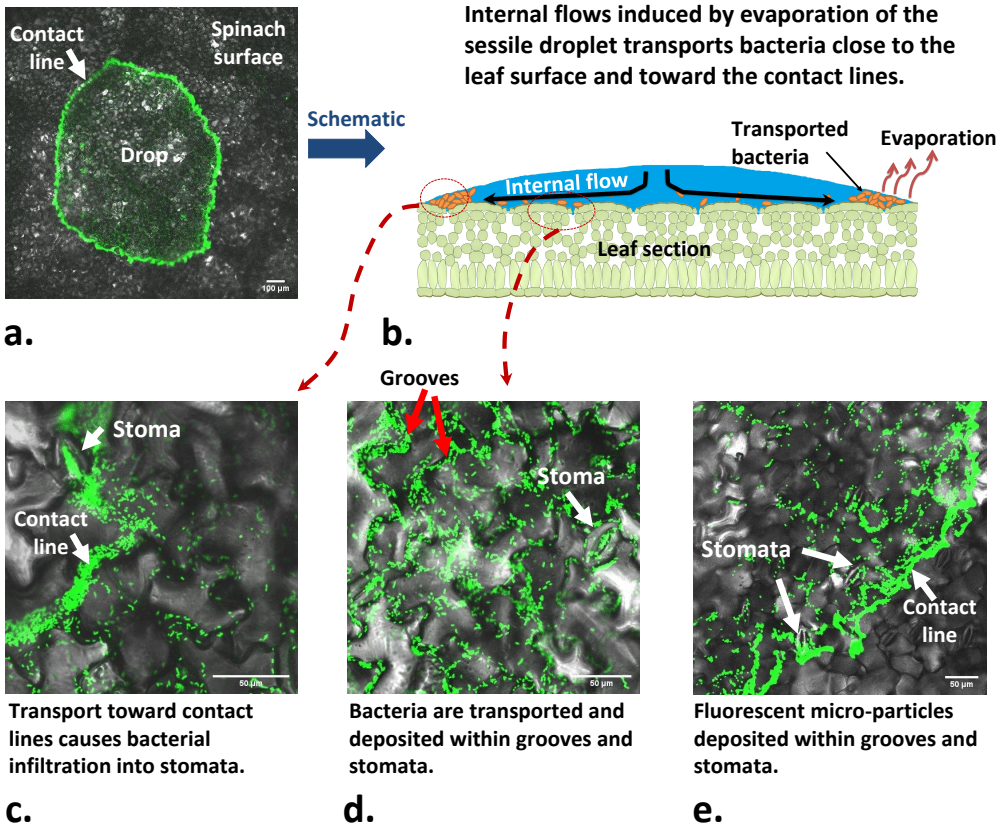

Figure 4.5: Confocal microscopy image (with 10x magnification) of deposition of *E. coli* RP437 on adaxial side of a spinach leaf after evaporation of a sessile droplet. b) A schematic of the mechanisms of transport of bacteria in the evaporating sessile droplet located at the leaf surface. c) A close look at the leaf surface, at the contact line region, showing bacterial collections at the contact line and a severe infiltration into a stomatal pore. d) A close look at the leaf surface, at a location inside the droplet and away from the contact line, showing bacterial deposition within grooves and stomata. e) Deposition of 1μm fluorescent micro-particles on an adaxial side of a spinach leaf, showing their accumulation within stomata and grooves.

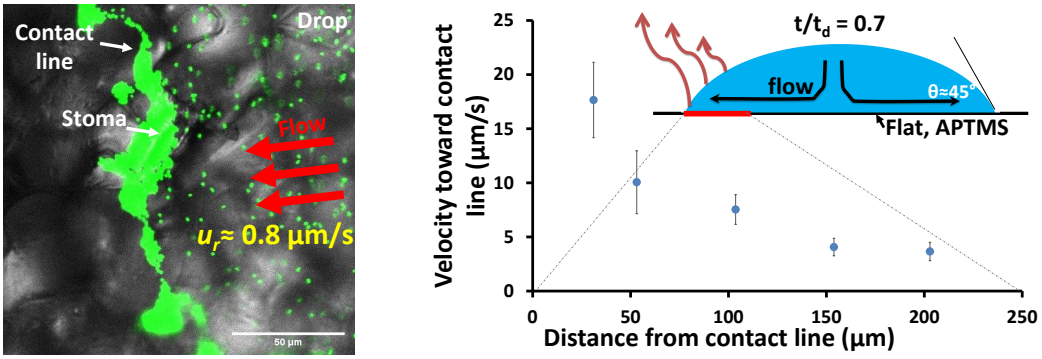

Figure 4.6: a) A close look at the transport of 1μm fluorescent micro-particles toward contact line of a sessile droplet located at adaxial side of a spinach leaf. b) Distribution of the velocity of fluorescent micro-particles as a function of distance from the contact line of an evaporating sessile droplet located on an APTMS-deposited flat PDMS suface. Data are collected after about 650 s of evaporation, when the contact angle was about 45°

.

Figure 4.6a shows flow of fluorescent beads toward contact line of an evaporating sessile droplet on spinach leaf. To provide a quantitative understanding of the amount and distribution of fluid velocity within the droplet, velocity of fluorescent beads within an evaporating droplet on a flat APTMS-deposited surface was measured from confocal microscopy data (Fig. 4.6b). The velocity of microbeads increases as they approach the contact lines. This is because the evaporation flux is stronger at the contact line region (Starov and Sefiane, 2009; Son, 2010), leading to the acceleration of particles. The same patterns and orders of magnitude were observed by Kasyap et al. (2014), Monteux and Lequeux (2011), and predicted by analytical models derived from the lubrication theory (Hu and Larson, 2005). On a plant leaf, however, presence of microstructure can create instabilities in the fluid flow close to the leaf surface. This can generate upward flows away from microstructures that can reduce the radial flow velocity toward the contact line, compared with what is seen on a flat APTMS-coated PDMS substrate

(Fig. 4.6b). From confocal microscopy data (Fig. 4.6a), the radial velocity of microparticles toward contact line of a sessile droplet at a leaf surface was estimated to be less than 1 μm/s which is smaller than what is observed on a flat APTMS-coated PDMS surface (Fig. 4.6b). The smaller velocity on a leaf can lead to a more uniform distribution of microparticles/bacteria at the leaf surface.

Plant leaves being complex, the underlying mechanisms of contamination can be studied more effectively by using fabricated surfaces with known hydrophobicity and roughness. Figure 4.7 shows the variations in the concentration of *E. coli*RP437 (fluorescence intensity represents bacterial concentration), during evaporation of sessile droplets, initially containing 10^9 cells/ml on APTMS-deposited surfaces. On a flat surface (Fig. 4.7a), the highest concentration of bacteria is at the contact lines (the sharp line of the fluorescence intensity). In the presence of stomata (Fig. 4.7b), bacteria are also collected within the features. Stomatal pores located at the contact line region contain the highest concentration of bacteria after evaporation (see also Fig. 4.5c). Trichomes play the role of micropillars in front of internal flows that can trap bacteria. Figure 4.7c shows how bacterial cells are collected around trichomes during evaporation. At the contact line, more bacteria are collected around the trichomes which is due to the bacterial transport by evaporation-driven flows toward the contact line. Bacteria are also deposited within the grooves (Fig. 4.7d). Grooves located at the contact lines contained a much higher concentration of bacteria after evaporation, as is highlighted by the fluorescent intensity profile (see also Fig. 4.5c).

Stomata are the main natural routes for infiltration of bacteria into plant leaves. Effect of their size and spacing on the bacteria infiltration is shown in Fig. 4.8a to Fig. 4.8c. Stomatal density on the adaxial side of a leaf is lower than its abaxial side. Therefore, patterned surfaces with stomatal features of wide (Fig. 4.8a) and narrow (Fig. 4.8b) spacing can represent adaxial and abaxial sides of a leaf, respectively. An increase in the stomatal density led bacteria to mainly accumulate at the location of the contact line. An mentioned before, presence of stomata can create upward flows away from stom-

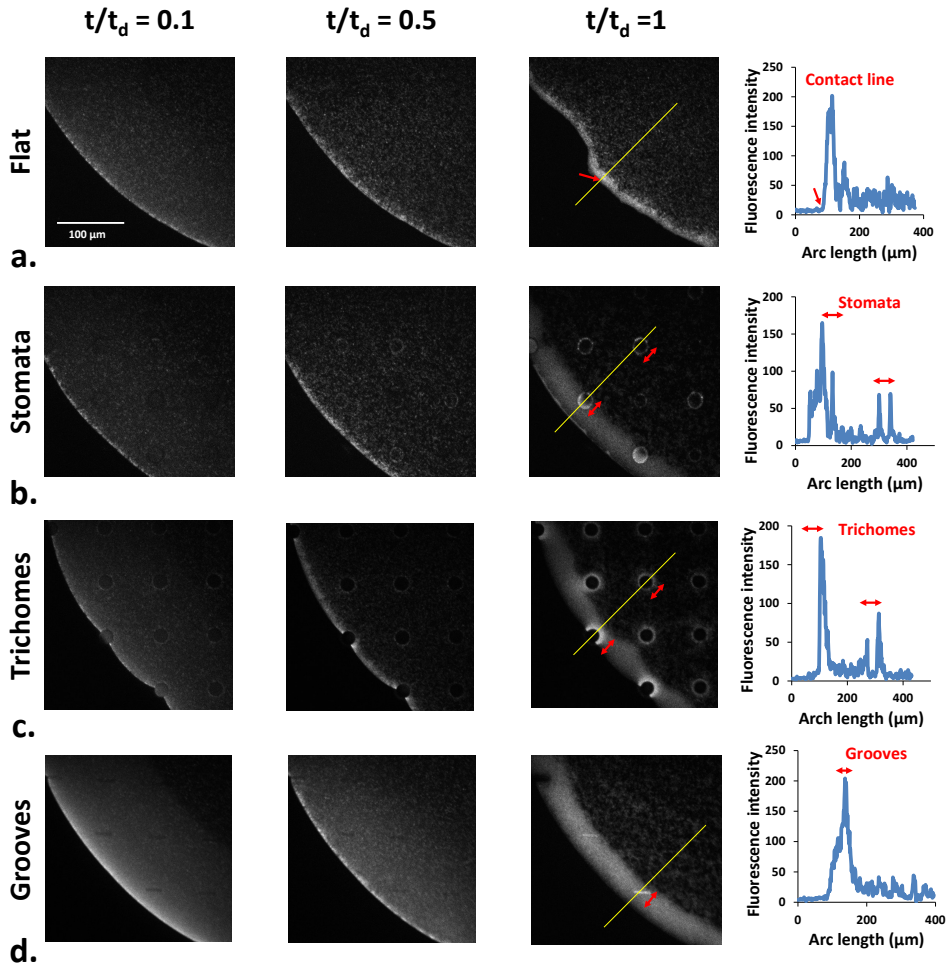

Figure 4.7: Collection of *E. coli* RP437 (fluorescence intensity represents bacterial concentration), with an initial concentration of 10^9 cells/ml, on APTMS-coated (hydrophillic) PDMS surfaces with a) no patterns (flat surface), and with b) stomatal, c) trichomes and d) grooves patterns. For all cases, a fluorescence intensity profile highlights the distributions of the bacterial concentration at $t/t_d = 1$ along a yellow line shown in each image. On a flat surface (a), bacterial concentration is higher at the contact line. In (b) and (d), the bright color inside the small ellipses and rectangles represents bacterial infiltration into stomata and grooves, respectively. In (c), the bright color around the circles, represents bacterial collection around the trichomes. The location of the contact line and the fabricated features are shown by red arrows. All patterned surfaces shown here contain large features with wide spacing. Here t_d is about 15 min.

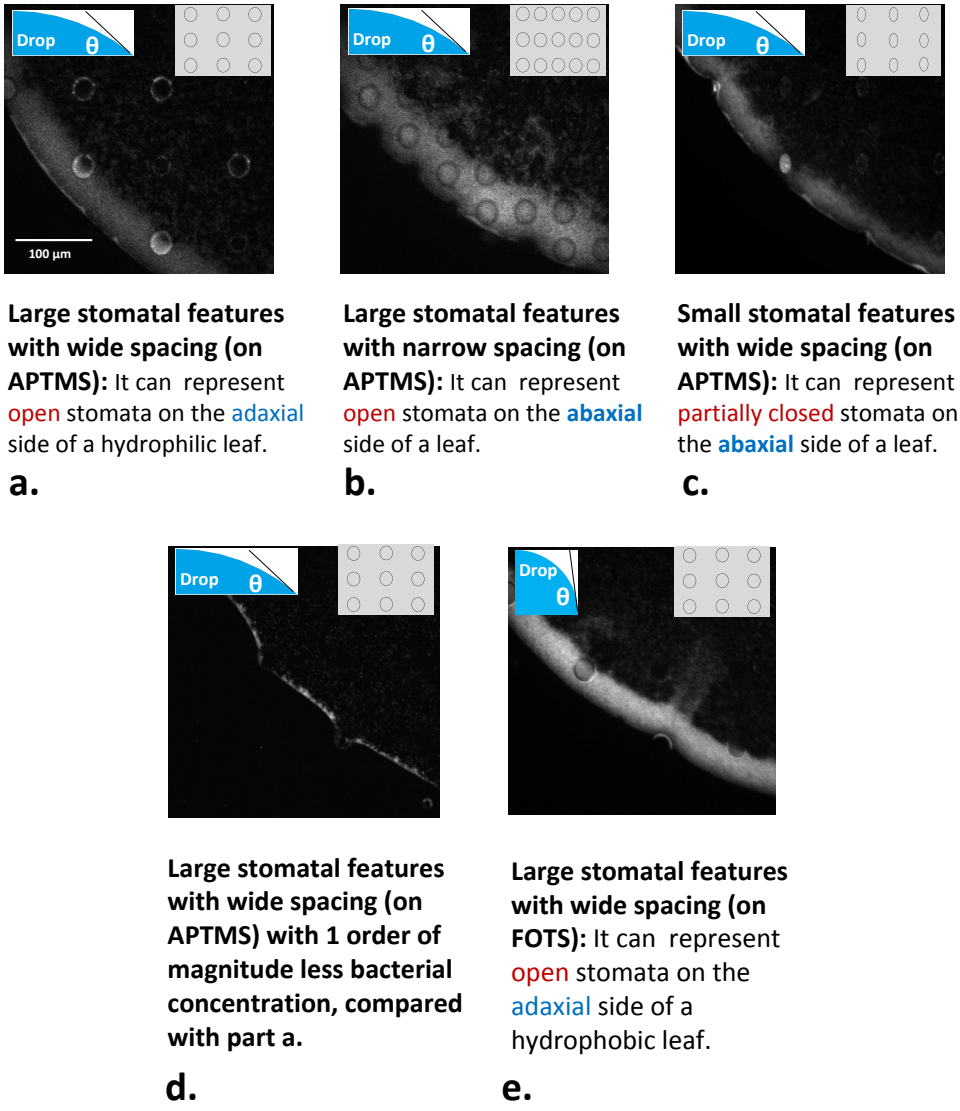

Figure 4.8: Collection of *E. coli* RP437 (fluorescence intensity represents bacterial concentration) with an initial concentration of 10^9 cells/ml, on APTMS-coated (hydrophillic) PDMS surfaces patterned with stomatal features with a) large size and wide spacing, b) large size and narrow spacing, and c) small size and narrow spacing. d) Bacterial collection (with an initial concentration of 10^8 cells/ml) on a APTMS-coated (hydrophillic) PDMS surface patterned with stomatal features with large size and wide spacing. e) Bacterial collection (with an initial concentration of 10^9 cells/ml) on a FOTS-coated (hydrophobic) PDMS surface patterned with stomatal features with large size and wide spacing. the bright color inside the small ellipses and rectangles represents bacterial infiltration into stomata.

atal pores that can transport unattached bacteria out of the pore. When the stomatal density increases, these flows get stronger. A combination of these upward flows and the evaporation-driven downward and radial flows close to the leaf surface leads bacteria to mainly transport through rows between stomatal pores, toward the contact line. Therefore, they are rarely trapped inside the high-density stomatal pores (Fig. 4.8b), and mainly accumulate at the contact line region.

Small stomatal features with wide spacing (Fig. 4.8c) can represent partially closed stomata on adaxial side of a leaf at which the stomatal density is lower (Panarese et al., 2016). Comparing Fig. 4.8a and Fig. 4.8c, a wider stomatal pore seems to trap more bacteria per pore. The bacterial infiltration into stomatal opening during evaporation is concentration-dependent. Figure 4.8d shows the effect of 1 order of magnitude decrease in the bacterial concentration (compared with what is used in Fig. 4.8a) on their infiltration into stomatal pores. Obviously, the infiltration (presence of bacteria inside the pores as represented by fluorescence intensity) is more noticeable when bacterial concentration in the droplet is higher. Surface hydrophobicity can also affect the bacterial accumulation patterns within an evaporating droplet. A more hydrophobic surface (Fig. 4.8e, FOTS-deposited) has drastically reduced infiltration of bacteria within stomatal pore area compared to a hydrophillic surface (Fig. 4.8a, APTMS-deposited). The hydrophillic nature of the surface can keep the bacteria closer to the leaf surface. Therefore, the chance of bacteria to infiltrate the stomatal pores on a hydrophillic surface (Fig. 4.8a) is higher than that on a more hydrophobic surface (Fig. 4.8e).

4.4.3 Evaporation-driven movement of contact line deposits bacteria within surface microstructures

Microscopy imaging (Fig. 4.9a) reveals that mainly on a more hydrophobic surface (FOTS-deposited), when the evaporation rate is high enough, the contact line sticks and

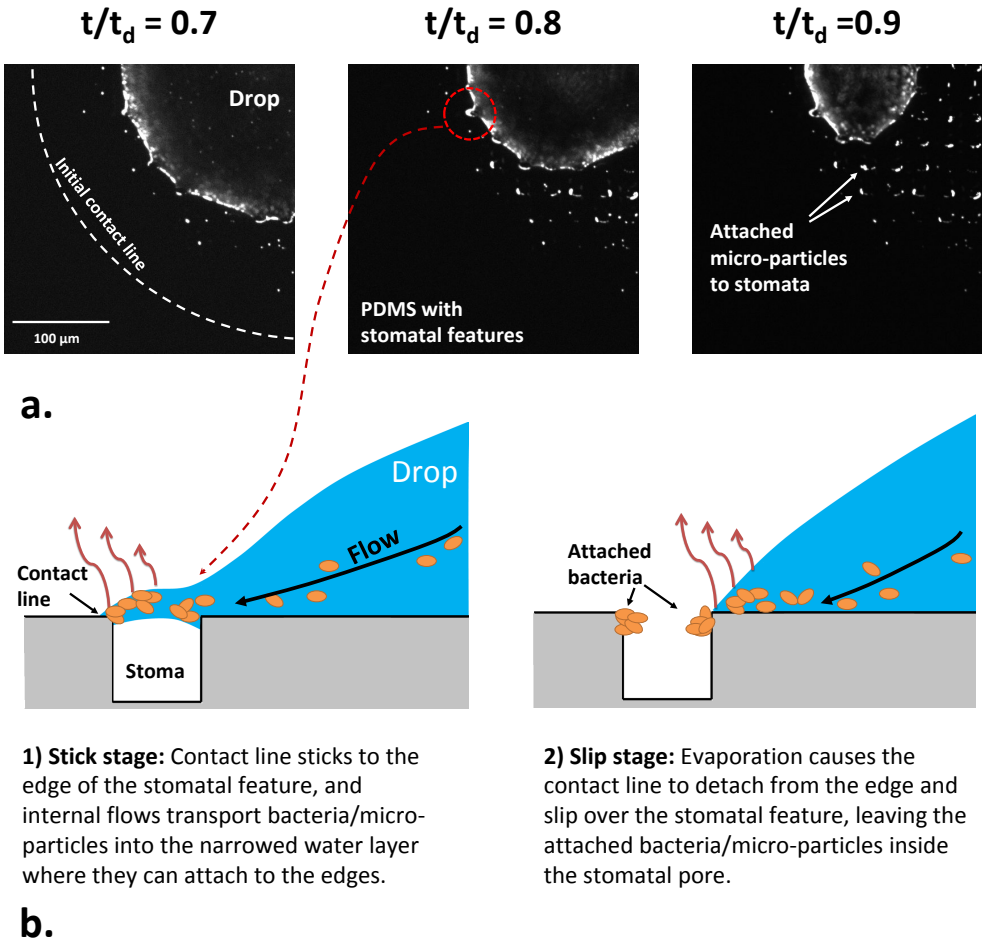

Figure 4.9: a) Deposition of 1 μm fluorescent microparticles, at different times during drying of a sessile droplet (with an initial concentration of 10^8 particles/ml), into stomatal pores, fabricated on a FOTS-coated (hydrophobic) PDMS surface. Here the $t_d = 7$min. b) schematic showing how a stick-slip behaiour of the contact line during evaporation of a sessile droplet can lead to bacterial deposition inside the stomatal pores.

slips over the microstructures. Here, instead of bacteria, fluorescent microparticles were used to show that this mechanism can lead to particle attachment to the microstructure even without any active attachment means, such as flagella that wild-type bacteria have. Evaporation-driven flows transport microparticles toward the contact line (Deegan et al., 2000). Receding movement of the contact line over stomatal pores, as a result of evaporation, leads to microparticle deposition at the edges or within the pores. This observation can be explained using a schematic shown in Fig. 4.9b: in the first (stick) stage, contact line sticks to the edge of the stomatal pore. Evaporation-driven internal flows transport bacteria/microparticles into the stuck region where they can attach to the surface and edges. Meanwhile, the surface tension forces tend to pull the liquid surface in an opposite direction (toward the drop center line), leading to a local reduction in the contact angle at the stuck edge. This smaller contact angle creates a higher evaporation flux at the stuck edge (as it acts like a hydrophyllic surface) and a stronger microparticle transport into the stuck region. As the drop evaporates, the surface tension forces cause the apparent contact angle of the drop to decrease to a critical value at which the de-pinning forces dominate the pinning forces (Fig. 4.4d). At this second (slip) stage (Fig. 4.9b), the contact line slips over the stomatal pore and leaves the attached microparticles/bacteria at the stomatal edge.

4.5 Conclusions

Evaporation of sessile droplets, containing bacterial suspensions, on plant leaves were studied using confocal microscopy. Due to complexity of the plant leaves in terms of variability in the surface roughness and hydrophobicity, fabricated PDMS surfaces were used to further understand the underlying mechanisms of microbial retention and infiltration during evaporation. Drop evaporation experiments on plant leaves showed that evaporation-driven flows can transport bacteria close to the leaf surface and facilitate their access to the microstructures, such as trichomes, stomata, and grooves, leading to

their significant infiltration into the stomatal opening. Larger size and wider spacing of the micropores, and a more hydrophillic surface led bacteria to spread more on the droplet base area and infiltrate into more stomata. The infiltration was more noticeable when the bacterial concentration in the droplet was higher. During evaporation of a droplet on stomatal pores, the contact line may stick to the pore edges and slip over them. Sticking of the contact line to the stomatal pores increases the time scale at which evaporation driven internal flows can transport bacteria into the stomata, that facilities their infiltration.

Acknowledgments

This work was supported by Grant 2014-70003-22357 from the USDA National Institute of Food and Agriculture. The microfabrication experiment were partially supported by a Spencer award. Microfabrications were done at Cornell Nanoscale Science and Technology Facility (CNF). Special thanks Dr. Beth Rhoades at CNF for all her guidance during fabrications and experimentation steps. The confocal microscopy imaging of plant leaves was done in the Plant Cell Imaging Center (PCIC) at Boyce Thompson Institute (BTI) of Cornell University.

Supplementary Information

Bacterial culture: *Escherichia coli* (*E. coli*) cells (RP437 strain, a gift from Sandy Parkinson, the University of Utah, transformed with pTrc-GFP plasmid in DeLisa lab, Cornell University) were grown in Tryptone Broth (10.0 g/L of Bacto Tryptone powder dissolved in phosphate-buffered saline (PBS)) supplemented with 100 g/ml Ampicillin in a shaker bath at 30 °C, 150 rpm. The overnight cultures were inoculated the next morning in a fresh Tryptone Broth medium ($\sim$ 25X) to a final concentration that corre-

sponds to OD600 $\sim$ 0.05. Inducer isopropyl thiogalactopyranoside was added to a final concentration of 1 mM when cell density reached OD600 $\sim$ 0.2. Cells were harvested at exponential growth phase when OD600 reached $\sim$ 0.5. Cells were resuspended twice (centrifuged at 1500 g for 2 min) in chemotaxis buffer (PBS, 0.1mM EDTA, 1μM methionine, 10 mM lactic acid, pH = 7.3) before experiments. All drop evaporation experiments were done within $\sim$ 2 h after the bacterial culture were prepared, to make sure that each experimental run used cells with exact same preparation procedures as described above.

BIBLIOGRAPHY

[1] Chen, X., Ma, R., Li, J., Hao, Ch., Guo, W., Luk, B.L., Li, Sh.Ch., Yao, Sh., Wang, Z. 2012. Evaporation of droplets on superhydrophobic surfaces: surface roughness and small droplet size effects. Physical Reviews Letters 109, 116101.

[2] Deegan R.D., Bakajin, O., Dupont, T.F., Huber, G., Nagel, S.R., Witten, Th.A. (1997). Capillary flow as the cause of ring stains from dried liquid drops. Nature 389, 827-829.

[3] Deegan R.D., Bakajin, O., Dupont, T.F., Huber, G., Nagel, S.R., Witten, Th.A. (2000). Contact line deposits in an evaporating drop. Physical Review E 62(1), 756-765.

[4] He, M., Liao, D., Qiu, H. 2017. Multicomponent droplet evaporation on chemical micropatterned surfaces. Scientific Reports 7, 41897.

[5] Hu, H., Larson, R. 2005a. Analysis of microfluid flow in an evaporating sessile droplet. Langmuir 21, 3963-3971.

[6] Hu, H., Larson, R. 2005b. Analysis of the effects of Marangoni stresses on the microflow in an evaporating sessile droplet. Langmuir 21, 3972-3980.

[7] Kasyap., T.V., Koch, D.L., Wu, M. (2014). Bacteria collective motion near contact line of an evaporating sessile drop. Physics of Fluids 26, 111703.

[8] Kroupitski,Y.,Golberg, D.,Belausov, E.,Pinto, R.,Swartzberg, D., Granot, D., Sela, Sh. 2009. Internalization of Salmonella enterica in Leaves Is Induced by Light and Involves Chemotaxis and Penetration through Open Stomata. Applied and Environmental Microbiology, 6076-6086.

[9] Lazouskaya, V., Sun, T., Liu, L., Wang, G., Jin, Y. 2016. Effect of surface properties on colloidal retention on natural and surrogate produce surfaces. Journal of Food Science 81(12), E2956-E2965.

[10] Monteux, C., Lequeux, F. 2011. Packing and sorting colloids at the contact line of a drying drop. Langmuir 27, 2917-2922.

[11] Sirinutsomboon, B., Delwiche, M.J., Young, G.M. (2011). Attachment of Escherichia coli on plant surface structures built by microfabrication. Biosystems Engineering 108, 244-252.

[12] Snoeijer, J.H., Andreotti, B. 2013. Moving contact lines: scales, regimes, and dynamical transitions. Annual Review of Fluid Mechanics 45, 269-292.

[13] Son, G. 2010. A level-set method for analysis of microdroplet evaporation on a heated surface. Journal of Mechanical Science and Technology 24 (4), 991-997.

[14] Starov, V., Sefiane, Kh. 2009. On evaporation rate and interfacial temperature of volatile sessile drops. Colloids and Surfaces A: Physicochemical and Engineering Aspects 333, 170-174.

[15] Thokchom, A.K., Swaminathan, R., Singh, A. 2014. Fluid flow and particle dynamics inside an evaporating droplet containing live bacteria displaying chemotaxis. Langmuir 30, 12144-12153.

CHAPTER 5

A MECHANISTIC MODEL FOR BACTERIAL RETENTION AND INFILTRATION ON A LEAF DURING A SESSILE DROPLET EVAPORATION

5.1 Abstract

Evaporation of sessile droplets at surface of plant leaves is a process that frequently occurs during plant growth as well as post-harvest processes. Evaporation-driven internal flows within sessile droplets can transport microorganisms near the leaf surface, facilitating their adhesion to surface microstructures such as trichomes, and infiltration into available openings such as stomata and grooves. A mechanistic model for this retention and infiltration pathway was developed. Solution domain is a sessile droplet located on a leaf surface, as well as its surrounding gas. The model includes fluid flow within the droplet and gas phases, gas-water interface tracking, heat transfer, transport of vapor in gas, and transport of sugar and bacteria within water. The model results are validated based on available literature data and experimental images. The results showed that a hydrophilic surface would promote bacterial retention and infiltration. Evaporation-driven flows increase concentration of bacteria around or inside microstructures at the leaf surface, facilitating their adhesion and infiltration. Larger microstructures having wider spacing between them increased the retention. Chemotaxis toward nutrients at the leaf surface and random motility were shown to decrease the retention and infiltration during evaporation.

5.2 Introduction

Leafy greens are among the most contaminated food products to various microorganisms (DeWaal and Bhuiya, 2007; Olaimat and Holley, 2012). Their contamination might

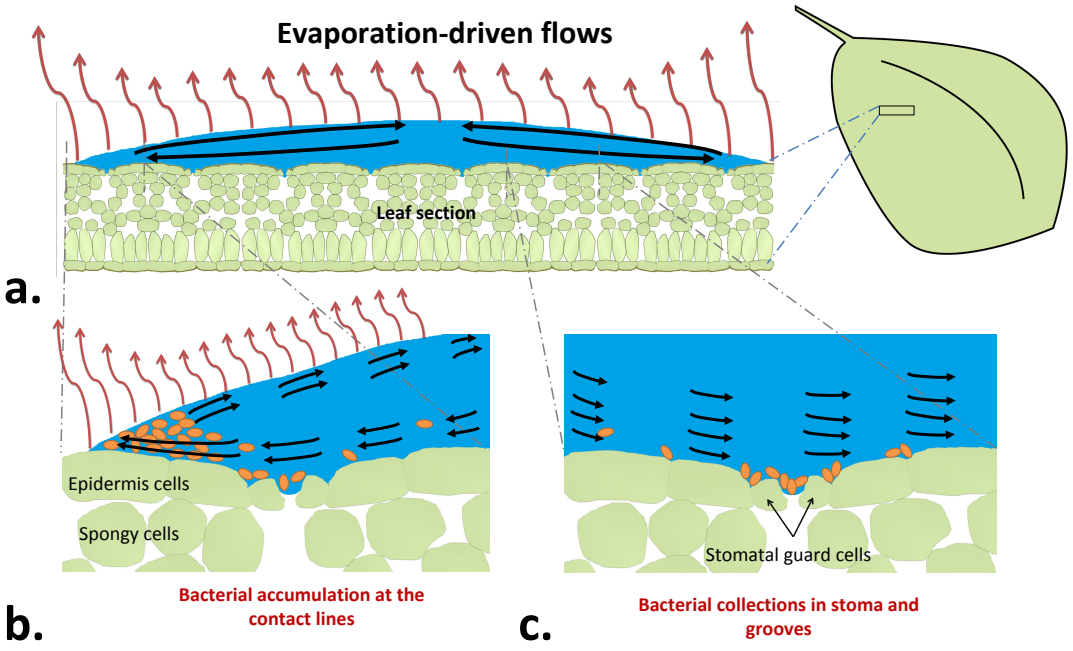

Figure 5.1: Evaporation of a water film at the leaf surface can lead to bacteria infiltration into the grooves and openings at the leaf surface.

be facilitated by various pathways such as imposed pressure gradients (Ranjbaran and Datta, 2019), light exposure (Kroupitski et al., 2009), and evaporation of water film at the leaf surface (Lazouskaya et al., 2016).

Sessile droplets of water frequently evaporate at the surface of plant leaves during the growth period and the post-harvest processing of leafy greens. The evaporation-driven internal flows within the sessile droplet can transport microorganisms close to the leaf surface and facilitate their adhesion to the surface microstructures such as trichomes, and infiltration into the available openings such as stomata and grooves (Fig 5.1). The flows within evaporating sessile droplets (Deegan et al., 1997; Hu and Larson, 2005a,b) and how these flows affect transport and deposition of colloids and bacteria at artificial surfaces (Monteux and Lequeux, 2011; Kasyap et al., 2014) have been studied over the years. Presence of chemical and structural complexities at a leaf

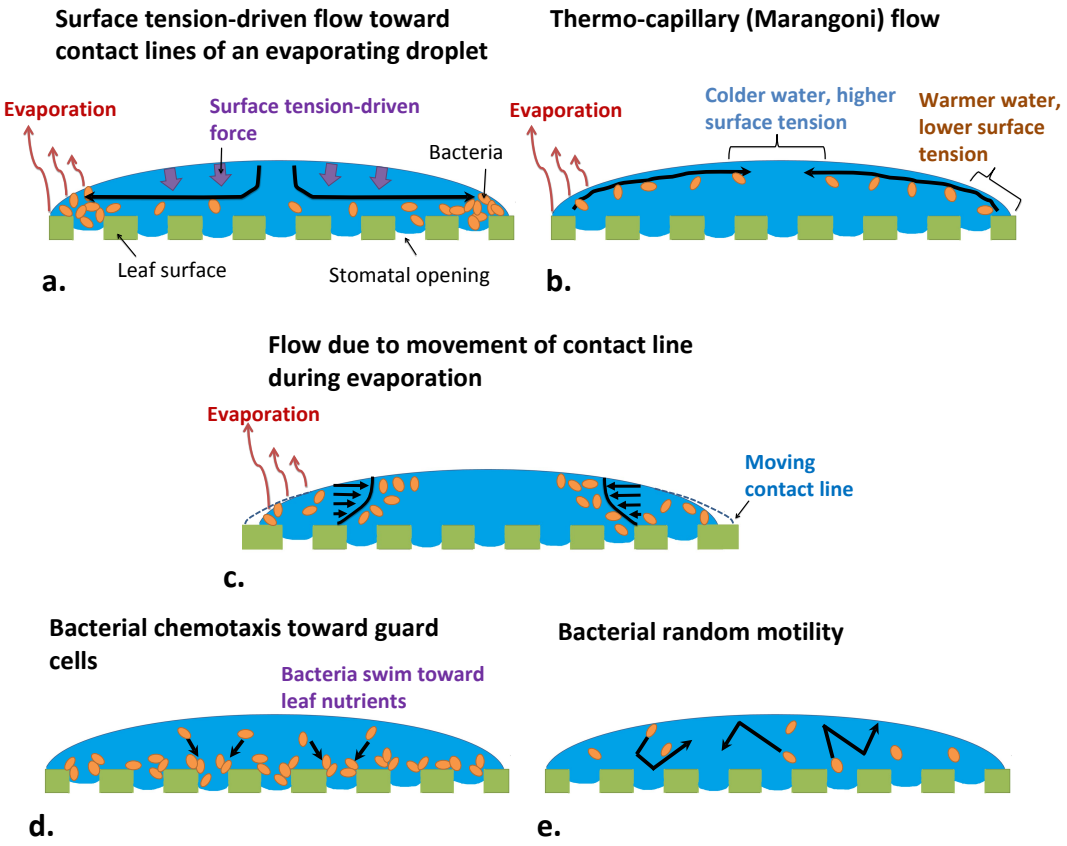

Figure 5.2: mechanisms of bacteria transfer in an evaporating sessile droplet on a leaf surface

surface, however, can affect the flow patterns within the evaporating sessile droplets and incorporate additional bacterial transport mechanisms.

The most important pathways contributing to bacterial transport in an evaporating sessile droplet at a leaf surface are (Fig 5.2): 1) **Flows toward contact line** (Fig 5.2a) that happen when the surface-tension forces, acting at the droplet surface, squeezes the fluid, making it flow toward the contact lines to compensate for the large evaporation losses at the contact lines (Deegan et al. 1997). These flows can transport bacteria toward the contact line regions (Kasyap et al., 2014). 2) **Thermo-capillary (Marangoni) flow** (Fig 5.2b) that happen due to the temperature gradients at the droplet surface. These flows can play a role in generating vortices within the droplet (Hu and Larson,

2005a) and transport bacteria away from contact lines. 3) **Flows due to movement of contact lines** (Fig 5.2c) that take place when the droplet recedes due to evaporation and escaping water molecules from the contact lines. These flows can transport bacteria away from contact line. Presence of surface roughness (Chen et al., 2012) or chemical heterogeneity (He et al., 2017) can cause the contact line movement to happen as a stick-slip motion. 4) **Bacterial chemotaxis** (Fig 5.2d) that is the directed movement of cells toward available nutrients at the leaf surface. Swimming speed of chemotactic bacteria is of the same order of magnitude as the flow velocity in an evaporating droplet (Curk et al., 2013; Kasyap et al., 2014). The photosynthetic products can attract bacteria to actively infiltrate the stomatal openings, and other crevices and cracks at the leaf surface (Kroupitski et al., 2009). 5) **Bacterial motility** (Fig 5.2e) that is a random run and tumbling motion of bacteria. This motion induces a diffusion-like transport (Kasyap et al., 2014) of cells toward locations with lower bacterial densities.

The complex process of evaporation-driven retention and infiltration of bacteria at/into plant leaves can be effectively understood by using a mechanistic model that complements experimental observations. The model can help better understand how various contributing factors and pathways work together to influence the overall process. This work presents a novel mechanistic model describing the role of evaporation of sessile droplets in bacterial retention and infiltration at/into plant leaves.

5.2.1 Objectives

The main objectives of this paper are to: 1) develop a model for transport of bacteria within an evaporating sessile droplet by fluid flows, 2) incorporate the role of active transport (chemotaxis and motility) in the model, 3) validate the model against experimental and literature data, and 4) identify the most important contributing factors and quantify of their relative contributions to evaporation-driven bacterial retention and infiltration.

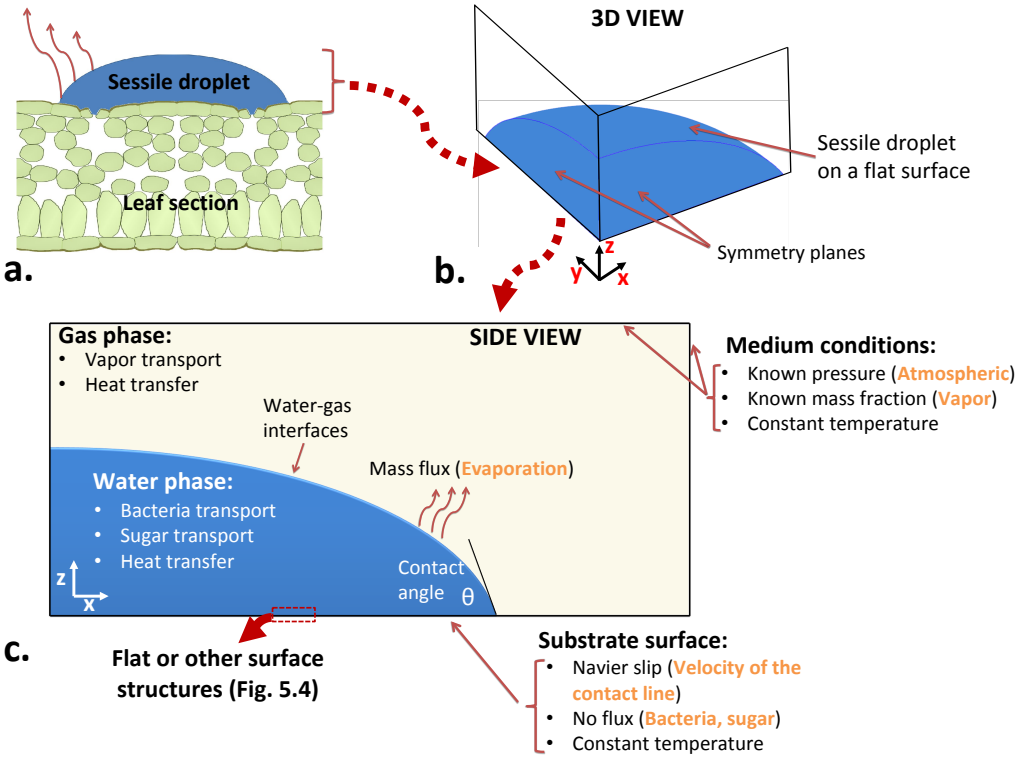

Figure 5.3: a) A physical leaf section with a water droplet containing bacteria at the surface, b) a 3D computational domain focusing on the water droplet and gas above the leaf surface. c) A side view of the solution domain introducing the boundary conditions.

5.3 Model development

5.3.1 Problem description and assumptions

A schematic of the problem description is shown in Fig. 5.3. A microdroplet containing a known bacterial concentration is located on a leaf surface (Fig. 5.3a). To avoid topological complexities existing at the leaf surface, the solution domain is simplified to be a flat surface (Fig. 5.3b). In addition to a flat surface, other substrate structures, i.e., stomata, grooves and trichomes (Fig. 5.4), are separately studied. The solution domain includes the epidermis layer of the leaf, the water droplet and the surrounding gas

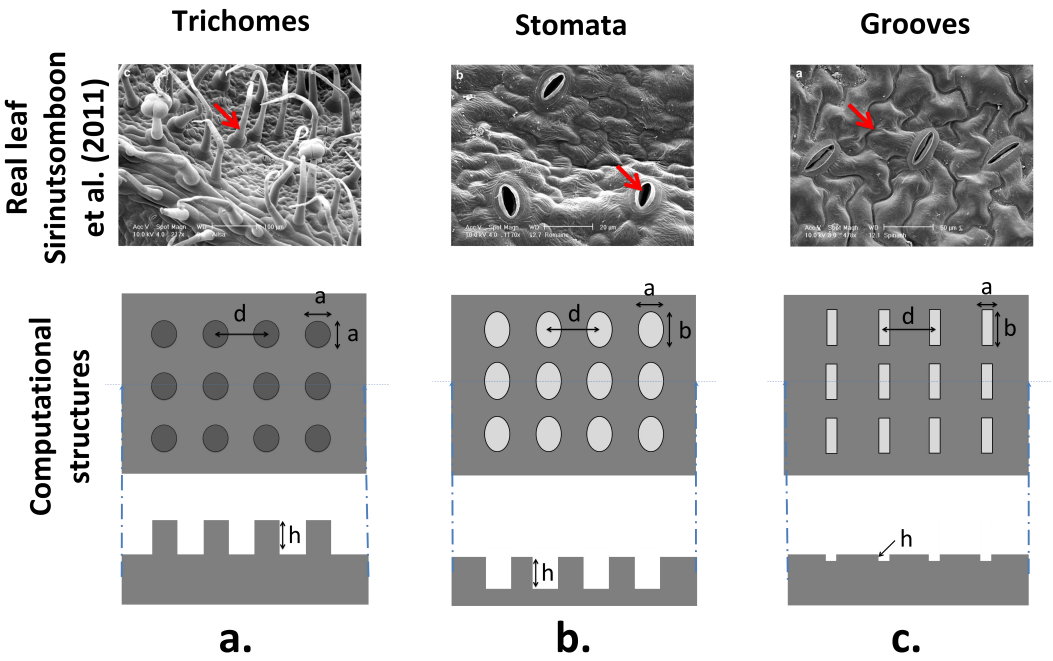

Figure 5.4: Microscopic images of the three types of the microstructures at the surface of plant leaves, adapted from Sirinutsomboon et al. (2011), and their computational analogues.

(Fig. 5.3c). A two-phase flow moving mesh approach describes the flow within droplet and surrounding gas. At the interface, there is a pressure jump due to liquid surface tension and evaporation effects. The evaporation flux at the interface is dynamically calculated from local vapor concentration and temperature. Movement of the contact line is described by the Navier slip condition which is used in conjunction with a prescribed dynamic contact angle (Sui et al., 2014). As the moving mesh approach does not tolerate mesh break-ups, the contact line was assumed to move only on flat a surface. Vapor generated from evaporation of the droplet transports within the gas phase. Heat transfer inside the entire domain is solved to include the evaporative cooling effects and updating temperature-dependent parameters. Inside the water phase, bacteria can transport by fluid flow and motility (diffusion-like transport). In the presence of sugar (glucose), bacteria can also do chemotaxis (convection-like transport). Sugar transports by the fluid flow within the droplet as well as molecular diffusion. When sugar transport is solved, a constant sugar concentration boundary condition at the internal walls

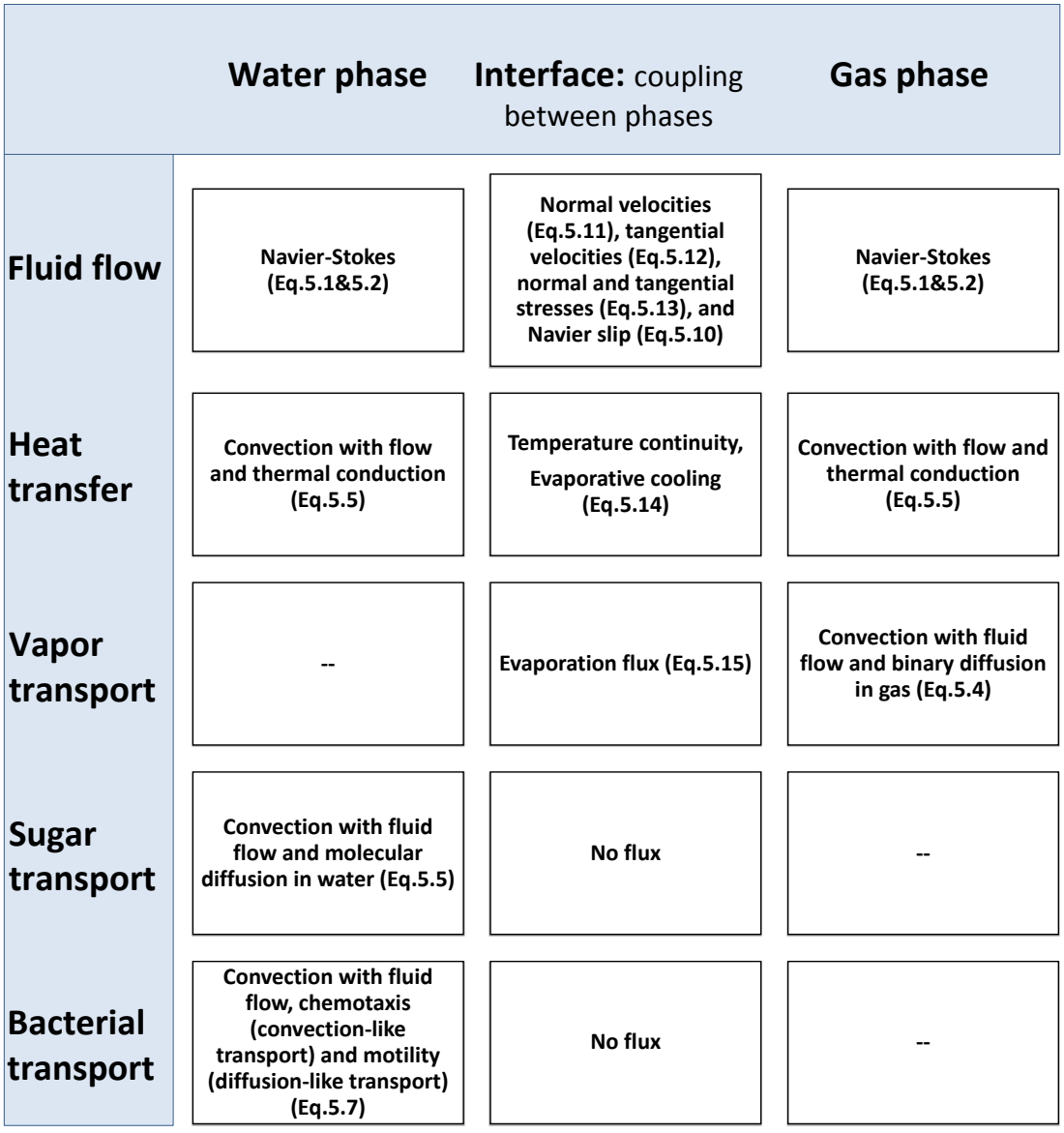

Figure 5.5: An overview of the model.

of stomatal openings simulates secretion of photosynthetic products from leaf interior into the droplet.

5.3.2 Governing Equations

An overview of the model is shown in Fig. 5.5. All of the equations are written in the mesh frame; their solution domain moves with the mesh. Fluid flow in each phase is described by Navier-Stokes equations coupled with an ALE moving mesh approach to track the interface. A heat transfer equation determines distribution of temperature within the fluids. Vapor transport is solved within the gas phase, while bacterial and sugar transport equations are solved in the liquid phase.

Flow of water and gas

Shape of a sessile droplet is mainly governed by the surface tension. For a small sessile droplet (*e.g.*, 1 μl), the Bond number ($Bo = \Delta\rho g L^2/\sigma$) which accounts for the balance of the surface tension and gravitational forces, is quite small (~ 0.04) (Hu and Larson, 2005a). Here, $\Delta\rho$ is the difference between densities of the two phases (kg/m^3), g is the gravitational acceleration (m/s^2), L is the characteristic length scale (m), and σ is the surface tension (N/m). Therefore, for a small droplet of size 1 μl, the surface forces dominate the body forces and the effect of buoyant flows due to changes in the water density can safely be neglected. Both gas and water phases are considered as Newtonian incompressible fluids here. Within both fluid phases (i.e., mesh frame), the continuity and momentum balance equations are as:

$$\nabla \cdot \mathbf{u} = 0 \tag{5.1}$$

$$\rho \frac{\partial \mathbf{u}}{\partial t} + \rho \mathbf{u} \cdot \nabla \mathbf{u} = \nabla \cdot \overline{\tau} + \rho \mathbf{g} \tag{5.2}$$

where ρ is fluid density (kg/m^3), $\mathbf{u}$ is the fluid velocity vector (m/s), P is the fluid pressure (Pa), η is the fluid viscosity, and $\mathbf{g}$ is the gravitational acceleration vector (m/s^2). The stress tensor, $\overline{\tau}$, is defined as:

$$\overline{\tau} = -P\mathbf{I} + \eta \left(\nabla \mathbf{u} + (\nabla \mathbf{u})^{\mathrm{T}} \right) \tag{5.3}$$

The movement of the mesh within the solution domain is done by an ALE approach whose equations are not elaborated here.

Transport of vapor in gas

Vapor is transported within the gas phase by binary diffusive and convective transport:

$$\frac{\partial}{\partial t}(\rho_g \omega_v) + \nabla \cdot (\mathbf{u_g} \rho_g \omega_v) = \nabla \cdot \left(\frac{C_g}{\rho_g} M_a M_v D_{bin} \nabla x_v \right) \tag{5.4}$$

where, ω_v and x_v are the mass (kg/kg) and mole (mol/mol) fractions of water vapor, respectively. D_{bin} is the binary diffusion coefficient (m^2/s), and M_a and M_v are molar masses (kg/mol) of air and vapor, respectively.

Heat transfer in water and gas

The heat transfer in fluids is described by a convection-diffusion equation:

$$\rho_f C_{p_f} \frac{\partial T}{\partial t} + \rho_f C_{p_f} \mathbf{u}_f \cdot \nabla T = \nabla \cdot (k_f \nabla T) \tag{5.5}$$

where k_f and C_{p_f} are thermal conductivity and specific heat capacity of fluids (W/m·K), respectively.

Transport of sugar in water

Sugar (glucose) available at the leaf surface is transported into the water film and attract bacteria toward leaf stomata. In an evaporating sessile droplet, the effect of aerotaxis on bacterial transport and deposition was shown to be insignificant (Kasyap et al., 2014), and is ignored here. A transport equation is used to describe the distribution of the glucose concentration (c_{sug}) within the droplet:

$$\frac{\partial c_{sug}}{\partial t} + \nabla \cdot (\mathbf{u}_l c_{sug}) = \nabla \cdot (D_{sug,l} \nabla c_{sug}) \tag{5.6}$$

where $D_{sug,l}$ is the diffusivity of glucose in water (m^2/s).

Transport of bacteria within water

Bacteria are transported within the water droplet. They can be advected by water velocity ($\mathbf{u}_w$) and actively swim with a chemotactic velocity ($\mathbf{u}_{chx}$) toward nutrient concentration gradients. In addition, the tumbling motion of bacteria would induce a diffusion-like transport within the water phase. As the drop evaporation takes a short time (e.g., 10 min), the growth of bacteria and their consumption of nutrients was neglected. Transport of bacteria within the water droplet is described by a modified Keller-Segel equation (Tindall et al., 2008):

$$\frac{\partial c_b}{\partial t} + \nabla \cdot ((\mathbf{u}_l + \mathbf{u}_{chx})c_b) = \nabla \cdot (D_{b,l} \nabla c_b) \tag{5.7}$$

where c_b is the bacterial concentration (CFU/m^3), $D_{b,l}$ is the diffusivity of bacteria (m^2/s) within water. For motile bacteria, it is called coeficient of random motility. The chemotactic velocity is defined as (Tindall et al., 2008):

$$\mathbf{u}_{chx} = \chi_{cht} \nabla c_{sug} \tag{5.8}$$

Here χ_{cht} is chemotactic coefficient (1/s):

$$\chi_{cht} = \chi_0 \frac{K_d}{(K_d + c_{sug})^2} \tag{5.9}$$

where χ_0 is chemotactic sensitivity coefficients (m^2/s) and K_d is the receptor-ligand binding dissociation constant (kg/m^3).

Table 5.1: Input Parameters

Parameter	Symbol	Value	Units	Source
Density				
Water	ρ_w	998	kg/m^3	Rahman (2005)
Vapor	ρ_v	Ideal gas	kg/m^3	Assumed
Air	ρ_a	Ideal gas	kg/m^3	Assumed
Specific heat capacity				
Water	C_{p_w}	4176	$J/kg \cdot K$	Rahman (2010)
Vapor	C_{p_v}	1793	$J/kg \cdot K$	Rahman (2010)
Air	C_{p_a}	1005	$J/kg \cdot K$	Rahman (2010)
Thermal conductivity				
Water	k_w	0.60	$W/m \cdot K$	Rahman (2010)
Vapor	k_v	0.026	$W/m \cdot K$	Rahman (2010)
Air	k_a	0.026	$W/m \cdot K$	Rahman (2010)
Viscosity				
Water	μ_w	9.27×10^{-4}	$Pa \cdot s$	McCabe et al. (1956)
Gas	μ_g	1.80×10^{-5}	$Pa \cdot s$	McCabe et al. (1956)
Interfacial energy				

Water-gas	σ	$10^{-3}(114.81 - 0.1435T)$	N/m	Kazemi et al. (2017)
Diffusivity				
Vapor in air	D_{bin}	$\left(\frac{2.13}{P}\right)\left(\frac{T}{273.15}\right)^{1.8}$	m^2/s	Millington and Quirk (1961)
Bacteria in water	$D_{b,w}$	1×10^{-11}	m^2/s	Ranjbaran and Datta (2019)
Sugar in water	$D_{sug,w}$	0.67×10^{-9}	m^2/s	Nobel (2005)
Other parameters				
Latent heat of vaporization of water	h_{lv}	2.26×10^6	J/kg	Ranjbaran and Datta (2019)
Slip length of contact lines	β	15×10^{-9}	m	Assumed from Kazemi et al. (2017)
Bacteria chemotaxis				
Chemotactic sensitivity coefficient, *E. coli*	χ_0	10×10^{-9}	m^2/s	Ford et al. (1991)
Receptor-ligand dissociation constant	K_d	0.1	mol/m^3	Ford and Lauffenburger (1991)

5.3.3 Input parameters, initial and boundary conditions

The input data for the simulations are shown in Table 5.1. Initially, the droplet having a known volume (1 μl) forms a spherical cap with a known contact angle at the substrate surface. The initial velocities of fluids are zero everywhere. There is a uniform concentration of bacteria in the droplet which is normalized to 1. Temperature is initially constant at 25 °C everywhere. If sugar transport is to be solved, its initial concentration is zero in the droplet. The boundary conditions (Fig. 5.3c) are elaborated below.

Solid walls

At the contact line (wall-interface connection), the dynamic contact angle, θ, is prescribed, based on experimental measurement data (Ranjbaran, 2019), over evaporation time. At all solid walls the normal component of the fluid velocity is zero. At walls that are entirely covered with a specific fluid phase, a no slip condition sets the tangential slip velocities of the fluid to zero. Whereas, for the solid wall that is in touch with the contact line, a Navier slip (Sui et al., 2014) condition is assumed that relates the slip velocity of the contact line to the shear rate at the surface:

$$\mathbf{u} \cdot \mathbf{t}_i = \frac{\beta}{\eta}(\overline{\tau} \cdot \mathbf{t}_i) \tag{5.10}$$

where t is the unit tangential vectors at the interface, $i = 1, 2$, and β is the slip length (m).

A constant temperature boundary condition was assumed at all solid surfaces. If sugar transport is to be solved, a constant concentration of sugar was assumed at the internal walls of the stomatal pores. A no flux condition was applied in the bacterial transport at all solid walls.

Liquid-gas interface

From a mass balance at the interface, the following relationship between normal velocities of water and gas can be obtained:

$$\mathbf{u}_l \cdot \mathbf{n} = \mathbf{u}_g \cdot \mathbf{n} + \dot{m} \left(\frac{1}{\rho_l} - \frac{1}{\rho_g} \right) \tag{5.11}$$

where $\mathbf{n}$ is the unit normal vector at the interface, and $\dot{m}$ is the local mass flux at the interface due to phase change (kg/m^2.s). By adopting a no-slip condition at the interface, the tangential components of liquid and gas velocities are equal:

$$\mathbf{u}_l \cdot \mathbf{t}_i = \mathbf{u}_g \cdot \mathbf{t}_i \tag{5.12}$$

where $i = 1, 2$. The three other conditions needed for resolving momentum transfer at the interface are embedded in (Panton, 2005):

$$\overline{\tau}_l \cdot \mathbf{n} = \overline{\tau}_g \cdot \mathbf{n} - \sigma \kappa \mathbf{n} - \nabla_t \sigma + \dot{m}(\mathbf{u}_l - \mathbf{u}_g) \tag{5.13}$$

Here $\kappa = -\nabla_t \cdot \mathbf{n}$ is the curvature of the interface (1/m). The second and third terms on the right-hand side of Eq. 5.13 are the capillary and thermo-capillary (Marangoni) stresses, respectively, and the last term is the momentum transfer due to inertia. These three terms represent a pressure jump at the interface.

A temperature continuity at the interface (*i.e.*, $T_l = T_v$) is assumed here. Therefore, an energy balance at the interface gives:

$$k_l \nabla T = k_v \nabla T - \dot{m} h_{lv} \tag{5.14}$$

where h_{lv} is the latent heat of evaporation of water (J/kg).

The local mass flux at the interface due to evaporation (kg/m^2.s) is calculated from (Son, 2010):

$$\dot{m} = \frac{\mathbf{n} \cdot D_{bin} \rho_g \nabla \omega_v}{(1 - \omega_{sat})} \tag{5.15}$$

where ω_{sat} is the mass fractions of vapor at saturation point, and the saturation density of vapor (kg/m^3), ρ_{sat}, is defined as:

$$\rho_{sat} = \frac{P_{sat} M_v}{RT} \tag{5.16}$$

where R is the universal gas constant (8.314J/mol $\cdot$ K), and P_{sat} is the vapor pressure at saturation point (Murray, 1967):

$$P_{sat} = \frac{101325}{760} 10^{\left(8.07131 - \frac{1730.63}{T - 39.574}\right)} \tag{5.17}$$

At the interface a no flux condition is applied to bacterial and sugar transport.

The mesh velocity at the interface is obtained from:

$$\mathbf{u}_{mesh} = \mathbf{u} \cdot \mathbf{n} - \frac{\dot{m}}{\rho} \mathbf{n} \tag{5.18}$$

Surrounding boundaries

For all surrounding boundaries confining the domain, there are known bulk gas velocity/pressure and temperature, and a known vapor mass fraction.

5.3.4 Solution procedure

The governing equations were solved using a commercial finite element package, COMSOL Multiphysics version 5.4 (COMSOL Multiphysics, Burlington, MA). The time-step size was varied between 0.001 s to 0.1 s. The relative and absolute tolerances were 0.001 for all computations. The solution domain was meshed with more than 70000 mesh elements. A very fine mesh was used at the location of the contact lines and microstructures. The solutions were done with the PARDISO direct solver. Run time for the simulations was about 15 minutes on a Windows machine with 32 GB of RAM, and 2 GHz dual core Intel© Xeon© CPU E5-2620 processor.

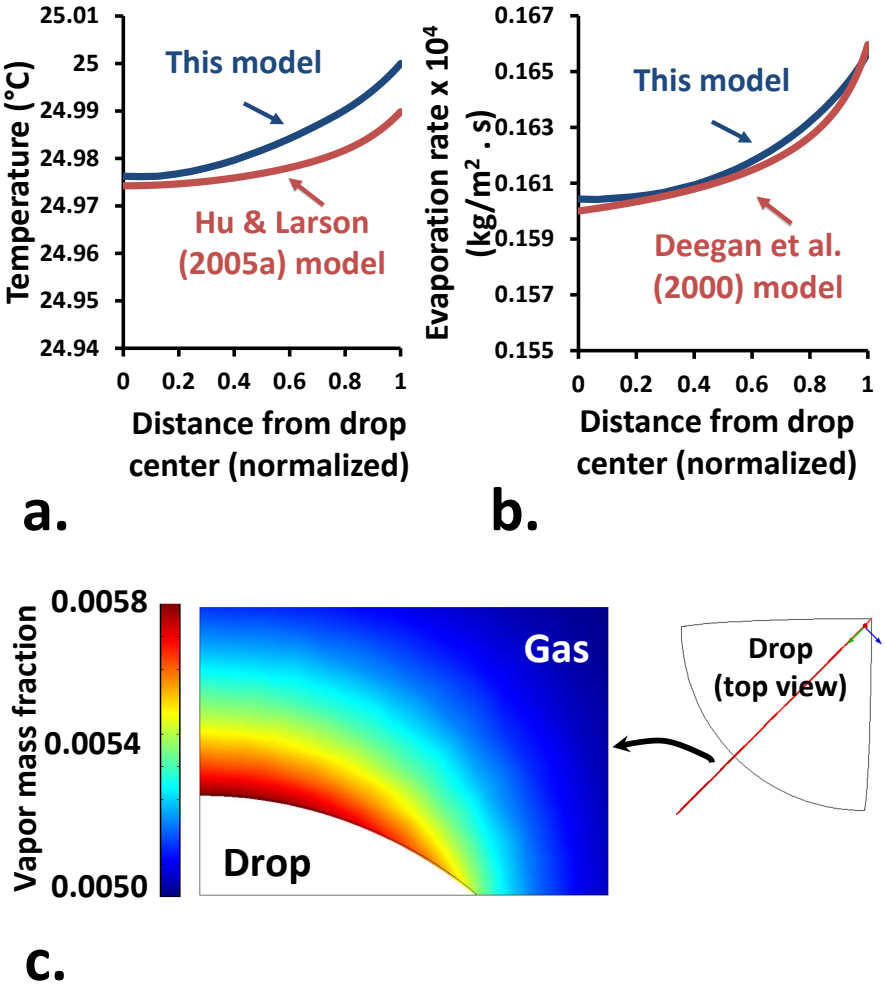

Figure 5.6: Typical variations of a) droplet surface temperature, and b) evaporation rate along the drop radius. The predicted distributions for temperature and rate of evaporation are compared with the analytically models reported by Hu and Larson (2004), and Deegan et al. (2000), respectively. c) A typical contour plot of vapor mass fraction above the droplet surface. The data is related to a drying time of 6 min.

5.4 Results and Discussion

5.4.1 Spatial distribution of temperature and evaporation

Temperature distribution at the droplet surface is not uniform due to the evaporative cooling effects, being colder on the apex and warmer near the contact line (Fig.5.6a) (Hu and Larson, 2005; Girard et al., 2008; Starov and Sefiane, 2009). This is because the fluid near the contact line is closer to the substrate and can exchange heat with it through conduction. Therefore, although the rate of evaporation is higher at the contact line (and more evaporation cooling effect might be expected), the fluid is warmer at this region. At the location of the contact line, the rate of evaporation increases (Fig. 5.6b) (Deegan et al., 2000). This is because the saturation mass fraction of vapor is higher at the contact line due to higher temperature. In addition, the local concentration of vapor decreases at this region, leading to a larger concentration gradient of vapor (Fig. 5.6c) and its faster diffusion into open ambient. Figure. 5.6b compares predicted evaporation flux with the prediction of Deegan et al., (2000) that was already verified with experimental work of Monteux and Lequeux (2011):

$$J_{evp} = \frac{D_{bin}(c_{v,sat} - c_{v,\infty})}{\rho_w x^{\alpha} R^{1-\alpha}} \tag{5.19}$$

where R is the radius of the droplet, x is the distance from the contact line, and $\alpha = (\frac{\pi}{2} - \theta)/(\pi - \theta)$, with θ being the contact angle of the droplet (Fig. 5.3c). The non-uniformity in the evaporation flux within the droplet is a major contributor in the generation of internal flows within the droplet, as discussed in the next section.

5.4.2 Velocity patterns

Evaporative flux theoretically goes to infinity at the location of contact line, as $J_{evp} \sim 1/x^{\alpha}$ (Eq. 5.19). Inside the droplet, this induces a flow (with a velocity U_{evp}) toward the

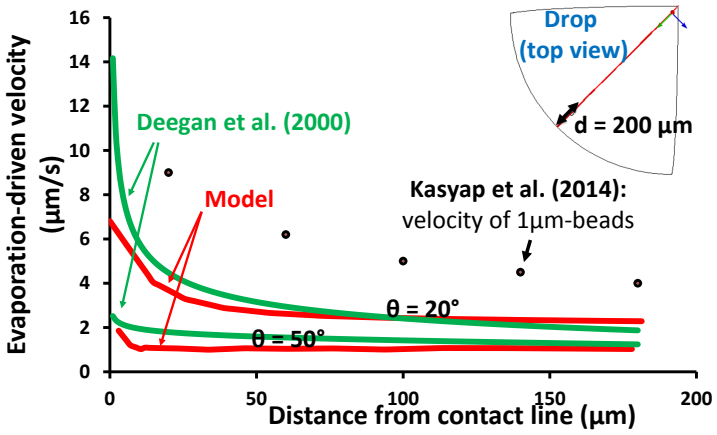

a.

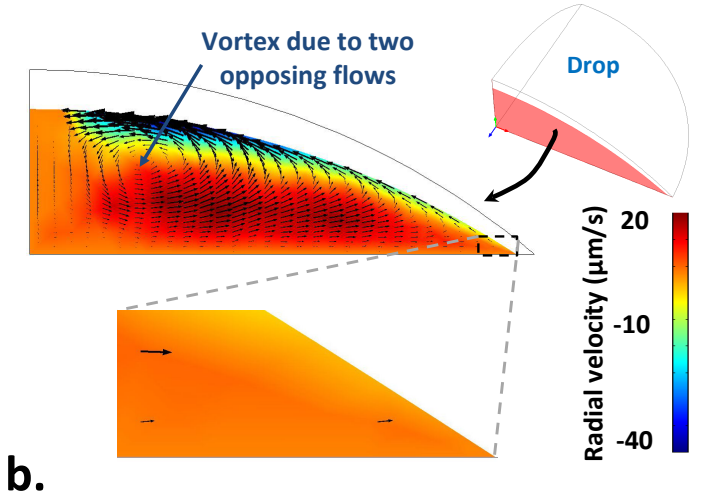

b.

Figure 5.7: a) Evaporation-driven velocity within sessile droplets at flat substrates predicted by the current computational model and the analytically model of Deegan et al. (2000). The predictions are compared with measured velocities of 1 μm fluorescent beads suspended in an evaporating droplet on a flat substrate (Kasyap et al., 2014). b) A typical velocity profile in an evaporating sessile droplet, with a focus on the contact line.

contact line (Fig. 5.2a). An estimation of the U_{evp} was reported by Deegan et al. (2000) that was obtained from the lubrication theory for an evaporating sessile droplet on a flat substrate:

$$U_{evp} = \frac{R\left((1-\overline{r}^2)^{-\lambda_\theta} - (1-\overline{r}^2)\right)}{4t_d(1-\frac{t}{t_d})\overline{r}} \tag{5.20}$$

where t_d is the total drying time, $\overline{r} = (R-x)/R$ is non-dimensional radial coordinate measured from the center of the droplet, and $\lambda_\theta = 0.5 - \theta/\pi$. Figure 5.7a compares the model predictions of the flow on a flat substrate for a sessile droplet, with initial contact angles of 40° and 70°, with those predicted by Eq. 5.20 and experimental data reported by Kasyap et al. (2014) for the velocity of 1 μm fluorescent beads in an evaporating droplet on a glass substrate. The Deegan's estimation (Eq. 5.20) was calculated by considering the updated contact angle of droplets after 6 minutes of evaporation. As can be seen, the fluid velocity increases in the vicinity of the contact line. This velocity is higher in a droplet located at a more hydrophilic surface. This is because the evaporation flux at the contact line of a droplet located on a more hydrophillic surface is stronger, leading to higher velocity of fluid toward the contact line. Meanwhile, as droplet evaporates, the contact line recedes in an opposite direction, creating a receding flow (with a velocity U_{rsd}) away from the contact line (Fig. 5.2c) (Berteloot et al., 2008; Snoeijer and Andreotti, 2013). Thermo-capillary effects also cause flows toward the center of the droplet (Fig. 5.2b). A combination of these three mechanisms creates a vortex within an evaporating droplet (Fig. 5.7b). At the early stage of evaporation, the flow velocity toward the contact line, U_{evp}, is weak and is scaled to about 1 μm/s. At the longer evaporation times, however, following a decline in the contribution of receding flow velocity, U_{rsd}, the velocity toward the contact line, U_{evp}, increases to tens of μm/s. These predictions are supported by experimental observations of Monteux and Lequeux (2011) showing that the radial flow of fluorescent microbeads, directed toward the contact line of an evaporating sessile droplet, increased an order of magnitude, from 1 μm/s to 20 μm/s.

Presence of the microstructures changes the velocity patterns in the proximity of the

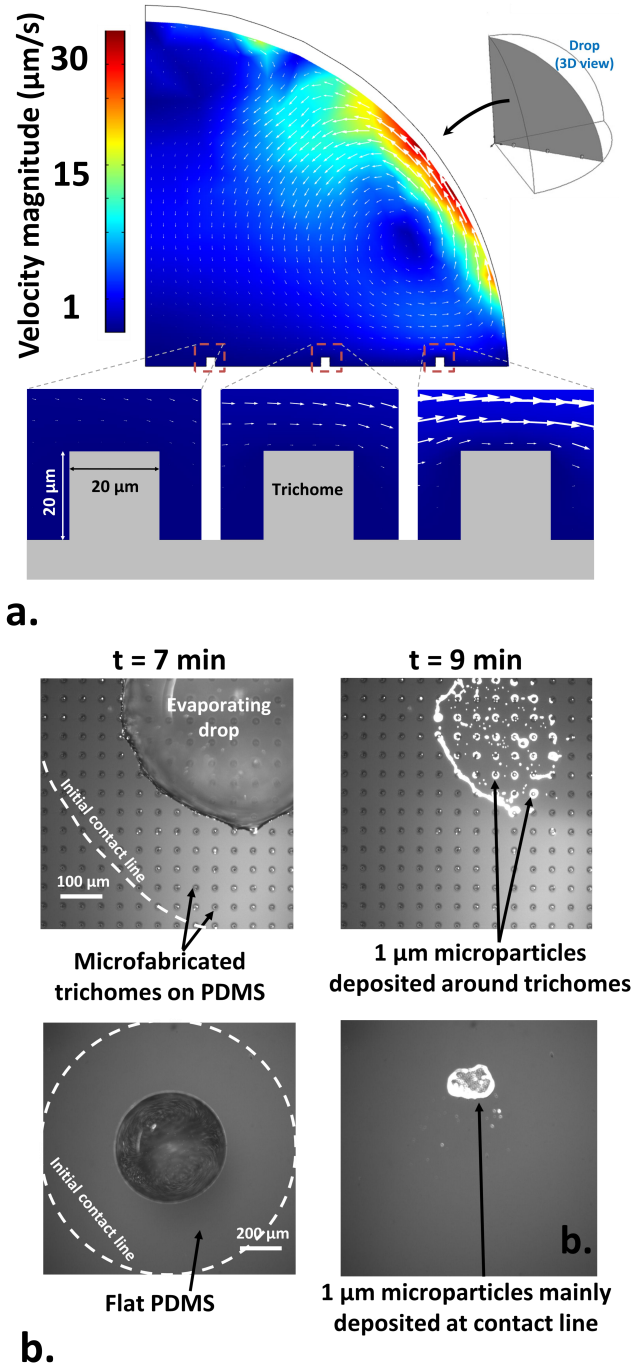

Figure 5.8: a) Velocity magnitude in an evaporating sessile droplet, and b) deposition of fluorescent micro-particles around microfabricated trichomes, indicating their role in trapping particles that are transported with the flow.

leaf surface. Trichomes are micropillars that flow passes around or over them (Fig. 5.8a). If the flow contains microparticles, they interact with the surface of trichomes. Fluid velocity approaches to zero when reaching the trichome surfaces, creating spots that microparticles can safely attach to the substrate surface without being transported with the fluid. Note that the physics of attachment of microparticles to a plant surface (Warning and Datta, 2017) is not included in the current model which focuses on the modes of transport of bacteria as a continuum phase. Figure 5.8b shows an evaporating 1 μl sessile water droplet containing 1 μm fluorescent microparticles (1×10^7 particle/ml), located on a PDMS surface ($\theta = 74^\circ$) patterned with trichome microstructures (see Chapter 4 for fabrication details). After 9 min of evaporation, the microparticles are shown to deposit around the trichomes, suggesting their critical role in decreasing fluid velocity and trapping microparticles transported with the fluid flow. These patterns are compared (Fig. 5.8b) with those on a flat PDMS surface with the same hydrophobicity level, suggesting the role of trichomes in trapping microparticles. Similarly, trichomes on plant leaves (Fig. 5.4) act as micro-pillars standing in front of the internal flows within evaporating droplets, to which colloids and bacteria can attach.

The same mechanism can aid bacteria suspended in sessile droplets located at the surface of plant leaves to reach these microstructures, increasing the probability of their attachment to the surface.

5.4.3 Bacterial collection at the surface

When a sessile droplet containing bacteria evaporates on a leaf, it eventually deposits all the bacterial cells on its surface. However, the deposition pattern and area depend on surface characteristics (hydrophobicity and roughness), rate of evaporation, and bacterial charactristics (ability to do motility and chemotaxis). If the cells are deposited on an open surface of the leaves, they could be washed away during rinsing practices. However, the bacterial cells may also be transported into leaf openings or deposit around tri-

chomes that protect them from wash fluids. Effects of the above factors on the bacterial retention at the leaf surface and infiltration into the leaf openings, during evaporation, are analyzed.

Effect of hydrophobicity

On a hydrophilic surface, evaporation driven flows keep the bacterial cells closer to the surface. Figure 5.9a shows the variation of the bacterial amount over evaporation time within a distance of 5 μm away from a flat substrate. For a hyrdophilic surface ($\theta = 40^\circ$), this amount increases with a higher rate during evaporation. Since the drop spreads more on a hydrophilic surface, the area of interaction between bacteria and the substrate is larger than that for a hydrophobic surface. Therefore, the cells can contaminate a wider area on a hydrophilic surface.

Deegan et al. (2000) showed that on a flat substrate, the total number of colloids (N) accumulated near contact lines follows a power-law trend in time:

$$N_{col,acum} = N_{col,tot}\left(1-(1-t/t_f)^{(1+\alpha)/2}\right)^{2/(1+\alpha)} \tag{5.21}$$

where t_f is the total drying time. Figure 5.9b qualitatively compares the bacterial amount at the location of contact lines with Deegan's model (Eq. 5.21) for accumulation of colloidal particles at the contact lines. For hydrophobic surfaces ($\theta = 90^\circ$), the amount of accumulation at the contact line decreases. This is because evaporation driven flows (U_{evp}) toward contact lines are weakened for a hydrophobic surface. Contours of predicted bacterial concentration within an evaporating sessile droplet on a flat substrate with an initial contact angle of 40° is shown in Fig. 5.9c. When there is no evaporation, bacterial concentration remains uniform within the droplet as there is no flows within the droplet and cells can only have a diffusion-like transport (motility). Therefore, no bacterial collection happens at the location of contact line. However, evaporation drives bacterial transport with water flow, leading to a non-uniform con-

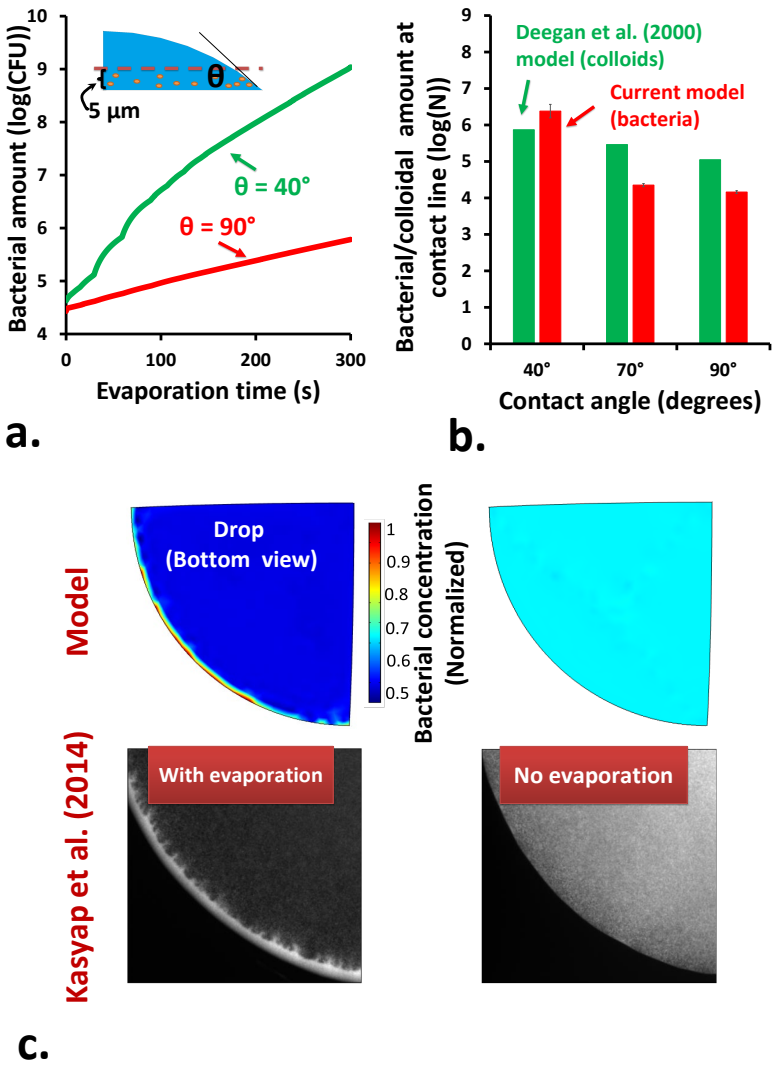

Figure 5.9: a) Variation of the total amount of bacterial cells within a distance of 5 μm close to the surface of flat substrates with two different levels of hydrophobicity. b) A comparison between Deegan's model describing the amount of colloidal particles accumulated at the location of contact lines (Eq. 5.21), with the predictions of the current computational model for the amount of bacteria at the location of contact line. Eq. 5.21, the total drying time was assumed to be 1500 s. In the computational model, the data was obtained within 50 μm of the contact lines. Error bars indicate the respective variations for 1 order of magnitude change in the rate of evaporation. c) Contours of bacterial accumulation at the location of contact lines on a flat substrate. The model predictions are qualitatively compared with experimental observations of Kasyap et al. (2014) for evaporating/non-evaporating droplets on a glass substrate.

centration patterns within the droplet. The predicted collection of bacteria near the contact line is compared with experimental observations of Kasyap et al. (2014) (Fig. 5.9c) after 6 min of evaporation.

Effect of microstructures

To obtain a fundamental understanding of the effects of surface microstructures on the bacterial collections, the model focused on a few microstructures. In Fig. 5.10a, a sessile droplet with $\theta = 90^{\circ}$ evaporated on a substrate surface containing three stomatal opening. The predicted bacterial distribution within the droplet after 5 min of drying shows how internal flows can transport cells into the openings. In reality, once the bacteria reach sufficiently close to these microstructures (stomata), they can use their flagella, or other adhesion means, to attach to the microstructure. The amount of bacterial collection at each microstructure increases with the evaporation time as the evaporation-driven flows close to the leaf surface increase during drying (Eq. 5.20). Figure 5.10b shows the image of an evaporating sessile droplet containing gfp-tagged *E. coli* RP437 on a PDMS surface patterned with microfabricated stomatal openings (See Chapter 4 for details of the experiments). The fluorescence intensity diagram reveals how the bacteria accumulated at the contact line as well as stomatal openings. This accumulation supports the model predictions in Fig. 5.10a, showing the role of internal flows in transport of bacteria into the leaf openings. This transport of bacteria into the stomatal openings is more likely to happen when the surface is hydrophilic and the droplet is in Wenzel state (*i.e.*, drop completely sits on the surface and covers the microstructures). On highly hydrophobic surfaces where the droplet is more likely to be in the Cassie state (*i.e.*, drop sits on top of the microstructures without any contact with the surface), the drop may not penetrate into pores. In this case, although bacteria are transported to the pores, they will be relocated by the flow without any infiltration.

In general, the amount of bacterial accumulation close to a surface is higher for a

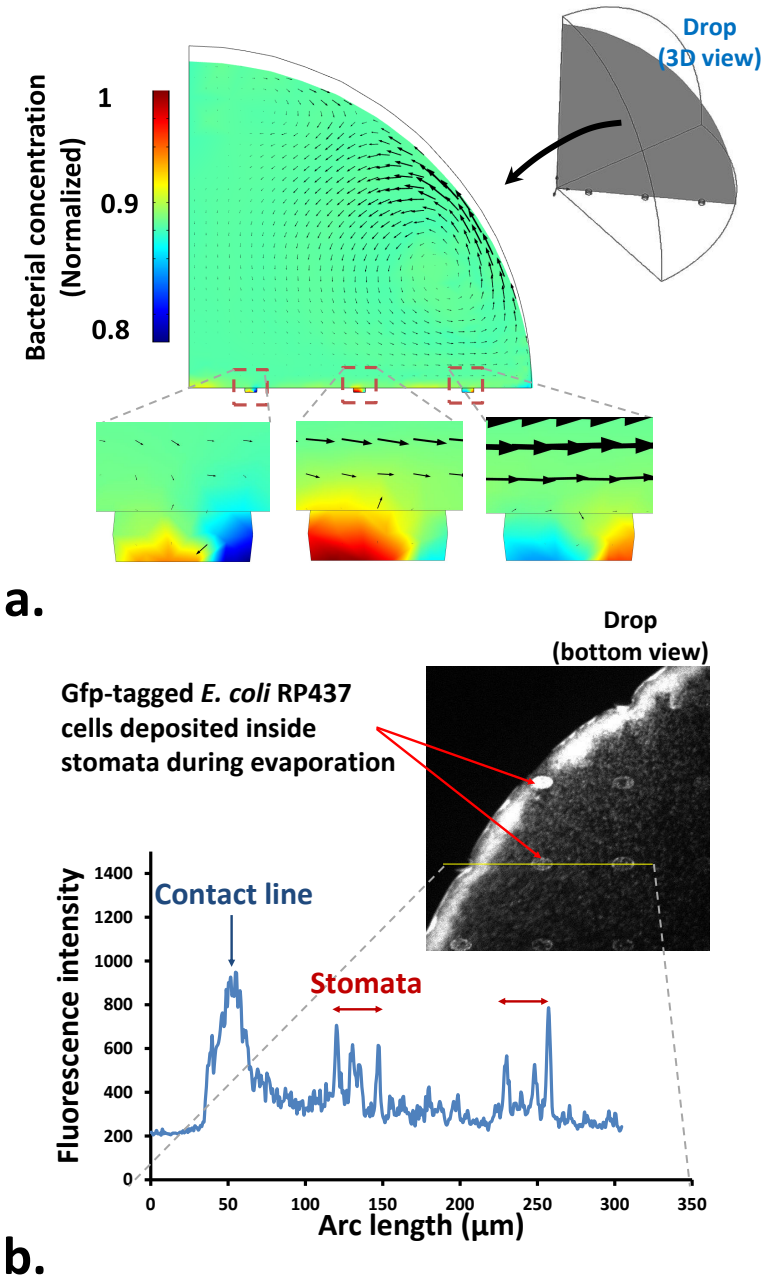

Figure 5.10: a) Distribution of bacterial concentration in an evaporating sessile droplet located on a substrate with three stomatal pores. b) Fluorescence intensity variation along a series of microfabricated stomatal opening, made from PDMS (See Chapter 4 for details of fabrication and experiments), located under an evaporating sessile droplet. The inset image is taken from bottom side of the droplet. Bright areas represent higher concentrations of the fluorescent *E. coli* RP437.

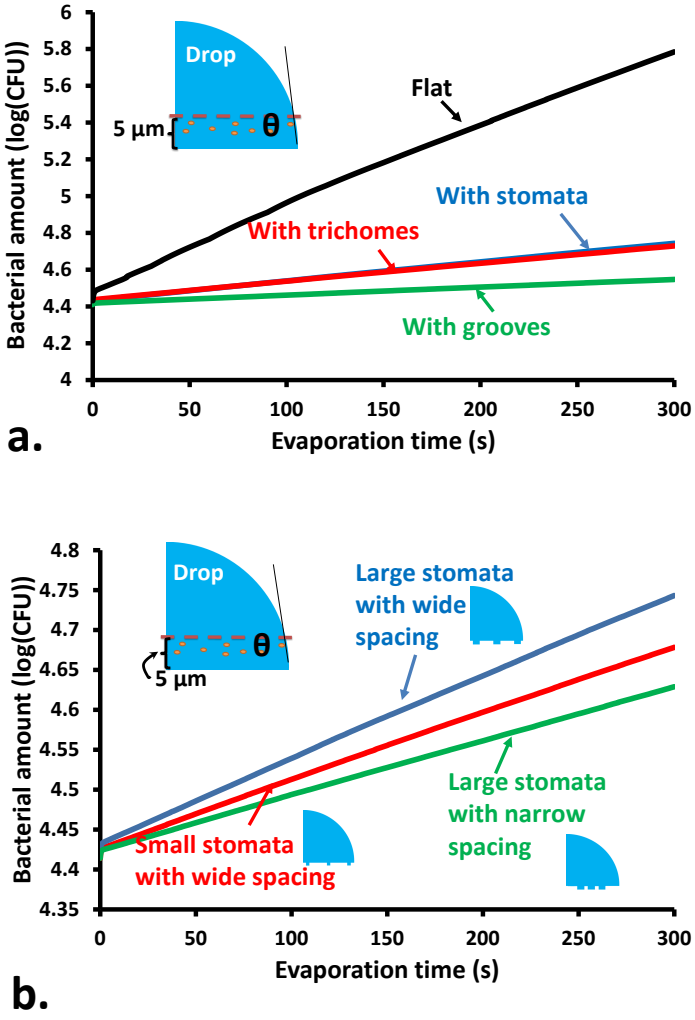

Figure 5.11: a) Variation of the total amount of bacterial cells within a distance of 5 μm close to the surface of various substrates. For non-flat substrates, three microstructures with 150 μm spacing were considered. b) The same variations for substrates with various stomatal size and spacing, shown as insets. For the narrow spacing case, distance between adjacent features is 75 μm.

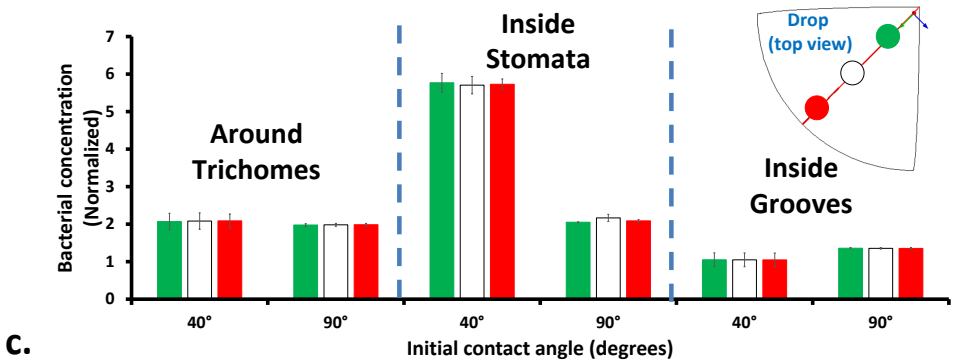

Figure 5.12: Bacterial concentration around trichomes, and inside stomata and grooves after 300 s evaporation of a sessile droplet on substrate surfaces with different levels of hydrophobicity. The error bars show 30% change in the rate of evaporation. The results are normalized to the initial concentration of bacterial within the droplet before evaporation starts.

flat substrate (Fig. 5.11a). Presence of microstructures, such as trichomes, stomata and grooves, causes changes in the flow patterns within the evaporating droplet, leading to less accumulation near the substrate surface. For instance, stomata create upward flows away from the stomatal pore (Fig. 5.10a) that can interfere with radial flows toward the contact lines. These upward flows can transport unattached bacteria away from the leaf surface. However, when microstructures are present, the bacteria have higher chance to attach to them or infiltrate inside the pores, leading to enhanced contamination. Among different microstructures, stomata are more effective in increasing bacterial accumulation near the substrate surface that here is defined as the total amount of bacteria in a 5 μm distance from the substrate surface (Fig. 5.11a). The size and spacing of the microstructures can affect the bacterial retention near the substrate surface (Fig. 5.11b). Larger stomata with a wider spacing can keep more bacteria near the surface. Spacing has a more dominant effect than the size on the bacterial retention near a substrate surface.

Figure 5.12 shows the amount of bacterial concentration around trichomes or within

stomata and grooves after 5 min of drying, for two levels of hydrophobicity of the substrate and at three different locations with respect to the drop center line. The error bar shows the effect of a 30% change in the evaporation rate. The concentration of bacteria around trichomes and within stomata is higher when the substrate is highly hydrophilic ($\theta = 40^{\circ}$). This is because the evaporation driven flows responsible for transport of bacteria are stronger, leading to retention of more bacteria close to the substrate surface (Fig. 5.9a) and an increase in the chance of their accumulation within the stomatal pores or around trichomes. Stomata are larger openings than grooves (Fig. 5.4c). Therefore, bacterial concentration can increase more inside stomata, as the fluid velocity can be lower inside them. As the depth of grooves is shallow, fluid velocity can simply transport bacteria out of them, leading to less bacterial concentration inside them. This is more evident for more hydrophilic surfaces ($\theta = 40^{\circ}$).

Effect of active transport

Swimming speed of chemotactic bacteria in an aqueous medium is $\sim 10\ \mu$m/s (Curk et al., 2013), which is comparable the flow velocity magnitude in an evaporating droplet (Monteux and Lequeux, 2011; Kasyap et al., 2014). Therefore, the two active (taxis and motility) and passive (flow) transport mechanisms compete during evaporation of a droplet on a leaf surface. It was previously shown that aerotaxis (active swimming toward oxygen gradients) was not an effective factor in bacterial collection at the location of contact lines of an evaporating droplet located on a glass substrate (Kasyap et al., 2014). However, the role of chemotaxis of bacteria in destabilizing flows within an evaporating sessile droplet and altering the final deposition patterns on the substrate has been documented (Thokchom et al., 2014). Plant leaves can provide surface-located bacteria a rich source of photosynthetic products (Kroupitski et al., 2009) that can play a role in bacterial access to the leaf surface during sessile drop evaporation. Assuming a constant concentration of sugar at the boundaries of the stomatal pores, the model was re-solved with chemotaxis. When there is no evaporation, sugar only diffuses within

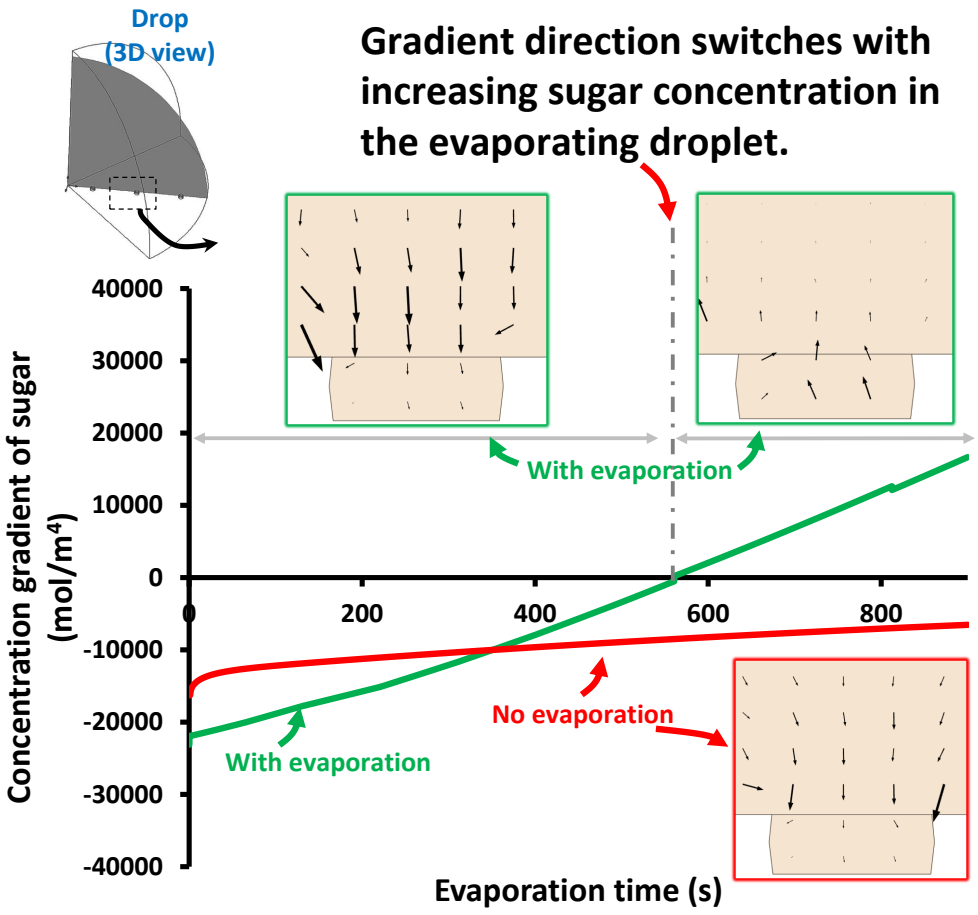

Figure 5.13: Variation of concentration gradient of sugar, at the entrance of a stomatal pore in presence and absence of evaporation. The insets show the directions of the bacterial chemotactic velocity that follows the gradients.

the droplet and its concentration gradient at the stomatal opening is always toward the pore (Fig. 5.13). In the presence of evaporation, sugar is transported within the droplet by the internal flows as well as diffusion. At the initial stage of the evaporation, the sugar concentration within the droplet is low, creating a high concentration gradient toward stomatal pores. This accelerates bacterial access to the stomata. By progression of the evaporation, however, droplet volume decreases, leading to an increase in the sugar concentration within the droplet and gradual reduction of the gradients. Eventually, the concentration of sugar within the droplet becomes higher than that in the stomatal pore,

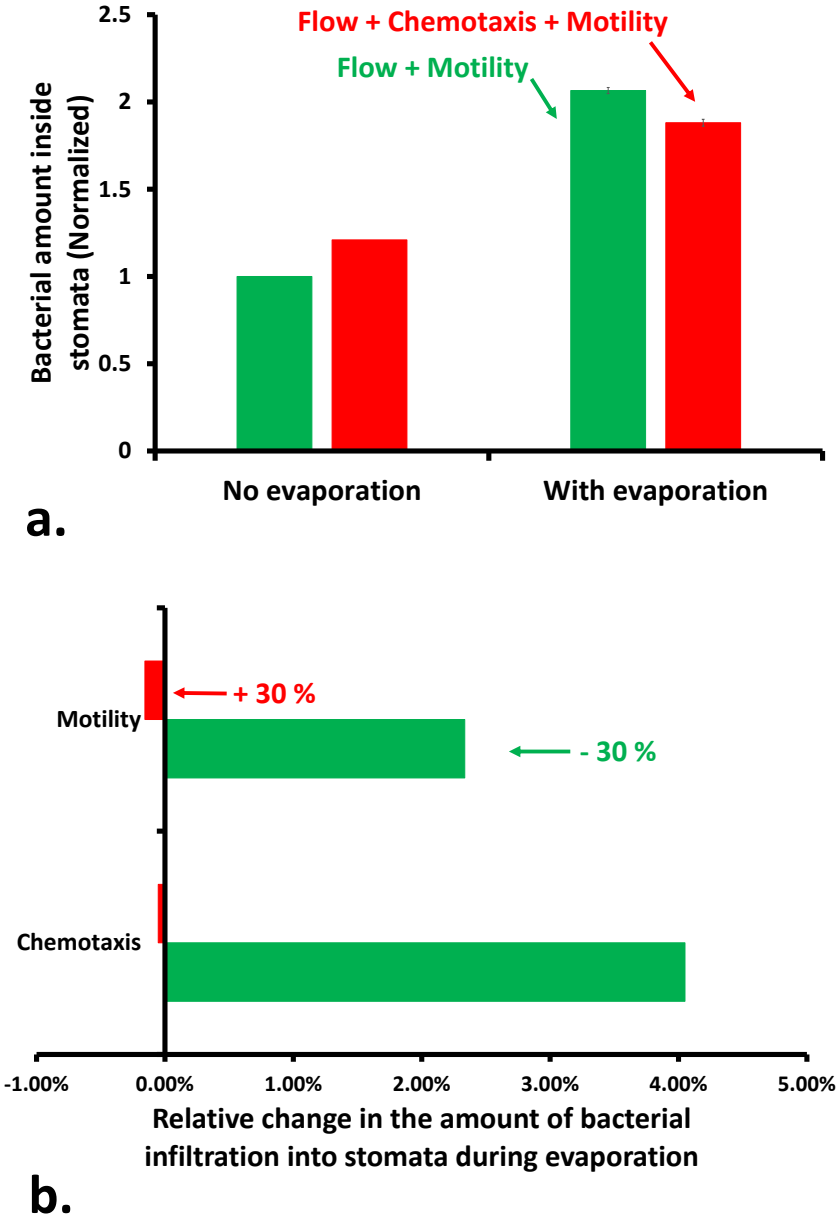

Figure 5.14: a) Bacterial concentration inside stomata after 300 s evaporation of a sessile droplet on a substrate surface with a contact angle of 90°. The effect of two different combinations of transport mechanisms are shown. b) Effects of 30% change in motility and chemotactic coefficients on the amount of bacterial infiltration into stomatal pores, during evaporation.

making the concentration gradient away from the stomatal pores (Fig. 5.13). Therefore, if the bacteria are able to do chemotaxis, they tend to swim toward the droplet rather than into the stomatal pore at the later stages of evaporation.

Figure 5.14a compares bacterial infiltration into stomatal pores in the presence and absence of chemotaxis. Without evaporation, there are no internal flows and no net infiltration by the non-chemotactic bacteria. However, without evaporation, chemotactic bacteria can transport via chemotaxis toward the stomatal pores and infiltrate them. In the presence of evaporation, internal flows and chemotaxis are responsible for the directed movement of bacteria toward stomata. However, contribution of chemotaxis toward stomata gradually reduces and finally reverses, *i.e*, away from the stomata as concentration gradient of sugar evolves during evaporation (Fig. 5.13). This decreases the amount of bacterial infiltration into the stomata compared with when there is no chemotaxis (Fig. 5.14a).

A sensitivity analysis for the effects of motility and chemotaxis on bacterial infiltration into stomata during evaporation is shown in Fig. 5.14b. A 30% decrease in the bacterial motile and chemotactic ability led in 2.3% and 4.1% increase in the bacterial infiltration. Random motion of bacteria away from stomata deceases when the motility decreases. This increases their concentration inside the stomatal pore. Bacteria with lower chemotaxis ability are mainly transported with fluid flow, leading to more infiltration. These results highlight the suppressing roles that active transport modes (chemotaxis and motility) have on passive transport with evaporation-driven fluid flow into the leaf openings.

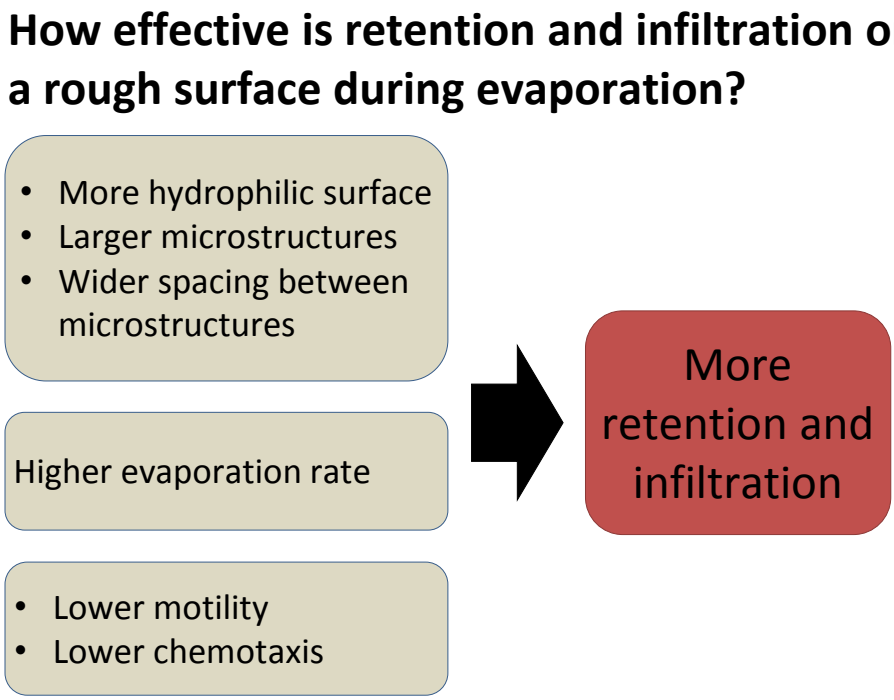

Figure 5.15: Various factors affecting the efficacy of retention and infiltration of bacteria on a rough surface, during evaporation of a sessile droplet.

5.4.4 Summary of influencing factors in retention and infiltration

A summary of the primary and secondary factors affecting bactreial retention and infiltration facilitated by evaporation-driven flows are shown in Fig. 5.15. Surface hydrophobicity is a major factor: a more hydrophilic surface leads to more retention and infiltration. Also, lower chemotaxis toward nutrients at the leaf surface and lower random motility can result in more retention and infiltration during evaporation. Evaporation rate, and microstructure size and spacing are among the secondary factors.

5.5 Conclusions

A mechanistic model for transport of bacteria in an evaporating sessile droplet located on a leaf surface was presented. The predicted process parameters such as temperature, evaporation rate and evaporation-driven velocity in the vicinity of the contact line were compared with classical analytical models and experimental data. It was shown that internal flows within the evaporating sessile droplet are the major responsible for transporting bacteria close to the leaf surface and into the leaf openings. A hydrophilic substrate can better cause bacterial retention at its surface during evaporation. In general, presence of microstructures decreased the effectiveness of internal flows in transporting bacteria close to the leaf surface. However, on a non-flat surface, these flows could increase the concentration of bacteria around microstructures such as trichomes, or inside micropores such as stomata and grooves, facilitating their further attachment to the substrate. The bacterial retention increased when the microstructures were larger and/or their spacing was wider. The bacterial retention and infiltration were not highly sensitive to the evaporation rate, suggesting that only presence of evaporation is sufficient to promote bacterial transport. In an evaporating droplet on a leaf surface containing nutrients, infiltration of non-chemotactic bacteria is more than that of chemotactic ones. Higher motility decreased the infiltration as it decreased the chance of bacteria in the droplet to reach the stomatal pores.

Acknowledgments

This work was supported by Grant 2014-70003-22357 from the USDA National Institute of Food and Agriculture.

BIBLIOGRAPHY

[1] Berteloot, G., Pham, C.T., Daerr, A., Lequeux, F., Limat. (2008). Evaporation-induced flow near a contact line: Consequences on coating and contact angle. EPL 83, 14003.

[2] Chen, X., Ma, R., Li, J., Hao, Ch., Guo, W., Luk, B.L., Li, Sh.Ch., Yao, Sh., Wang, Z. (2012). Evaporation of droplets on superhydrophobic surfaces: surface roughness and small droplet size effects. Physical Reviews Letters 109, 116101.

[3] Curk, T., Marenduzzo, D., Dobnikar, J. (2013). Chemotactic Sensing towards Ambient and Secreted Attractant Drives Collective Behaviour of E. coli. PLoS ONE 8(10): e74878.

[4] Deegan R.D., Bakajin, O., Dupont, T.F., Huber, G., Nagel, S.R., Witten, Th.A. (1997). Capillary flow as the cause of ring stains from dried liquid drops. Nature 389, 827-829.

[5] Deegan R.D., Bakajin, O., Dupont, T.F., Huber, G., Nagel, S.R., Witten, Th.A. (2000). Contact line deposits in an evaporating drop. Physical Review E 62(1), 756-765.

[6] DeWaal, C.S., Bhuiya, F. (2007). Outbreaks by the Numbers: Fruits and Vegetables. 1990-2005, vol. 2012.

[7] Ford, R., Lauffenburger, D., (1991). Measurement of Bacterial Random Motility and Chemotaxis Coefficients: II. Application of Single-Cell-Based Mathematical Model. Biotechnology and Bioengineering 37, 661-672.

[8] Ford, R.M., Phillips, B.R., Quinn, J.A. & Lauffenburger, D.A. (1991). Measurement of Bacterial Random Motility and Chemotaxis Coefficients: I. Stopped-Flow Diffusion Chamber Assay.Biotechnology and Bioengineering 37(7), 647-660.

[9] Girard, F., Antoni, M., Faure, S., Steinchen, A. (2008). Influence of heating temperature and relative humidity in the evaporation of pinned droplets. Colloids and Surfaces A: Physicochemical and Engineering Aspects 323,36-49.

[10] He, M., Liao, D., Qiu, H. (2017). Multicomponent droplet evaporation on chemical micropatterned surfaces. Scientific Reports 7, 41897.

[11] Hu, H., Larson, R. (2005a). Analysis of the effects of Marangoni stresses on the microflow in an evaporating sessile droplet. Langmuir 21, 3972-3980.

[12] Hu, H., Larson, R. (2005b). Analysis of microfluid flow in an evaporating sessile droplet. Langmuir 21, 3963-3971.

[13] Kasyap., T.V., Koch, D.L., Wu, M. (2014). Bacteria collective motion near contact line of an evaporating sessile drop. Physics of Fluids 26, 111703.

[14] Kazemi, M.A., Nobes, D.S., Elliott, J.A.W. (2017). Experimental and numerical study of the evaporation of water at low pressures. Langmuir 33, 4578-4591.

[15] Kroupitski,Y.,Golberg, D.,Belausov, E.,Pinto, R.,Swartzberg, D., Granot, D., Sela, Sh. (2009). Internalization of Salmonella enterica in Leaves Is Induced by Light and Involves Chemotaxis and Penetration through Open Stomata. Applied and Environmental Microbiology, 6076-6086.

[16] Lazouskaya, V., Sun, T., Liu, L., Wang, G., Jin, Y. (2016). Effect of surface properties on colloidal retention on natural and surrogate produce surfaces. Journal of Food Science 81(12), E2956-E2965.

[17] McCabe, W.L., Smith, J.C., Harriott, P. (1956). Unit Operations of Chemical Engineering, vol. 5. McGraw-Hill, New York.

[18] Millington, R., Quirk, J. (1961). Permeability of porous solids. Transactions of the Faraday Society 57, 1200-1207.

[19] Monteux, C., Lequeux, F. (2011). Packing and sorting colloids at the contact line of a drying drop. Langmuir 27, 2917-2922.

[20] Murray, F.W. (1967). On the computation of saturation vapor pressure. J. Appl. Meteorol. 6, 203204.

[21] Nobel, P.S. (2005) Physicochenichal And Environmental Plant Physiology. 3rd Ed. Elsevier Academic Press. Burlington, MA.

[22] Olaimat, A.N., Holley, R.A. (2012). Factors influencing the microbial safety of fresh produce: A review. Food Microbiology 32(1), 1-19.

[23] Panton, R.L. (2005). Incompressible Flow. John Wiley and Sons, Inc. New Delhi.

[24] Rahman, M.Sh. (2005). Mass-Volume-Area-Related Properties of Foods. In, Rao, M.A., Rizvi, S.S.H., Datta, A.K. (Eds). Engineering Properties of Foods. 3rd Ed. CRC Press, Boca Raton, FL.

[25] Rahman, M.Sh. (2010). Food Properties Handbook. CRC Press, Boca Raton, FL.

[26] Ranjbaran, M. (2019). Pathways of Bacterial Infiltration into Plant Leaves: Mechanistic Modeling, Microbiological and Microfabrication Experiments. PhD Dissertation, Cornell University, Ithaca, NY, USA.

[27] Ranjbaran, M., Datta, A.K. (2019). Pressure-driven infiltration of water and bacteria into plant leaves during vacuum cooling: A mechanistic model. Journal of Food Engineering 246, 209-223.

[28] Sirinutsomboon, B., Delwiche, M.J., Young, G.M. (2011). Attachment of Escherichia coli on plant surface structures built by microfabrication. Biosystems Engineering 108, 244-252.

[29] Snoeijer, J.H., Andreotti, B. (2013). Moving contact lines: scales, regimes, and dynamical transitions. Annual Review of Fluid Mechanics 45, 269-292.

[30] Son, G. (2010). A level-set method for analysis of microdroplet evaporation on a heated surface. Journal of Mechanical Science and Technology 24 (4), 991-997.

[31] Starov, V., Sefiane, Kh. (2009). On evaporation rate and interfacial temperature of volatile sessile drops. Colloids and Surfaces A: Physicochemical and Engineering Aspects 333, 170-174.

[32] Sui, Y., Ding, H., Spelt, P.D.M. (2014). Numerical simulations of flows with moving contact lines. Annual Reviews of Fluid Mechanics 46, 97-119.

[33] Tindall, M.J., Maini, P.K., Porter, S.L., Armitage, J.P. 2008. Overview of Mathematical Approaches Used to Model Bacterial Chemotaxis II: Bacterial Populations. Bulletin of Mathematical Biology 70: 1570-1607.

[34] Thokchom, A.K., Swaminathan, R., Singh, A. (2014). Fluid flow and particle dynamics inside an evaporating droplet containing live bacteria displaying chemotaxis. Langmuir 30, 12144-12153.

[35] Warning, A.D., Datta, A.K. (2017). Mechanistic understanding of non-spherical bacterial attachment and deposition on plant surface structures. Chemical Engineering Science 160, 396-418.